

DISSERTATION

PART I: ELECTROREDUCTIVE POLYMERIZATION OF NANOSCALE SOLID
POLYMER ELECTROLYTES FOR THREE-DIMENSIONAL LITHIUM-ION
BATTERIES

PART II: PHYSICAL CHARACTERIZATION AND HYDROGEN SORPTION
KINETICS OF SOLUTION-SYNTHEZIZED MAGNESIUM NANOPARTICLES

Submitted by

Timothy S. Arthur

Department of Chemistry

In partial fulfillment of the requirements

For the degree of Doctor of Philosophy

Colorado State University

Fort Collins, Colorado

Summer 2010

COLORADO STATE UNIVERSITY

July 12th, 2010

WE HEREBY RECOMMEND THAT THE DISSERTATION PREPARED UNDER OUR SUPERVISION BY TIMOTHY S. ARTHUR ENTITLED PART I: ELECTROREDUCTIVE POLYMERIZATION OF NANOSCALE SOLID POLYMER ELECTROLYTES FOR THREE-DIMENSIONAL LITHIUM-ION BATTERIES AND PART II: PHYSICAL CHARACTERIZATION AND HYDROGEN SORPTION KINETICS OF SOLUTION-SYNTHEZIZED MAGNESIUM NANOPARTICLES BE ACCEPTED AS FULFILLING IN PART THE REQUIREMENTS FOR THE DEGREE OF DOCTOR OF PHILOSOPHY.

Committee on Graduate Work

Travis S. Bailey

C. Michael Elliott

Mathew P. Shores

John D. Williams

Advisor: Amy L. Prieto

Department Head: Ellen R. Fisher

ABSTRACT OF DISSERTATION

PART I: ELECTROREDUCTIVE POLYMERIZATION OF NANOSCALE SOLID POLYMER ELECTROLYTES FOR THREE-DIMENSIONAL LITHIUM-ION BATTERIES

PART II: PHYSICAL CHARACTERIZATION AND HYDROGEN SORPTION KINETICS OF SOLUTION-SYNTHESIZED MAGNESIUM NANOPARTICLES

The demand for secondary batteries with longer cycle life and higher power is greater now than ever. Lithium-ion batteries have emerged as the leading technology to store electrochemical energy and power our transportation needs. By employing solution-based nanotemplating methods, new three-dimensional cell configurations can exploit the high-surface area of nanowire array electrodes. A key to the architecture is the deposition of a nanoscale solid polymer electrolyte (SPE). The non-active component must provide sufficient electrical insulation and lithium-ion conductivity between the electro-active battery electrodes. The uniform application of the polymer electrolyte is done in solution by the direct electropolymerization of electrochemically-active monomers.

The first system explored was the reductive electropolymerization of a zinc vinyl-bipyridine complex $[\text{Zn}(\text{vbpy})_3]^{2+}$. The electrochemical synthesis covered the surface of planar and nanowire electrodes. Uniform deposition was observed by XPS and

electrochemical “redox-probe” experiments. During the electropolymerization, the potentiodynamic cycle number determined the height of the polymer on the surface of a tin-doped indium-oxide (ITO) electrode. The thickness of the polymer was measured with an AFM “scratch” method and by SEM profiling. A relationship between the dielectric window and thickness of $pZn(vbpy)_3$ exemplified how the physical characteristics of a polymer electrolyte are closely tied to the electrical characteristics.

The second system of interest was the reductive “electrografting” of polymers with vinyl moieties. The reductive electropolymerization of glycidyl methacrylate (GMA) on two-dimensional electrodes was successful, but the conversion to nanowires is on-going research. Solid-state ionic conductivity, tested with a liquid metal eutectic, was observed on Cu_2Sb . Ion transport was induced by soaking the polymer in a 1M $LiClO_4/PC$ solution and drying. Cu_2Sb modified with $pGMA$ can charge and discharge in solution-based battery testing, but salt-clustering, observed with optical microscopy, in the solid-state displayed inhomogeneous regions of ionic conductivity for $pGMA:LiClO_4$.

Copolymerization, an *in situ* doping method, was required to uniformly distribute Li-ions throughout the SPE. The first step towards copolymerization was an in-depth analysis of the homopolymerization of an anionic monomer. Potassium 3-sulfopropyl acrylate (KSPA), soluble in water, was reductively polymerized onto multiple electrode surfaces. The growth was observed electrochemically and spectroscopically (UV-Vis). The reduction potential of the monomer on different electrodes was dependent on the work function of the material, but all depositions of $pKSPA$ were non-uniform and electrically conducting. AFM and XPS measurements taken on polymer-modified ITO electrodes were the basis for the electrochemical island growth of anionic polymers.

Electrochemical co-reduction of *p*GMA with an anionic monomer, *p*LiMA, uniformly deposited a polymeric layer. A “sweep-step” deposition potential profile successfully incorporated both monomers uniformly. ATR-IR spectroscopy provided some evidence for copolymerization. The curve-fitting analysis of the C 1s and Li 1s XPS HRES scans definitively evidenced the presence of *p*GMA-*co-p*LiMA on the surface of Cu₂Sb. Variable-temperature solid-state impedance results indicated that the T_g of the copolymer must be lowered to increase the ionic conductivity. If SPEs are to be used in Li-ion batteries, then they must perform as well as common liquid organic electrolytes.

However, the decomposition of carbonate-based solvents for Li-ion batteries also offered a route to a solid-state electrolyte. The decomposition of liquid electrolytes commonly used for batteries, such as propylene carbonate (PC), ethylene carbonate (EC), and dimethyl carbonate (DMC), produce a solid-electrolyte interface (SEI) layer on the surface of the all battery anode and cathodes. However, capacity retention was improved with the inclusion of the vinylene carbonate (VC) as an additive to the liquid electrolyte. XPS HRES curve-fitting analysis illustrated the inclusion of organo-lithium salts into the SEI when galvanostatically cycled. The solid-state electrical properties of the SEI were dependent on the growth methods, the number of growth cycles and the potentials chosen for growth. Solid-state ionic conductivity was established by choosing the correct electrochemical parameters.

Finding an effective storage medium is a significant challenge facing practical use of hydrogen as a fuel source. Light metal hydrides, such as MgH₂, are a proposed solution for the efficient storage of H₂ gas. The size of the solution-synthesized magnesium nanocrystals (MgNCs) was controlled by chemical composition of the

reducing solution and the concentration of the magnesium precursor, magnesocene. The MgNCs are characterized by XRD and TEM. Extremely fast sorption kinetics is hypothesized to be due to the high-number of defect sites in the crystalline metal-hydride. The activation energy for H/D processes did not significantly change from bulk Mg.

The first solution-based *in-situ* doping of MgNCs with nickel (1, 5, and 20 wt%) was accomplished with our synthetic methods. Nickel metal is a popular choice of dopant for Mg because it is cheap (\$3.20/g – Sigma Aldrich), light (compared to 2nd and 3rd row TMs), and alloys with Mg to form another H₂-storage material, Mg₂Ni. Ni also has a large nuclear cross-section, which permits small amounts to be detected with neutron diffraction (in collaboration with Dr. Steve Conradson at LANL). The presence of Ni⁰ on the surface of the Mg NCs was detected by XPS measurements, though no crystalline Ni_(m) was ever seen with XRD.

A computer-controlled H/D system, based on Seivert's method, was built to measure the adsorption and desorption capabilities of the MgNCs. A significant improvement in the adsorption kinetics was expressed by the large decrease in E_a from the undoped Mg NCs (81.9 kJ/mol) to the 5 wt% Ni-doped MgNCs (15.9 kJ/mol). The adsorption and desorption isotherms of undoped samples displayed a much slower rate with increasing H/D cycles. The doped samples, even as low as 1 wt%, retained the same rates with cycle number. A proposed mechanism for the formation of catalytic Ni⁰ on the surface of MgNCs is presented in this dissertation.

Timothy S. Arthur
Department of Chemistry
Colorado State University
Fort Collins, CO 80523
Summer 2010

ACKNOWLEDGEMENTS

The work I have accomplished in the last five years would not have been possible without the hard work, support and love of many people. First, I must thank Professor Amy “Boss” Prieto for letting me be part of the beginning of her very long and successful career. Not many graduate students can say that they had a hand in building a lab (even though Nick and I tried our hardest to accidentally burn it down at times) and a hand in the start-up of the successful *Prieto Battery Inc.* I am truly grateful for the opportunity to work with you and for the doors working in your group has opened for me and my family. I am hopeful that our ties will remain strong through the years.

I asked my wife, Maria, if she wanted me to put her name on the front of this dissertation next to mine...the graduate school wouldn't allow it. Her never-ending love, her up-beat nature and her timely nuggets of wisdom (“you need to sleep to learn”) will continue to propel our family forward. I also forgot to mention her during my 4th-year research seminar, one of my biggest graduate school regrets.

The friendships formed in graduate school are forged in the fires of science, research, teaching, mental breakdowns, and emotional tipping-points. Mark Oinen, the tallest groomsmen ever-made, would share first-year trials, tribulations and a box of doughnuts with me on the first Saturday morning of every month. Vast amounts of knowledge and mass was gained during cumes.

My close friends in the Prieto group will remain my close friends. James Mosby tireless dedication to the battery cannot be matched, I only tried to keep up. Derek Johnson's willingness to teach younger scientists his engineering savvy is priceless. Shannon Riha's work-ethic is unparalleled, though my fondest memories will be our battles

against our arch-enemy, the glovebox. Nick Norberg started all the work with the magnesium nanocrystals, a foundation that hopefully continues to be built upon. Dan Shissler (Arr) helped to build the hydrogen storage system. Dan Bates has willingly taken reins of the polymer electrolyte project. I am saddened to be leaving such an intelligent and friendly group of people.

My gratefulness extends to all the people in the chemistry department that took part in my education. Dr. Pat McCurdy has spent hours on end helping me with XPS. All the scientists in the CIF are keystones for the entire department. Ron Costello has built stands, fixed pumps and drilled holes in things that have made my research easier, if not possible. I also know more about the Broncos than most Coloradoans.

The Elliott group has also been a large part of my life here at CSU, and although I am not an official member, I will continue to butt my way into the Steam-boat ski trip. When I first arrived, Mike “Can Crusher” Scott, Mike “Blue” Green, Matt Rawls (currently with *Prieto Battery*) and Jeremy Nelson welcomed me into the lab and into Fort Collins.

Mike Elliott is a huge part of my success at CSU. I am forever grateful for a great many things, and I could never do them all justice in one acknowledgment section. Thank-you for letting me live in your house rent-free so I could start me research career early in 2005. Thank-you for all the potentiostat availability, electrodes, chemicals, beer, steaks and advice you willingly gave to a very young Prieto Group. Thank-you for the tickets to some of the best seats at Coors field. But most of all, thank-you for always having your door open to me.

Finally, I want to thank everybody else who gave me this amazing opportunity.

TABLE OF CONTENTS

PART I: ELECTROREDUCTIVE POLYMERIZATION OF NANOSCALE SOLID POLYMER ELECTROLYTES FOR THREE-DIMENSIONAL LITHIUM-ION BATTERIES

CHAPTER 1	1
<hr/> <i>THE PRIETO GROUP'S LI-ION BATTERY DESIGN: IMPLICATIONS FOR POLYMER ELECTROLYTES</i>	
1.1 - THE PRIETO GROUP'S LI-ION BATTERY DESIGN	2
1.2 - REQUIREMENTS OF A POLYMER ELECTROLYTE ON THE SURFACE OF Cu_2S NANOWIRES	6
1.3 - ELECTROPOLYMERIZATION AS A ROUTE TO CONFORMAL COATINGS OF ELECTRODE SURFACES	10
1.4 - REFERENCES	12
CHAPTER 2	14
<hr/> <i>CONFORMAL COATINGS OF NANOWIRE ARRAYS VIA ELECTROREDUCTIVE POLYMERIZATION</i>	
2.1 - ABSTRACT	15
2.2 - THE ELECTROPOLYMERIZATION OF $[\text{Zn}(\text{VBPY})_3]^{2+}$ ON 3D SURFACES	15
2.3 - EXPERIMENTAL	16
2.4 - PHYSICAL CHARACTERIZATION AND SOLID-STATE ELECTRICAL MEASUREMENTS	20
2.5 - DISCUSSION AND CONCLUSIONS	30
2.6 - REFERENCES	31
CHAPTER 3	32
<hr/> <i>REDUCTIVE ELECTROPOLYMERIZATION OF ACRYLATE MONOMERS FOR LI-ION BATTERIES</i>	
3.1 - INTRODUCTION	33
3.2 - EXPERIMENTAL	38
3.3 - THE ELECTROPOLYMERIZATION OF GMA	42
3.4 - PHYSICAL CHARACTERIZATION OF PGMA	46
3.5 - SOLID-STATE ELECTRICAL MEASUREMENTS OF PGMA-MODIFIED ELECTRODES	52
3.6 - DISCUSSION	57
3.7 - THE AQUEOUS ELECTROPOLYMERIZATION OF KSPA	59
3.8 - PHYSICAL CHARACTERIZATION OF PKSPA	62
3.9 - SOLID-STATE ELECTRICAL MEASUREMENTS OF PKSPA-MODIFIED ELECTRODES	67
3.10 - DISCUSSION	68
3.11 - TOWARDS ELECTRO-COPOLYMERIZATION OF POLYMER ELECTROLYTES FOR LI-ION BATTERIES	72
3.12 - THE ELECTROPOLYMERIZATION OF LIMA	73
3.13 - THE ELECTROPOLYMERIZATION OF PGMA-CO-PLIMA	75
3.14 - PHYSICAL CHARACTERIZATION OF PGMA-CO-PLIMA	76
3.15 - SOLID-STATE ELECTRICAL MEASUREMENTS OF PGMA-CO-PLIMA	84
3.16 - TEMPERATURE DEPENDENT SOLID-STATE ELECTRICAL MEASUREMENTS OF PGMA-CO-PLIMA	85
3.17 - DISCUSSION AND CONCLUSIONS	86
3.18 - REFERENCES	88

CHAPTER 4 **90**
*THE DECOMPOSITION OF LI-ION BATTERY LIQUID ELECTROLYTES ON Cu_2S : SEI
FORMATION AS A ROUTE TO A SOLID ELECTROLYTE*

4.1 - ABSTRACT	91
4.2 - DECOMPOSITION OF LIQUID ELECTROLYTES ON BATTERY ELECTRODE SURFACES	91
4.3 - EXPERIMENTAL	94
4.4 - PHYSICAL CHARACTERIZATION OF A SEI ON Cu_2S	98
4.5 - DISCUSSION AND CONCLUSIONS	103
4.6 - REFERENCES	111

PART II: PHYSICAL CHARACTERIZATION AND HYDROGEN SORPTION
KINETICS OF SOLUTION-SYNTHESIZED MAGNESIUM NANOPARTICLES

CHAPTER 5 **114**
*SIZE-DEPENDENT HYDROGEN STORAGE PROPERTIES OF MG NANOCRYSTALS
PREPARED FROM SOLUTION*

5.1 - INTRODUCTION	115
5.2 - EXPERIMENTAL	116
5.3 - PHYSICAL CHARACTERIZATION OF MAGNESIUM NANOCRYSTALS	116
5.4 - HYDROGEN ABSORPTION/DESORPTION PROPERTIES OF MAGNESIUM NANOCRYSTALS	118
5.5 - CONCLUSIONS	121
5.6 - NOTES ON CALCULATIONS OF REACTION RATES AND ACTIVATION ENERGIES	122
5.7 - REFERENCES	124

CHAPTER 6 **125**
*SOLUTION-SYNTHESIZED MAGNESIUM NANOCRYSTALS: IN SITU DOPING WITH $\text{Ni}_{(M)}$,
PHYSICAL CHARACTERIZATION AND H_2 -STORAGE PROPERTIES*

6.1 - INTRODUCTION	126
6.2 - EXPERIMENTAL	128
6.3 - PHYSICAL CHARACTERIZATION AND SORPTION MEASUREMENTS	132
6.4 - THE FORMATION OF Ni^0 ON THE SURFACE OF MAGNESIUM NANOCRYSTALS	142
6.4 - CONCLUSIONS	146
6.5 - REFERENCES	148

PART I: ELECTROREDUCTIVE POLYMERIZATION OF NANOSCALE SOLID POLYMER
ELECTROLYTES FOR THREE-DIMENSIONAL LITHIUM-ION BATTERIES

Chapter 1

The Prieto Group's Li-ion battery design: Implications for polymer electrolytes

1.1 The Prieto Group's Li-ion battery design

As global energy requirements increase at an alarming rate, so does the demand for safe, portable and high-energy devices to power the new-age of electronics¹. High gravimetric and volumetric energy densities make lithium-ion (Li-ion) batteries an excellent electrochemical energy storage medium. A part of society where Li-ion batteries can make an immediate, meaningful impact is the transportation sector²⁻³. Electric vehicles require a portable, safe and rechargeable energy storage medium with high charge/discharge rates, high voltage and high capacity properties. One avenue of battery research has focused on finding new battery materials⁴⁻⁶. New electrodes with high-storage capacities and new electrolytes with fast Li-ion transport are pushing the frontier of the Li-ion battery capability. However, science has recently taken a large interest in the, sometimes radical, change in properties exhibited by physically restraining the size of known materials^{4,7-9}. Nanoparticle solar cells¹⁰, nanowire sensors¹¹⁻¹², nanostructured electrochemical electrodes¹³ and nanocrystal H₂-storage materials¹⁴ are promising areas of energy research.

A route to improving battery performance is to transition from two-dimensional (2D) thin-film technologies to three-dimensional (3D) battery architectures. For Li-ion batteries, nanowire array (NWA) electrode materials have recently displayed capacity-retention at extremely fast rates, capacity-retention at high cycle numbers and high-power capabilities¹⁵⁻²². These exciting results are due to the larger effective surface area and the short diffusion distance of Li⁺ within the nanowires. Detrimental volume changes of the battery electrodes, or pulverization, cause a drop in capacity of thin-film batteries, but nanowires are physically less affected by the chemical intercalation/deintercalation of Li⁺

ions²³. The ground-up fabrication of a NWA electrode is the first step to completely understanding the ion-diffusion, electric field gradients and electron transport in a 3D nanowire battery.

The construction of the Prieto Group electrochemical device relies on solution-based electrochemical methods. First, an anodic alumina (AAO) template is anodized from Al_(m) under specific conditions. Periodic, nanometer scale pores grow during the anodization process until a solid, porous and insulating ceramic, Al₂O₃, is formed on a thin layer of Al_(m). Prieto²⁴ details the process intricately, and current research in our lab involves controlling pore dimensions and pore spacing. Dissolution of the remaining metal and thermal evaporation of a metal contact onto the surface of the pores concludes the fabrication of a conductive template for nanowire deposition. Figure 1.1 outlines the next three steps in the process: anode nanowire growth, template dissolution, and the electrochemical polymerization of a solid-polymer electrolyte. Finally, the battery is completed when a cathode material, such as LiCoO₂, is integrated between the nanowires and electrical contact is made to the cathode. The single-potential deposition of Cu₂Sb, our chosen anode material, is outlined by Mosby *et al.*²⁵ We are currently synthesizing and testing Cu₂Sb nanowires.

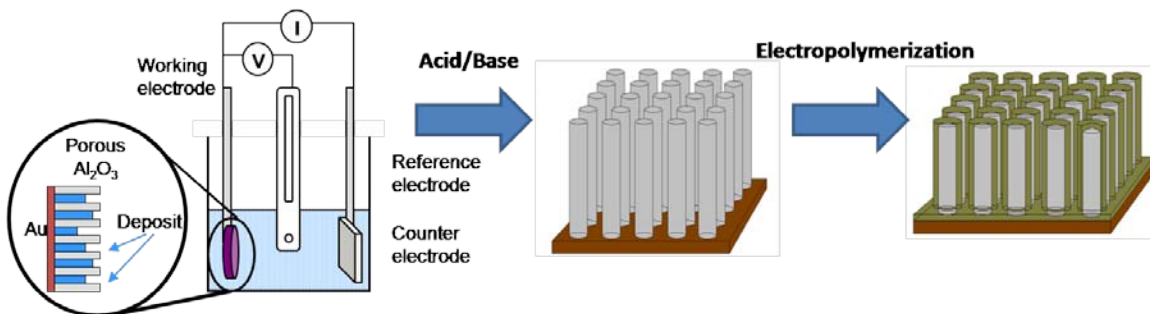


Figure 1.1. Electrodeposition of anode nanowires (left), release of the nanowires by Al₂O₃ dissolution (middle), and electropolymerization onto the NWA electrode (right). All three steps are part of the 3 D battery construction. Figure adapted from Prieto

In a 2004 review, Rolison *et al.*²⁶ outline the advantages of moving away from thin-film batteries, such as a significant increase in surface area between the electrodes and the electrolyte. The increase in interfacial surface area inherently increases the number of sites a Li-ion can inject from the electrode (electrolyte) to the electrolyte (electrode). The concept is expressed pictorially in Figure 1.2. If we assume a conservative 10^{10} nanowires/cm² for the electrochemical growth of nanowires within the pores of AAO (reports range from 10^{10} to 10^{12} nanowires/cm²)^{23,27-28}, then the areal footprint of a thin-film electrode has to be ~66 times larger than the NWA electrode to achieve the same geometric surface area. The calculation is based on a 200 nm diameter wire that is 1 μ m in length, but both of those physical dimensions are adjustable during AAO anodization.

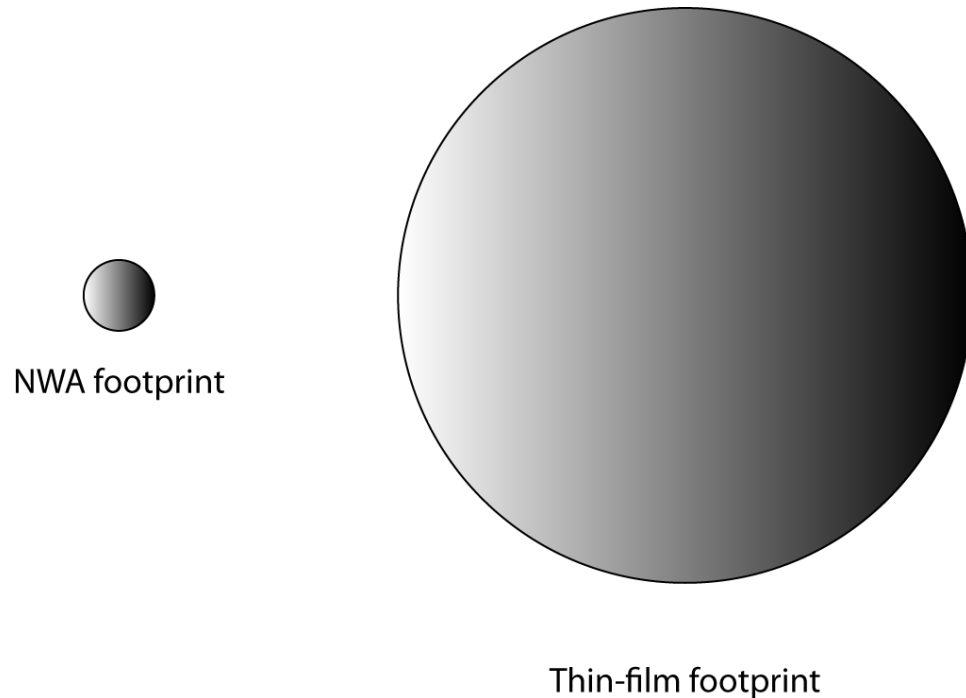


Figure 1.2. Footprint comparison between a NWA electrode and a thin film electrode. Both electrodes have the same effective surface area. The calculation is based on nanowires with $d = 200$ nm and $l = 1$ μ m, and assuming 10^{10} nanowires/cm² (footprint).

A battery is a series of electrically-coupled electrochemical cells. Reduction and oxidation (Redox) reactions of battery electrodes determine the energy of a dissociated electron (V_{oc} - Figure 1.3). During discharge, the anode is oxidized and releases a Li^+ into the electrolyte. Simultaneously, a Li^+ is injected into the cathode as the electrode is reduced. The reverse process occurs when the battery is charged, only the electrical current is supplied by an external power source. Ideally, the HOMO/LUMO separation, or thermodynamic window, of a polymer electrolyte (E_g) is larger than the open-circuit potential (V_{oc}) of the battery; that is, the electrolyte should be electrochemically non-reactive during battery operation. The role of the electrolyte is to efficiently transport Li -ions between electrodes while maintaining electrical insulation. The challenge is to apply the electrolyte onto the surface of the nanowires.

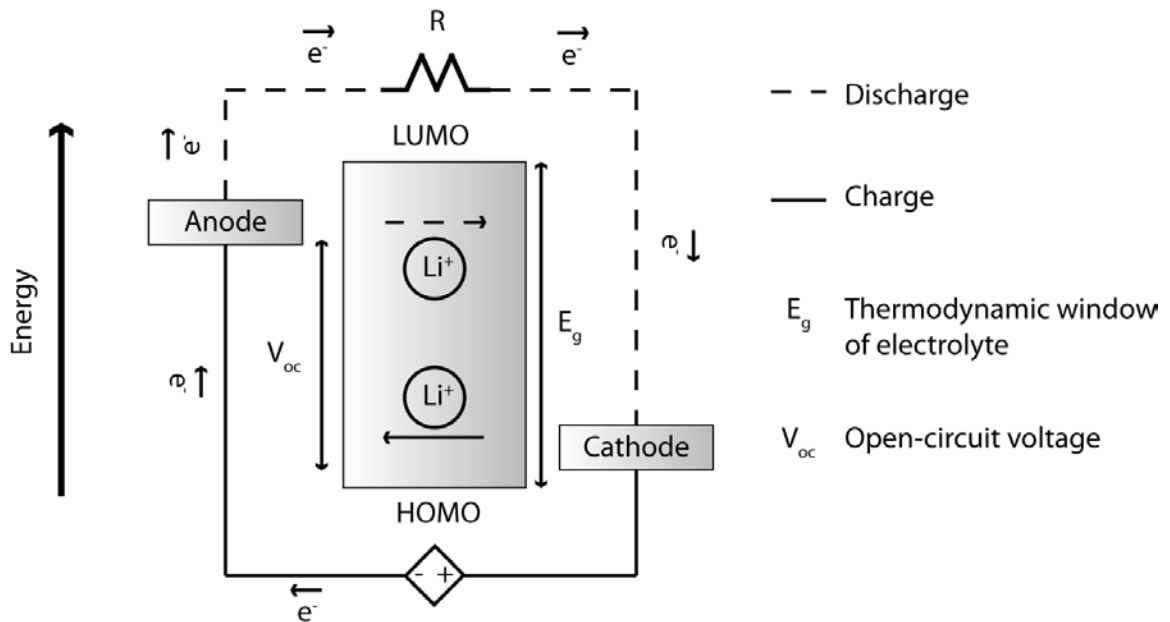


Figure 1.3. Schematic open-circuit energy diagram of a Li-ion battery electrolyte. The flow of the electrons and Li-ions is shown as the battery is charged and discharged.

The capability to apply a thin, uniform layer is the pivotal step before the integration of the cathode material.^{26,29-30} A point of ohmic contact between the positive and negative electrodes is an electrical short; a low resistance pathway for electrons to flow instead of the intended load, R (Figure 1.3). A functional nanowire architecture is dependent on the uniformity of a polymer electrolyte, but the thickness of the layer is also very important. Fast Li-ion transport between electrodes facilitates quick charge and discharge of the material, and a decrease in the mass of non-electroactive component will improve the gravimetric capacity.

1.2 Requirements of a polymer electrolyte on the surface of Cu₂Sb nanowires

The science of polymer electrolytes stretches across many disciplines; polymer science, organic chemistry, inorganic chemistry and electrochemistry. In general, polymer electrolytes for Li-ion batteries require the following:³¹

1. The polymer must be electrically insulating ($\sigma_e < 10^{-10}$ S/cm) to minimize self-discharge of the battery.
2. The polymer must conduct Li-ions between electrodes. Reports vary, but most agree that acceptable electrolytes have a ionic conductivity $\sigma_{ion} > 10^{-4}$ S/cm and a transference number $t_{Li}^+ \approx 1$ (i.e., the majority of ion-flow must be due to Li-ion transport).³⁰⁻³⁴ However, in size regimes below < 500 nm, the overlap of electrical double layers can significantly alter the transportation of ions.
3. The polymer must have a wide electrical window (> 4.0 V), so that electrolyte degradation does not occur within the working potentials of the electrodes.
4. The polymer must be physically robust.
5. The polymer must be chemically inert.

Preferably, polymer electrolytes must also be safe, non-toxic and cheap. However, none of those characteristics are required for a polymer electrolyte to function. Safety

concerns are partially addressed because most polymers have a much higher flash point than organic liquid electrolytes, and the solid layer also physically inhibits $\text{Li}_{(m)}$ dendritic growth.

Currently, polymer electrolytes are based on *poly*-ethylene oxide (PEO).³⁵⁻³⁷ The initial transportation of Li-ions, discovered by Fenton *et al.*³⁸, has set the standard for separator technology since 1972. The polymers dissolution of Li-based salts, due to the slight negative charge of the ether based linkages, is vital to battery operation. PEO's structure is part of our motivation for choosing *poly*-glycidyl methacrylate (Chapter 3) as a target polymer. However, PEO does have drawbacks:³⁹⁻⁴¹ 1) PEO does not work as a dry polymer electrolyte, that is, it requires a liquid component to achieve acceptable ionic conductivity, 2) low-molecular weight PEO requires high operational temperatures (> 60 °C) to function, and (3) PEO has not been electrochemically formed on the surface of electrodes. Electropolymerization is a key part to our proposed solution (Chapter 1.3), but not all monomers can be electrochemically reduced onto the surface of electrodes. Using known systems is a method to partially screen the large library of monomers.

The list of requirements is daunting, and all the challenges are difficult to solve simultaneously. However, electrical insulation is an intrinsic property of most polymers that lack continuous pi-conjugation. The solid, aliphatic layer provides sufficient electrical insulation for high-energy, lithium-ion battery electrodes, but also severely decreases the ionic conductivity (as compared to liquid electrolytes). To remedy this issue, research has focused on the formation of gel-polymer electrolytes (GPEs), liquid systems trapped in a polymeric matrix.^{34,41} Current research in our lab involves modifying electrodeposited layers to form GPEs.

The application of the polymer electrolyte directly to the 3D electrode surface is an interesting challenge. Solution-cast and vapor-deposited solid electrolyte layers are typically $\geq 1 \mu\text{m}$ or cannot be applied to large surface areas, electrostatic layer-by-layer assemblies are not completely pin-hole free and require a long time to prepare, and the physical and electrical characteristics of self-assembled monolayers (SAMS) are very surface specific.²⁶ The challenge is compounded by the limitations of the architecture. The nanometric spacing of electrodes requires the application of an ultra-thin layer to maximize the short Li-ion diffusion from anode to cathode. Optimization of battery dimensions will ultimately be a combination of calculations: 1) matching anode and cathode volumetric capacity, 2) balancing ohmic losses in nanowire conductivity with nanowire length, and 3) maintaining electrical insulation between electrodes. Figure 1.4 illustrates how certain properties of a polymer electrolyte will effect Li-ion diffusion. In the ideal case, Figure 1.4a, the polymer electrolyte thickness is optimized so that Li-ion diffusion is one-dimensional and uniform along the surface of the nanowire. If the polymer electrolyte is too thin, Figure 1.4b, then electron tunneling through the dielectric, quick self-discharge of the electrodes and shorting of the battery are all possible detriments to battery characteristics and/or operation. If the electrolyte is too thick, Figure 1.4c, then the usefulness of the nanowire electrodes is diminished by preferential diffusion of Li-ions. In this case, the diffusion length through the electrolyte is shortest between the tips of nanowires, and Li-ions will selectively diffuse across the least resistive pathway. The non-uniform diffusion of Li-ions decreases the power and rate capabilities of the battery below a thin film electrode of the same footprint. The

detrimental effects are caused by the smaller effective surface area of the battery and the added weight of the ineffective polymer electrolyte.

Uniform Li-ion diffusion can also be disrupted by chemical inhomogeneities in polymer films. Mixed-polymer systems and salt-doped polymer systems, synthesized *in situ* or physically mixed in solution, have regions of high and low ionic conductivity. The concept has been portrayed through nanoscale conductivity measurements (performed with a conducting-probe AFM), TEM/EDX *in situ* mapping of ion-dynamics, and theoretical simulations. Physical uniformity must be matched by chemical homogeneity of the polymer electrolyte. One method to achieve uniformity is to homopolymerize an ionically conducting polymer (Chapter 2 and Chapter 3); however, pathways of preferred ionic conductivity are unavoidable in mixed systems. The challenge is to dimensionally minimize regions of low ionic-conductivity and to uniformly distribute the regions.

The final limitation for the successful deposition of a polymer electrolyte is the electrochemical stability of the anode, Cu_2Sb . In aqueous solutions, cyclic voltammograms of Cu_2Sb show a stripping peak at $E_{\text{pa}} = 0.125 \text{ V}$ (vs SSCE), but the onset of oxidation current begins at $E_{\text{o}} \approx -0.5 \text{ V}$ (vs SSCE). The Cu_2Sb electrode potential must remain at more reducing potentials, $< -0.5 \text{ V}$ (vs SSCE), to avoid electrochemical stripping of the anode material from the current collector. Cu_2Sb stripping potentials narrow the voltage window for the chosen deposition method, electropolymerization; that is, monomers must be electrochemically polymerized from solution without oxidizing the anode.

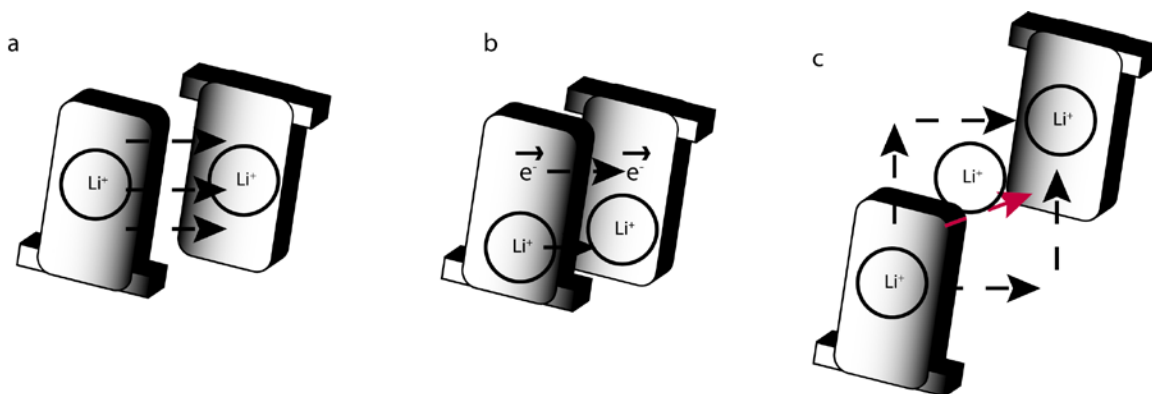


Figure 1.4. Li-ion diffusion between NWA battery electrodes when a) the spacing between the electrodes is optimized, b) the spacing between the electrodes is too thin, and c) the spacing between the electrodes is too thick.

1.3 Electropolymerization as a route to conformal coatings of electrode surfaces

Though the literature is extensive for the electro-synthesis of insulating or conducting polymers, the reductive polymerization and subsequent testing of a solid electrolyte onto the surface of an intermetallic electrode is unexplored. Electropolymerization is a soft-chemistry route to modification of electrode surfaces with high-surface area and non-linear of sight geometries⁴²⁻⁴⁴. Surface modification through electrochemical means can be accomplished through oxidation or reduction of either the monomer, or an initiator, in solution. The electrochemistry has been extensively studied for the electrochemical growth of polythiophenes and polyanilines, as well as work done with the electropolymerization of metal vinyl-bipyridine (vbpy) complexes reported by Murray *et al.* Since their discovery in the early 1980's⁴⁵⁻⁵², the electropolymerization of metal complexes with vbpy ligands have been studied as optical layers, within GPE's and as agents for kinetic control of catalytic reactions at electrode surfaces. More recently, Rolison *et al.* used self-limiting electropolymerization as a means to uniformly modify

the micropores of MnO₂ aerogel electrodes. That research has been extended to the fabrication of a nanocapacitor with exceptional properties.⁵³ Other groups have synthesized nanotubes and nanowires of conducting polymers by electrochemical polymerization within the pores of various ceramics.^{4,8,11}

We hypothesize that reductive electropolymerization is an effective method to apply a polymer electrolyte to the surface of Cu₂Sb. Ionic functionality in dielectric polymer layers can be achieved through the following: 1) chemical functionalization of grown polymer films (Chapter 2), 2) salt-impregnation (Chapter 3.5), and 3) copolymerization with an anionic monomer (Chapter 3.11). The advantages and draw-backs to each option are explored later in this dissertation. A library of reductively electropolymerizable monomers can be found by researching the literature, a natural starting point for our investigation. By conducting new experiments on known/slightly modified systems, we can explore the validity of our hypothesis and make significant progress towards the production of a 3D Li-ion battery.

1.4 References

- (1) Tarascon, J. M.; Armand, M. *Nature* **2001**, *414*, 359.
- (2) MacLean, H. L.; Lave, L. B. *Progress in Energy and Combustion Science* **2003**, *29*, 1.
- (3) Shukla, A. K.; Arico, A. S.; Antonucci, V. *Renewable & Sustainable Energy Reviews* **2001**, *5*, 137.
- (4) Arico, A. S.; Bruce, P.; Scrosati, B.; Tarascon, J. M.; Van Schalkwijk, W. *Nature Materials* **2005**, *4*, 366.
- (5) Bruce, P. G.; Scrosati, B.; Tarascon, J. M. *Angewandte Chemie-International Edition* **2008**, *47*, 2930.
- (6) Wakihara, M. *Materials Science & Engineering R-Reports* **2001**, *33*, 109.
- (7) Grimsdale, A. C.; Mullen, K. *Angewandte Chemie-International Edition* **2005**, *44*, 5592.
- (8) Kamat, P. V. *Journal of Physical Chemistry C* **2007**, *111*, 2834.
- (9) Ogden, J. M. *Annual Review of Energy and the Environment* **1999**, *24*, 227.
- (10) Riha, S. C.; Parkinson, B. A.; Prieto, A. L. *Journal of the American Chemical Society* **2009**, *131*, 12054.
- (11) Kiefer, R.; Chu, S. Y.; Kilmartin, P. A.; Bowmaker, G. A.; Cooney, R. P.; Travas-Sejdic, J. *Electrochimica Acta* **2007**, *52*, 2386.
- (12) Liu, H. Q.; Kameoka, J.; Czaplewski, D. A.; Craighead, H. G. *Nano Letters* **2004**, *4*, 671.
- (13) White, R. J.; White, H. S. *Langmuir* **2008**, *24*, 2850.
- (14) Norberg, N.; Arthur, T. S.; Prieto, A. L. *Journal of the American Chemical Society*, In preparation.
- (15) West, W. C.; Myung, N. V.; Whitacre, J. F.; Ratnakumar, B. V. *Journal of Power Sources* **2004**, *126*, 203.
- (16) Li, X. X.; Cheng, F. Y.; Guo, B.; Chen, J. *Journal of Physical Chemistry B* **2005**, *109*, 14017.
- (17) Xie, Y.; Wu, C. Z. *Dalton Transactions* **2007**, 5235.
- (18) Bruce, P. G. *Solid State Ionics* **2008**, *179*, 752.
- (19) Chan, C. K.; Peng, H. L.; Liu, G.; McIlwrath, K.; Zhang, X. F.; Huggins, R. A.; Cui, Y. *Nature Nanotechnology* **2008**, *3*, 31.
- (20) Chan, C. K.; Zhang, X. F.; Cui, Y. *Nano Letters* **2008**, *8*, 307.
- (21) Li, Y. G.; Tan, B.; Wu, Y. Y. *Nano Letters* **2008**, *8*, 265.
- (22) Chan, C. K.; Ruffo, R.; Hong, S. S.; Cui, Y. *Journal of Power Sources* **2009**, *189*, 1132.
- (23) Vullum, F.; Teeters, D. *Journal of Power Sources* **2005**, *146*, 804.
- (24) Prieto, A. L. *Dissertation*.
- (25) Mosby, J. M.; Prieto, A. L. *Journal of the American Chemical Society* **2008**, *130*, 10656.
- (26) Long, J. W.; Dunn, B.; Rolison, D. R.; White, H. S. *Chemical Reviews* **2004**, *104*, 4463.
- (27) Gelves, G. A.; Murakami, Z. T. M.; Krantz, M. J.; Haber, J. A. *Journal of Materials Chemistry* **2006**, *16*, 3075.
- (28) Green, S.; Cortes, A.; RiveroS, G.; Gomez, H.; Dalchiele, E. A.; Marotti, R. E. In *Physica Status Solidi C - Current Topics in Solid State Physics, Vol 4, No 2*; Stutzmann, M., Ed. 2007; Vol. 4, p 340.
- (29) Dias, F. B.; Plomp, L.; Veldhuis, J. B. J. *Journal of Power Sources* **2000**, *88*, 169.
- (30) Xu, K. *Chemical Reviews* **2004**, *104*, 4303.
- (31) Ahmad, S. *Ionics* **2009**, *15*, 309.
- (32) Meyer, W. H. *Advanced Materials* **1998**, *10*, 439.
- (33) Quartarone, E.; Mustarelli, P.; Magistris, A. *Solid State Ionics* **1998**, *110*, 1.
- (34) Song, J. Y.; Wang, Y. Y.; Wan, C. C. *Journal of Power Sources* **1999**, *77*, 183.
- (35) Sirisopanaporn, C.; Fericola, A.; Scrosati, B. *Journal of Power Sources* **2009**, *186*, 490.
- (36) Syzdek, J.; Armand, M.; Gizowska, M.; Marcinek, M.; Sasim, E.; Szafran, M.; Wieczorek, W. *Journal of Power Sources* **2009**, *194*, 66.
- (37) Zhu, C. B.; Cheng, H.; Yang, Y. *Journal of the Electrochemical Society* **2008**, *155*, A569.
- (38) Fenton, D. E.; Parker, J. M.; Wright, P. V. *Polymer* **1973**, *14*, 589.
- (39) Fericola, A.; Weise, F. C.; Greenbaum, S. G.; Kagimoto, J.; Scrosati, B.; Soletto, A. *Journal of the Electrochemical Society* **2009**, *156*, A514.

- (40) Hassoun, J.; Panero, S.; Reale, P.; Scrosati, B. *Advanced Materials* **2009**, *21*, 4807.
- (41) Niedzicki, L.; Kasprzyk, M.; Kuziak, K.; Zukowska, G. Z.; Armand, M.; Bukowska, M.; Marcinek, M.; Szczecinski, P.; Wieczorek, W. *Journal of Power Sources* **2009**, *192*, 612.
- (42) Rhodes, C. P.; Long, J. W.; Doescher, M. S.; Fontanella, J. J.; Rolison, D. R. *Journal of Physical Chemistry B* **2004**, *108*, 13079.
- (43) Rhodes, C. P.; Long, J. W.; Rolison, D. R. *Electrochemical and Solid State Letters* **2005**, *8*, A579.
- (44) Talbi, H.; Just, P. E.; Dao, L. H. *Journal of Applied Electrochemistry* **2003**, *33*, 465.
- (45) Denisevich, P.; Abruna, H. D.; Leidner, C. R.; Meyer, T. J.; Murray, R. W. *Inorganic Chemistry* **1982**, *21*, 2153.
- (46) Abruna, H. D.; Breikss, A. I.; Collum, D. B. *Inorganic Chemistry* **1985**, *24*, 987.
- (47) Meyer, T. J.; Sullivan, B. P.; Caspar, J. V. *Inorganic Chemistry* **1987**, *26*, 4145.
- (48) Elliott, C. M.; Baldy, C. J.; Nuwaysir, L. M.; Wilkins, C. L. *Inorganic Chemistry* **1990**, *29*, 389.
- (49) Surridge, N. A.; Keene, F. R.; White, B. A.; Facci, J. S.; Silver, M.; Murray, R. W. *Inorganic Chemistry* **1990**, *29*, 4950.
- (50) Gould, S.; Strouse, G. F.; Meyer, T. J.; Sullivan, B. P. *Inorganic Chemistry* **1991**, *30*, 2942.
- (51) Bommarito, S. L.; Lowerybretz, S. P.; Abruna, H. D. *Inorganic Chemistry* **1992**, *31*, 502.
- (52) Bommarito, S. L.; Lowerybretz, S. P.; Abruna, H. D. *Inorganic Chemistry* **1992**, *31*, 495.
- (53) Liu, X. M.; Zhang, R.; Zhan, L.; Long, D. H.; Qiao, W. M.; Yang, J. H.; Ling, L. C. *New Carbon Mater* **2007**, *22*, 153.

Chapter 2

Conformal coating of nanowire arrays via electroreductive polymerization

Timothy S. Arthur and Amy L. Prieto

This dissertation chapter is adapted from a manuscript submitted to *Nanotechnology*

2.1 Abstract

One of the major challenges facing the development of nanoscale devices is the ability to uniformly modify high-aspect ratio electrodes. Here, we utilize electroreductive polymerization as a route to conformally coat high aspect ratio nanowire arrays as a step towards the incorporation of ultrathin polymer coatings on high surface area electronic devices.

2.2 Introduction

There are many examples of high-surface area materials that exhibit improved performance over their bulk counterparts, particularly for applications where a small footprint is desired¹. Though significant advancements have been made in the realm of nanostructured inorganic materials²⁻⁴, new work has focused on the incorporation of polymer electrolytes at small length scales.⁵⁻⁷ Key to the incorporation of polymer electrolytes onto high surface area electrodes is conformal coating with the absence of pinhole defects, which could lead to electrical shorts or inhomogeneous electric fields or ionic diffusion rates⁸.

Electropolymerization is a powerful route to coating electrodes for use as actuators⁹, capacitors¹⁰, sensors¹¹, and batteries¹. The ability to uniformly modify three dimensional surfaces and control the thickness of the polymer layer is an essential step to creating a conformal coating on conducting substrates. These coatings can be electrically or ionically insulating or conductive, depending on the desired applications. Here we show that the electropolymerization of *poly*-[Zn(4-vinyl-4'-methyl-2,2'-bipyridine)₃](PF₆)₂ results in the conformal coating of high aspect ratio nanowire arrays without the presence

of pinhole defects. This polymer adheres well to a variety of nanowires, exhibits a large breakdown voltage (making it a very good dielectric coating), and can be tuned in thickness.

We chose $[\text{Zn}(4\text{-vinyl-4}'\text{-methyl-2,2}'\text{-bipyridine})_3](\text{PF}_6)_2$ as a potential target for a polymer coating for three reasons. First, the complex's metal-based oxidation, $\text{Zn}^{2+/3+}$, requires a high potential, making it an interesting alternative to the well-studied redox active ruthenium and osmium analogs.¹²⁻¹³ Second, the large electroinactive window of the polymer is critical for separating electrodes to prevent shorting. Third, the electropolymerization of the zinc *tris*(vbpy) complex is a reduction-based polymerization, achieved by applying a negative potential to inject electrons into the bipyridine rings. This is key for many electrode materials that are prone to electrochemical oxidation.¹⁴

2.3 Experimental

Synthesis of 4-vinyl-4'-methyl-2,2'-bipyridine and $[\text{Zn}(4\text{-vinyl-4}'\text{-methyl-2,2}'\text{-bipyridine})_3](\text{PF}_6)_2$: The synthesis of the ligand and the zinc complex were both taken from literature¹⁵⁻¹⁶. The purity was confirmed with ¹H_NMR before proceeding with electropolymerization experiments.

Nanowire Synthesis: The syntheses of nanowires were adapted from previously reported methods¹⁷⁻²⁰. Porous anodic alumina (AAO) templates were obtained from Whatman (100 nm pores, 13 mm circles) and 3-5 nm of chromium followed by 1-1.5 μm of copper (or gold) was thermally evaporated on one side as a back electrode (Denton Vacuum BTT-IV Evaporator). Electrical contact was made to the evaporated metal by attaching a copper wire with colloidal silver paint (Ted Pella – isopropanol based).

Nanowires were deposited in a three electrode cell, with a SSCE reference electrode, a platinum mesh counter electrode and the AAO working electrode. For copper, the 10 mL reaction solution consisted of 0.627 M CuSO₄ in 18 Ω (Millipore) H₂O and 1 mL of concentrated H₂SO₄. The AAO working electrode was submerged in the reaction solution until the open-circuit potential (E_{oc}) remained constant over 5 minutes. The potential was held at 0.3 V below the E_{oc} for 450 s to yield copper nanowires ~5 μm in length and 100 nm in diameter. The solution was stirred during the deposition (~100 rpm) to replenish reactants to the pores of the AAO template. Platinum nanowires were synthesized in a similar manner, only the 10 mL deposition solution used was a 0.01 M H₂PtCl₆ solution with 1 mL of HClO₄ (70 wt.%). The potential was cycled between +0.463 V and -0.237 V (vs SSCE) at 0.05 V s⁻¹ for 60 cycles to yield platinum nanowires ~3.5 μm long and ~100 nm in diameter. Metallic nanowires were characterized with scanning electron microscopy (SEM), X-ray photoelectron spectroscopy (XPS) and powder X-ray diffraction (XRD).

Nanowire Electrode Fabrication: Once the nanowires were grown, the templates were removed from solution and thoroughly washed with distilled water and ethanol. The conducting back of the AAO electrode was then attached to the conducting side of ITO glass with water-based colloidal graphite (*Aquadag*, Ted Pella) and dried *in vacuo* for 2 hs. Once dried, epoxy (*TorrSeal*), chemically inert in CH₃CN solutions, was used to cover both the AAO template and the ITO conducting glass so that only ~1 cm² area of the template was exposed. The epoxy was then left to dry in open air for 24 hrs, after which the electrode was immersed in aqueous 1 M NaOH at 50 °C for 1 h to release the nanowires. Copper and platinum nanowire array (NWA) electrodes were both

synthesized in this manner. Figure 2.1 is a process schematic of the NWA electrode fabrication.

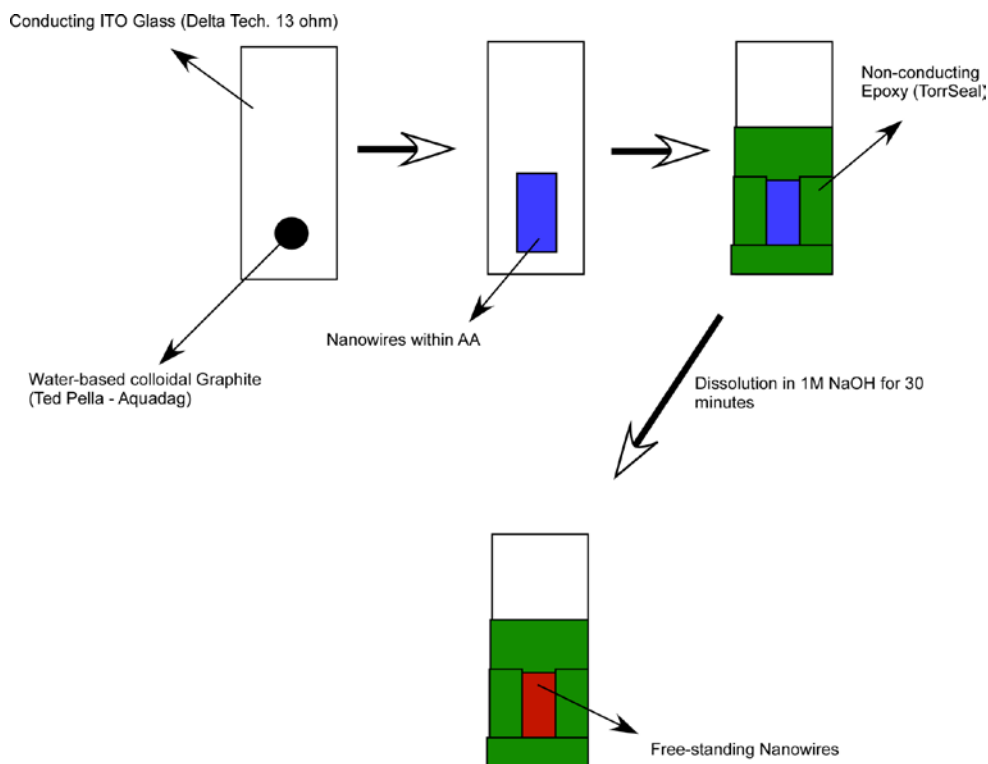


Figure 2.1. Schematic depicting the construction of nanowire electrodes used for polymer modification. The 2-dimensional surface area of the free-standing nanowires was kept to $\sim 1 \text{ cm}^2$.

Electropolymerization of $[\text{Zn}(4\text{-vinyl-4'methyl-2,2'-bipyridine})_3](\text{PF}_6)_2$:

Electropolymerization was achieved by utilizing a three-electrode Van Duyne cell where all oxygen was evacuated by bubbling acetonitrile-saturated nitrogen through the 0.1 M TBAPF₆/CH₃CN before polymerization. In all cases, a platinum wire was used as a counter electrode and the reference electrode was a saturated sodium calomel electrode (SSCE). Additionally nitrogen was blown over the cell during the electrochemical experiments to minimize oxygen contamination. Oxygen evacuation was confirmed by

taking a background cyclic voltammogram between 0 V and -1.2 V vs SSCE. All electrochemical and solid-state electrical measurements were done on a CH Instruments 650 potentiostat/galvanostat.

Physical characterization of polymer thin-films, nanowires and polymer-modified nanowires: Scanning electron microscopy (SEM) (JOEL JSM 6500F) was utilized to characterize the nanowires, before and after polymer deposition. The accelerating voltage of the electron beam was lowered to 3 keV during imaging of polymer films due to excessive charging of the non-conducting polymer.

X-ray photoelectron spectroscopy (XPS) (Phi 6500) was used to characterize the surface of the different electrodes. Measurements were performed with a 5800 series Multi-Technique ESCA system and analyzed using Multipak software. An Al monochromatic source operating at 350.0 W was scanned at a pass energy of 58.7 eV in intervals of 0.125 eV step⁻¹ over the range indicated on the spectra. High resolution XPS was performed using a signal to noise ratio of at least 100:1 for the films and 50:1 for the nanowires.

The thickness and topography of the polymer films were analyzed using atomic force microscopy (AFM) (Alpha NSOM with contact mode capabilities) of the as deposited films on 0.1 cm²-patterned tin-doped indium oxide (PITO) substrates. Established photolithographic methods were used to accurately etch the surface of the conducting glass electrode.²¹ Analysis of the topography was achieved on an 100 μm x 100 μm area, and the height was determined using the scratch method: A clean razor was used to scratch through the polymer film to the PITO substrate and a depth profile of the scratch was taken from two scratches on three separate electrodes to yield the mean thickness and

error. This method has been used before successfully to determine film height on a two-dimensional surface.⁶

Solid-State Linear Sweep Voltammetry: Electrical measurements done on nanometer thick layers were adapted from methods found in the literature.^{6,22} A Ga-In liquid metal eutectic (Sigma-Aldrich, used as received) was used to make contact to the bare and polymer covered PITO. Tungsten wire, pre-wetted by immersion into the Ga-In eutectic for 30 s, was then used to contact the liquid metal on the surface of the electrode. All solid-state electrical measurements were done in an N₂-filled glove-box and the bare ITO was positively biased.

“Redox-probe” experiments: The complexes [Ru(2,2',2'')-terpyridine)₂](PF₆)₂, [Co(cyclopentadienyl)₂](PF₆) (Elliott Group – CSU) and [Fe(cyclopentadienyl)₂] (Aldrich, used as received) were used to make a 10 mM solution in 0.1 M TBAPF₆/CH₃CN. The three electrode cell was comprised of a platinum mesh counter electrode, Ag/AgCl reference, and the stated working electrode. Cyclic voltammograms were scanned at 0.05 V s⁻¹.

2.4 Results and Discussion

The synthesis of the ligand, 4-vinyl-4'-methyl-2,2'-bipyridine (vbpy), has been reported¹⁵, as well as the synthesis of the zinc *tris*(vbpy) complex salt.¹⁶ A typical potentiodynamic polymerization is shown in (Figure 2.2). As seen in the literature²³⁻²⁵, the current response increases as more polymer is deposited with each cycle. The current-growth reflects the increase in the electroactive surface area of the electrode as the polymer is deposited. We observe that Zn_(m) plating onto the working electrode

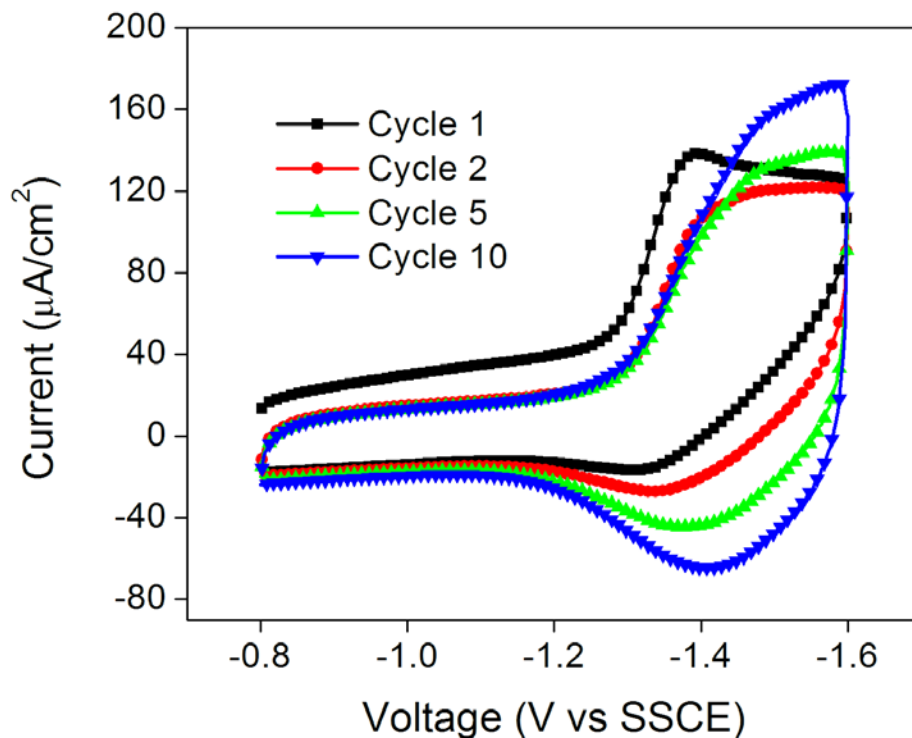


Figure 2.2. Cyclic voltammogram (CV) of the potentiocycling polymerization of 1mM [Zn(4-methyl-4'-vinyl-2,2'-bipyridine)₃](PF₆)₂ onto a 0.1 cm² platinum button electrode at 0.2 V s⁻¹ in 0.1 M TBAPF₆/CH₃CN (Ref: SSCE and Aux: Pt wire). The increased current with cycle number is typical of polymer growth onto an electrode.

occurs when potentials more negative than ~ -1.70 V vs SSCE are applied.

The electrodeposition of Zn_(m) and the broad peak associated with the polymer film renders electrochemical determination of polymer thickness unreliable. We used atomic force microscopy (AFM) to establish the thickness of the polymer films as a function of cycle number. AFM experiments were conducted in contact mode. Thickness was measured across scratches made in the polymer film with a razor blade. With a monomer concentration of 1 mM, and an electrode (PITO) surface area of 0.1 cm², we show that the thickness of the polymer film varied linearly with cycle number up to twenty cycles

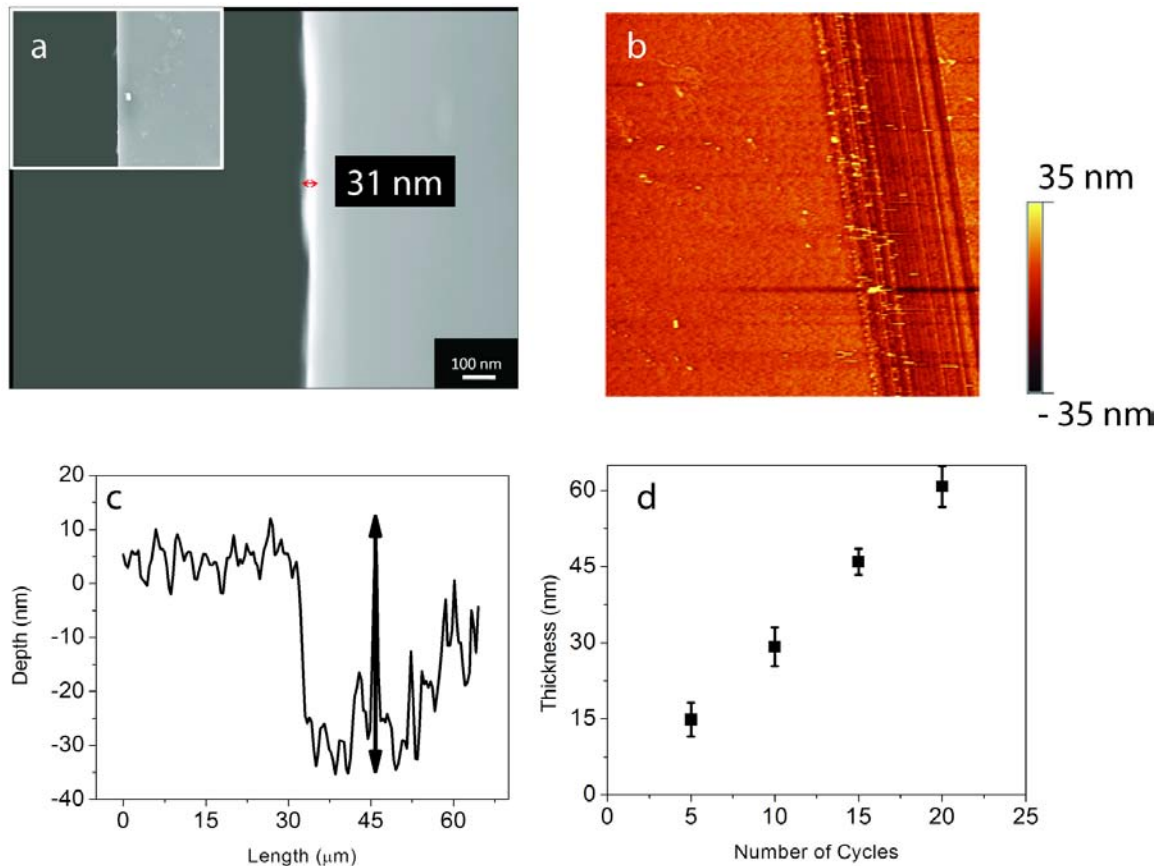


Figure 2.3. a) SEM image of the polymer layer on an ITO surface. b) Top-down AFM image of the topography of a scratched thin polymer layer on an etched ITO surface (100 μm x 100 μm). The height of the polymer is measured by taking a c) line profile perpendicular to the scratch. For potentiocycling depositions, the experiment depicted a d) linear relationship between cycle number and polymer height. Error bars were obtained from 1 sigma analysis of two scratches on three separate samples.

(Figure 2.3). Scanning electron microscopy was used to confirm these measurements by imaging a cross section of a polymer coated ITO surface (Figure 2.3a). This correlation is not rigorous on nanowires due to the inherent differences in diffusion profiles when depositing on nanowires versus a planar electrode, however it is a useful guide for estimating the number of cycle numbers required to achieve an approximate thickness.

We tested polymer coatings deposited on both films and nanowires arrays. Metal substrates were made by thermal evaporation. Nanowire arrays were synthesized by

electrodeposition of copper into porous anodic aluminum oxide (AAO). A thick layer of gold or copper was evaporated onto one side of the AAO templates. A copper wire was then attached with silver paint. The entire metal surface on the back of the AAO was painted with water insoluble, electrically insulating nail polish. Copper wires were then deposited in the AAO pores, and the alumina template was selectively dissolved away resulting in free-standing wires (Figure 2.4a).^{17,19} Since the nail polish used is soluble in acetonitrile (the solvent used in the electrochemical polymerization), a different electrode was used in preparing the polymer-coated nanowires. These electrodes were constructed (Figure 2.1) by placing the AAO on a strip of conducting ITO glass (Delta Technologies, 13 Ω) and covering the surrounding ITO with a non-conducting epoxy (TorrSeal) which is insoluble in acetonitrile.

The scanning electron microscopy images of the copper wires before and after polymerization are shown in Figure 2.4a and b. The micrographs exhibit a uniform change in morphology for the coated wires versus the as-deposited nanowires. However, imaging techniques are not sensitive to low numbers of defects.

We chose to conduct redox-probe experiments, with similarly synthesized platinum NWA electrodes¹⁹, since this technique should be sensitive to pinholes in the polymer coatings⁸. Figure 2.4c-f shows the redox activity of two species of different sizes and charges. The smaller, neutral ferrocene exhibits electroactivity on the polymer-coated electrodes, albeit significantly attenuated relative to each corresponding bare electrode. Moreover the wave shape is consistent with restricted diffusion ostensibly through the molecular-dimension pores of the polymer. In contrast, the electrochemical activity of the larger, positively charged $[\text{Ru}(2,2',2''\text{-terpyridine})_2]^{2+}$ species appears to be totally

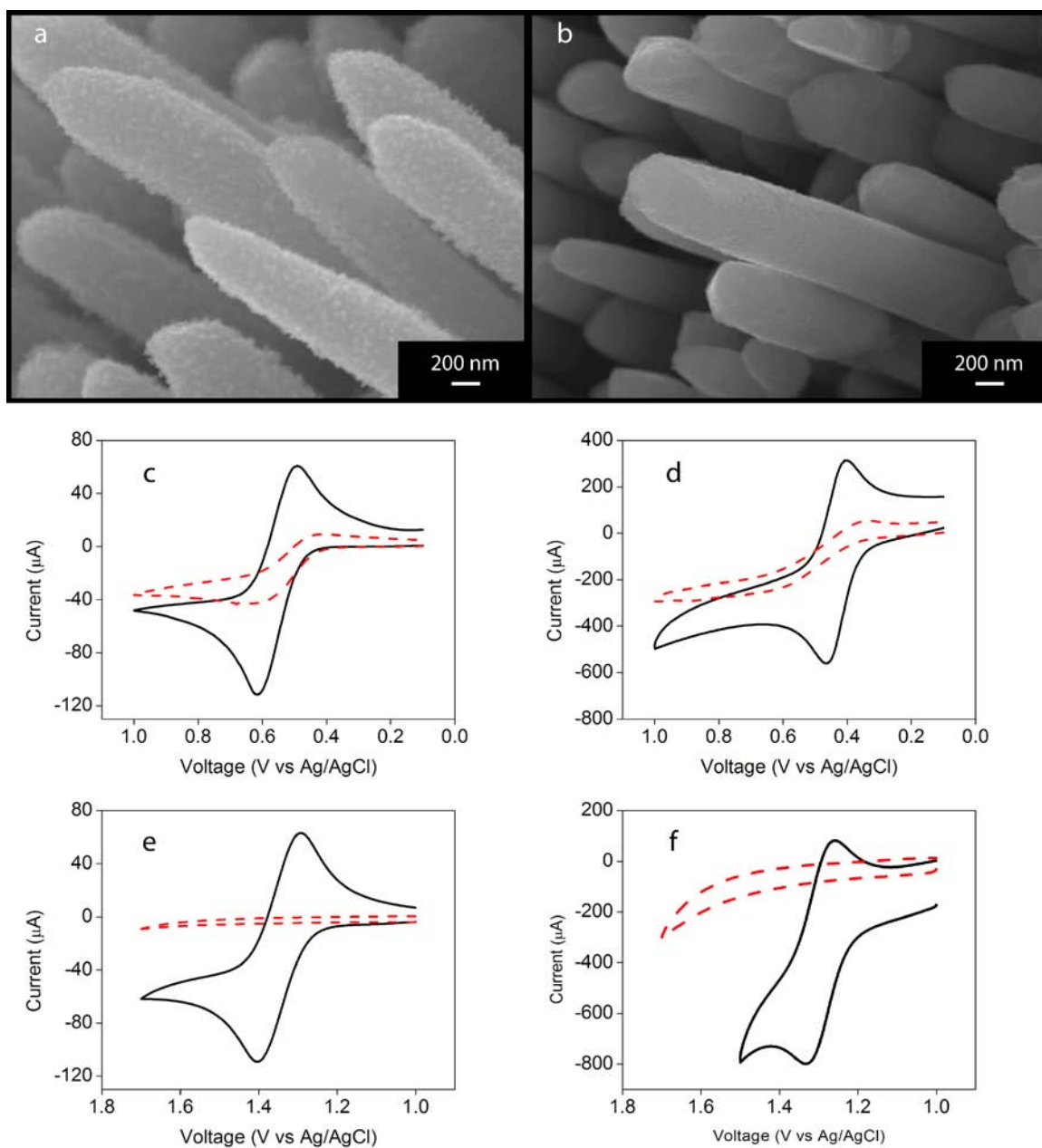


Figure 2.4. SEM pictures of (a) bare and (b) modified copper nanowire electrodes. CVs of a bare (solid) and polymer modified (dashed) platinum electrode in c,d) 10 mM ferrocene and (e,f) 10 mM [Ru(2,2',2''-terpyridine)₃](PF₆)₂ at 0.05 V s⁻¹ in 0.1 M TBAPF₆/CH₃CN (Ref: Ag/AgCl and Aux: Pt mesh). The voltammetric response of both the (c,e) Pt button and (d,f) Pt nanowire electrode depicts that the polymer is capable of uniformly covering the planar and three-dimensional nanowire architecture.

blocked on both the planar and NWA electrodes coated with polymer.

Additionally, to determine whether the polymer is acting as an ion exclusion layer, the voltammetric response of cobaltocenium was also measured and found to be similar to ferrocene (Figure 2.5). Our electrochemical results, coupled with the SEM micrographs (Figure 2.4a and b), indicate that a conformal layer of *poly*-[Zn(4-vinyl-4'-methyl-2,2'-bipyridine)₃](PF₆)₂ is deposited on the surface of the NWA electrodes. Figure 2.6 displays a micrograph of the entire length of polymer modified copper nanowires, showing that the morphology and contrast is the same along the entire length of the nanowires, indicating complete coverage. The same polymer has also been shown to grow on and adhere well to copper, platinum, gold, and ITO surfaces.

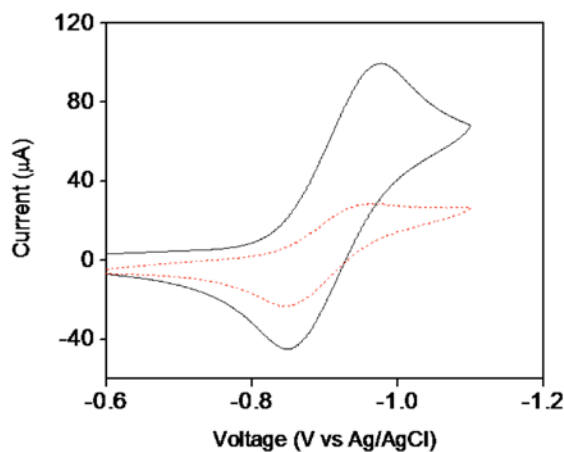


Figure 2.5. Voltammetric response of a bare (solid) and modified (dash) platinum button electrode to 10 mM cobaltocenium ([Co(cyclopentadienyl)₂](PF₆)) at 0.05 V s⁻¹ in 0.1 M TBAPF₆/CH₃CN (Ref: Ag/AgCl and Aux: Pt wire). The diffusion of the charged cation through the polymer layer indicates that the polymer does not act as an ion exclusion layer.

X-ray photoelectron spectroscopy (XPS) was used to further confirm the presence of the polymer coating on both nanowires (Figure 2.7) and films (Figure 2.8). The presence of the Zn 2p 3/2 and F 1s peaks were used as the fingerprints for the presence of the

polymer, and representative peaks for each metal were probed on bare electrodes for comparison. Clear metal peaks are observed before coating, and a complete lack of the metal peaks were observed for polymer coated nanowires and films.

Finally, a series of polymer-modified PITO electrodes were tested to examine the breakdown voltage as a function of polymer thickness (Figure 2.9). A ~30 nm polymer layer electrodeposited on PITO showed no appreciable current flow up to its breakdown

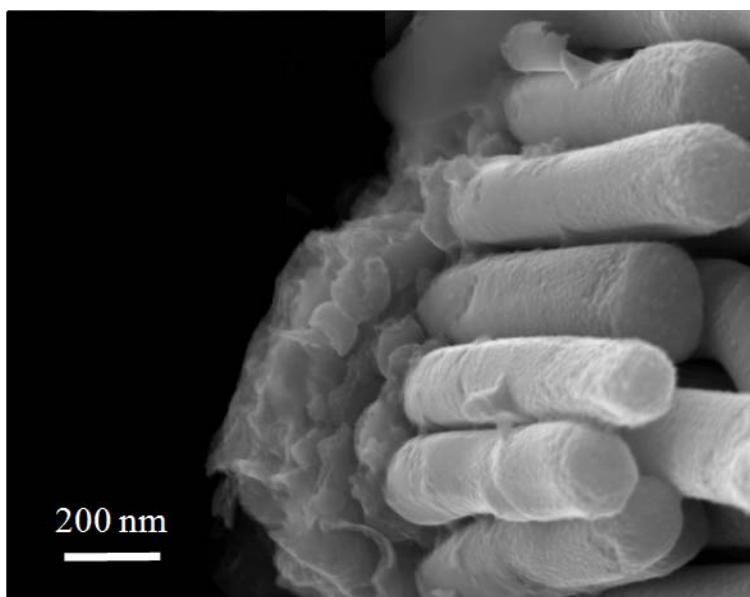


Figure 2.6. SEM micrograph depicting the entire length of copper nanowires covered with the electrodeposited polymer

bias of $\sim + 3.5$ V, which indicates that a thin polymer layer is electrically resistive over a large voltage window. These polymer films would serve as good dielectric coatings as polymerized. The possibility of replacing the Zn with other divalent metals, as well as exchanging the anions, opens the door to a range of versatile polymer films.

Murray *et al.* have illustrated²⁶ the capability of *poly*-[Zn(4-vinyl-4'-methyl-2,2'-bipyridine)₃](PF₆)₂ to exchange Zn²⁺ with Fe²⁺ or Co²⁺. The chemical doping procedure

involved soaking the films in a FeCl_2 solution to obtain $\sim 40\%$ iron doping, or electrochemically cycling the zinc polymer through the $\text{Fe}^{2+}/\text{Fe}^{3+}$ potentials to achieve

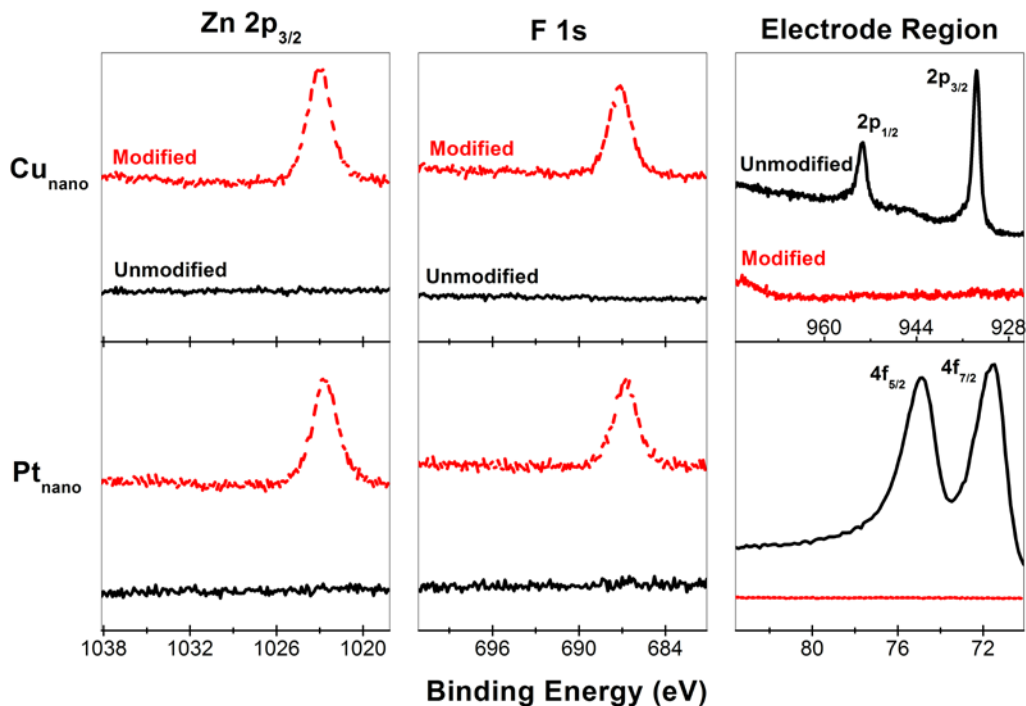


Figure 2.7. XPS high resolution spectra of bare (red, dashed) and polymer-modified (black, solid) nanowire electrodes. All the spectra were cycled until the peak to noise ratio (where applicable) reached at least 50:1.

> 95% conversion. The transparent zinc polymer was used as optical diluents for the colored iron and cobalt films. However, the solid-state electronics of the homopolymeric, or mixed-polymeric films, have not been studied. Materials with strong dielectric capabilities, especially those which can be applied conformally to conducting surfaces, are of particular interest to researchers in the field of microelectronics.²⁷⁻²⁸

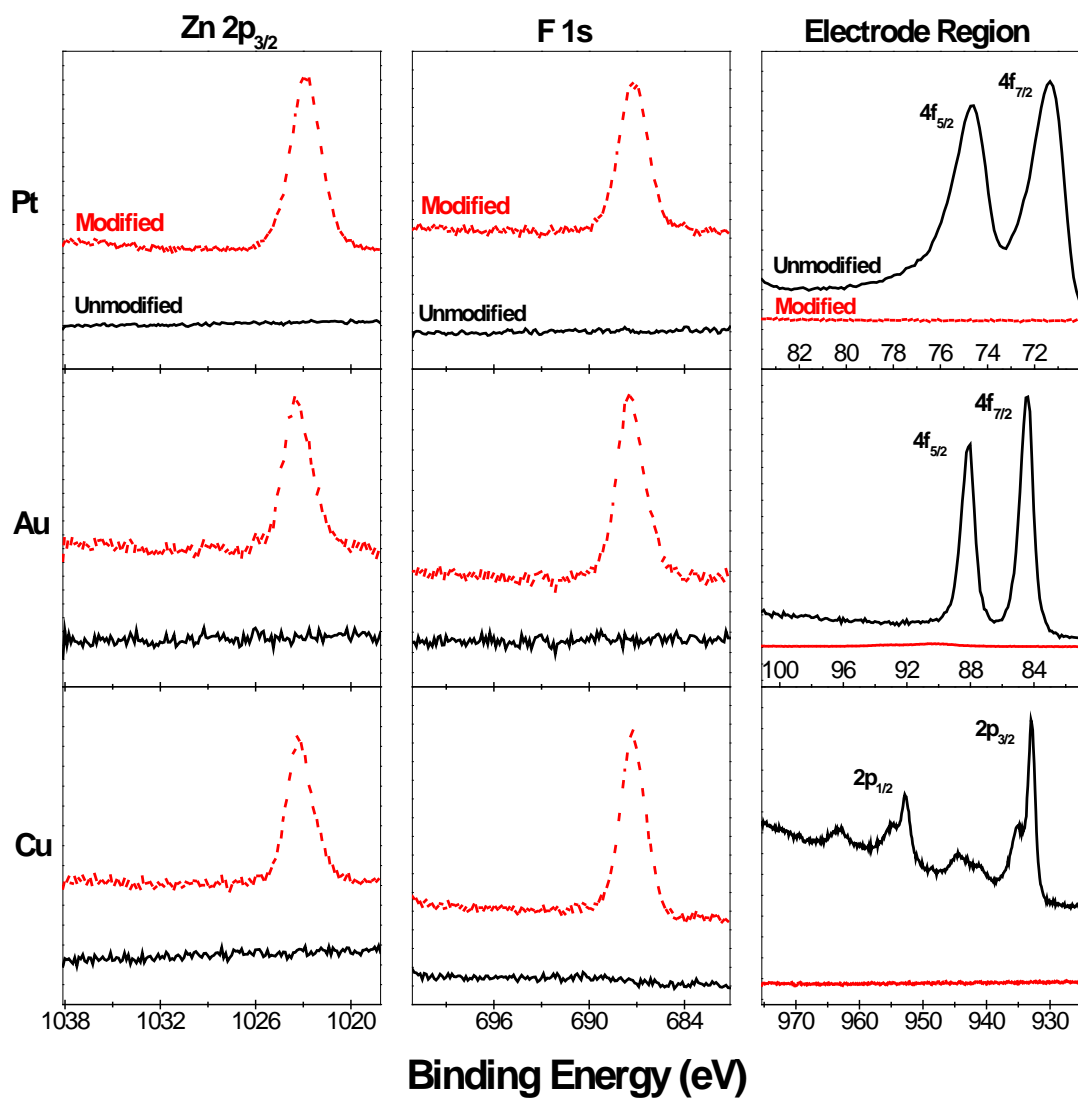


Figure 2.8. XPS high resolution spectra of bare (red, dashed) and polymer-modified (black, solid) planar electrodes. All the spectra were cycled until the peak to noise ratio (where applicable) reached at least 100:1.

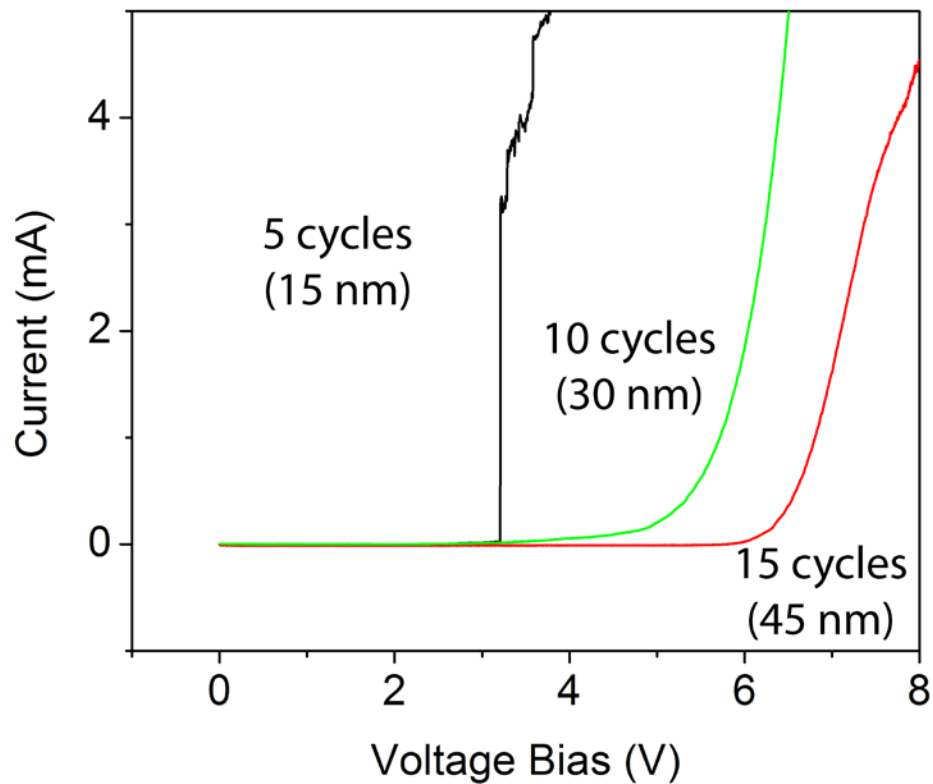


Figure 2.9. Solid-state linear sweep voltammograms *poly*-[Zn(4-methyl-4'-vinyl-2,2'-bipyridine)₃](PF₆)₂ of various thicknesses.

2.5 Conclusion

Controlling the dielectric window of polymeric insulators in nanoscale dimensions is an important step in the fabrication of solid-state nanodevices, such as nanobatteries, nanocapacitors and nanotransistors. The electrical limits of *poly*-[Zn(vbpy)₃](PF₆)₂ is directly coupled to the physical characteristics of thickness and uniformity. For Li-ion battery applications, transforming the dielectric into a solid-state Li-ion conductor is necessary for the system to provide energy. However, batteries based on a Zn_(m) anode is a natural avenue because Zn²⁺ ions are present within the as-polymerized film.

We have shown that *poly*-[Zn(4-vinyl-4'methyl-2,2'-bipyridine)₃](PF₆)₂ can be conformally coated onto films and high-aspect ratio nanowire arrays. The coverage of the

polymer has been examined through imaging, electrochemical, and spectroscopic experiments. Future work will focus on further linear sweep voltammetry experiments, impedance spectroscopy and salt-doping studies with the ultimate goal of exploring the range of properties possible for this versatile polymer coating.

2.6 References

- (1) Tarascon, J. M.; Armand, M. *Nature* **2001**, *414*, 359.
- (2) Li, N. C.; Martin, C. R. *Journal of the Electrochemical Society* **2001**, *148*, A164.
- (3) Lux, K. W.; Rodriguez, K. J. *Nano Letters* **2006**, *6*, 288.
- (4) Vullum, F.; Teeters, D. *Journal of Power Sources* **2005**, *146*, 804.
- (5) He, X. M.; Shi, Q.; Zhou, X.; Wan, C. R.; Jiang, C. Y. *Electrochimica Acta* **2005**, *51*, 1069.
- (6) Rhodes, C. P.; Long, J. W.; Doescher, M. S.; Fontanella, J. J.; Rolison, D. R. *Journal of Physical Chemistry B* **2004**, *108*, 13079.
- (7) Rhodes, C. P.; Long, J. W.; Rolison, D. R. *Electrochemical and Solid State Letters* **2005**, *8*, A579.
- (8) Long, J. W.; Dunn, B.; Rolison, D. R.; White, H. S. *Chemical Reviews* **2004**, *104*, 4463.
- (9) Kiefer, R.; Chu, S. Y.; Kilmartin, P. A.; Bowmaker, G. A.; Cooney, R. P.; Travas-Sejdic, J. *Electrochimica Acta* **2007**, *52*, 2386.
- (10) Talbi, H.; Just, P. E.; Dao, L. H. *Journal of Applied Electrochemistry* **2003**, *33*, 465.
- (11) Beer, P. D.; Kocian, O.; Mortimer, R. J.; Ridgway, C. *Journal of the Chemical Society-Dalton Transactions* **1993**, 2629.
- (12) Bommarito, S. L.; Lowerybretz, S. P.; Abruna, H. D. *Inorganic Chemistry* **1992**, *31*, 502.
- (13) Bommarito, S. L.; Lowerybretz, S. P.; Abruna, H. D. *Inorganic Chemistry* **1992**, *31*, 495.
- (14) Thackeray, M. M.; Vaughey, J. T.; Johnson, C. S.; Kropf, A. J.; Benedek, R.; Fransson, L. M. L.; Edstrom, K. *Journal of Power Sources* **2003**, *113*, 124.
- (15) Abruna, H. D.; Breikss, A. I.; Collum, D. B. *Inorganic Chemistry* **1985**, *24*, 987.
- (16) Meyer, T. J.; Sullivan, B. P.; Caspar, J. V. *Inorganic Chemistry* **1987**, *26*, 4145.
- (17) Gelves, G. A.; Murakami, Z. T. M.; Krantz, M. J.; Haber, J. A. *Journal of Materials Chemistry* **2006**, *16*, 3075.
- (18) Green, S.; Cortes, A.; Rivero, G.; Gomez, H.; Dalchiale, E. A.; Marotti, R. E. In *Physica Status Solidi C - Current Topics in Solid State Physics, Vol 4, No 2*; Stutzmann, M., Ed. 2007; Vol. 4, p 340.
- (19) Piao, Y.; Lim, H.; Chang, J. Y.; Lee, W. Y.; Kim, H. *Electrochimica Acta* **2005**, *50*, 2997.
- (20) Wu, B.; Boland, J. J. *Journal of Colloid and Interface Science* **2006**, *303*, 611.
- (21) Scott, M. *Ph. D Dissertation* **2007**.
- (22) Rampi, M. A.; Whitesides, G. M. *Abstracts of Papers of the American Chemical Society* **1998**, *216*, 166.
- (23) Denisevich, P.; Abruna, H. D.; Leidner, C. R.; Meyer, T. J.; Murray, R. W. *Inorganic Chemistry* **1982**, *21*, 2153.
- (24) Elliott, C. M.; Baldy, C. J.; Nuwaysir, L. M.; Wilkins, C. L. *Inorganic Chemistry* **1990**, *29*, 389.
- (25) Gould, S.; Strouse, G. F.; Meyer, T. J.; Sullivan, B. P. *Inorganic Chemistry* **1991**, *30*, 2942.
- (26) SurrIDGE, N. A.; Keene, F. R.; White, B. A.; Facci, J. S.; Silver, M.; Murray, R. W. *Inorganic Chemistry* **1990**, *29*, 4950.
- (27) White, R. J.; White, H. S. *Langmuir* **2008**, *24*, 2850.
- (28) Bruce, P. G.; Scrosati, B.; Tarascon, J. M. *Angewandte Chemie-International Edition* **2008**, *47*, 2930.

Chapter 3

Reductive electropolymerization of acrylate monomers for Li-ion batteries

3.1 Introduction

The techniques mastered and lessons learnt from *poly*-[Zn(vbpy)₃](PF₆)₂ are important for the development of a new polymer electrolyte. Impregnating the solid electrolyte with Li-ions after polymerization is difficult to achieve. The chemical and electrochemical ion exchange between Zn²⁺ and Li⁺ is not as facile as the exchange of Zn²⁺ with Fe²⁺^[1]. However, introducing mobile Li-ions can be accomplished with two other methods (Chapter 1.3), salt soaking and co-polymerization. Since the initial discovery by Wright *et al.*², extensive research in ion dissolution into *poly*(ethylene oxide) (PEO) has set the standard for solid-polymer electrolytes (SPEs)³⁻⁹. Despite the wide variety of polymer hosts tested, such as *polyimides*, *polysulfones* and *polypyridals*, the best conductivity results for SPEs still rely on variations of the PEO structure¹⁰. The amorphous ether-based polymer can be solvated with high concentrations of lithium salts (8 : 1 atomic oxygen : lithium). These qualities may be less important for nanoscale polymer films, as stated in Chapter 1.2. However, finding a reductively polymerizable monomer is the first-step.

Research for systematic cathodic electropolymerization¹¹⁻¹³ can be traced back to work done in the late 1960s into early 1970s, however, with limited success in adhesion, coverage and chemical stability. More recently (1992 – present)¹⁴⁻²⁸, multiple groups have pioneered work in the electrografting of vinylic monomers onto metallic surfaces. Electrografting, a subset of electropolymerization, consists of a M-C bond formed between electrode and monomer. Typically, adhesion between electro-initiated polymers and the substrate is due to “sticky” Van der Waal’s forces. Researchers have conducted multiple experiments^{15,22,25,29} as evidence of M-C bond formation, such as, infra-red

spectroscopy, X-ray photoelectron spectroscopy, near-edge X-ray absorption fine structure, and quartz-crystal microbalance measurements.

The formation of a covalent M-C bond is one product of two competing mechanisms during the polymerization process. Figure 3.1 displays Deniau and coworkers²⁹⁻³⁰ two proposed mechanisms for the cathodic grafting of polymers. Both processes begin by applying a reducing potential to the electrode which creates a negatively charged surface.

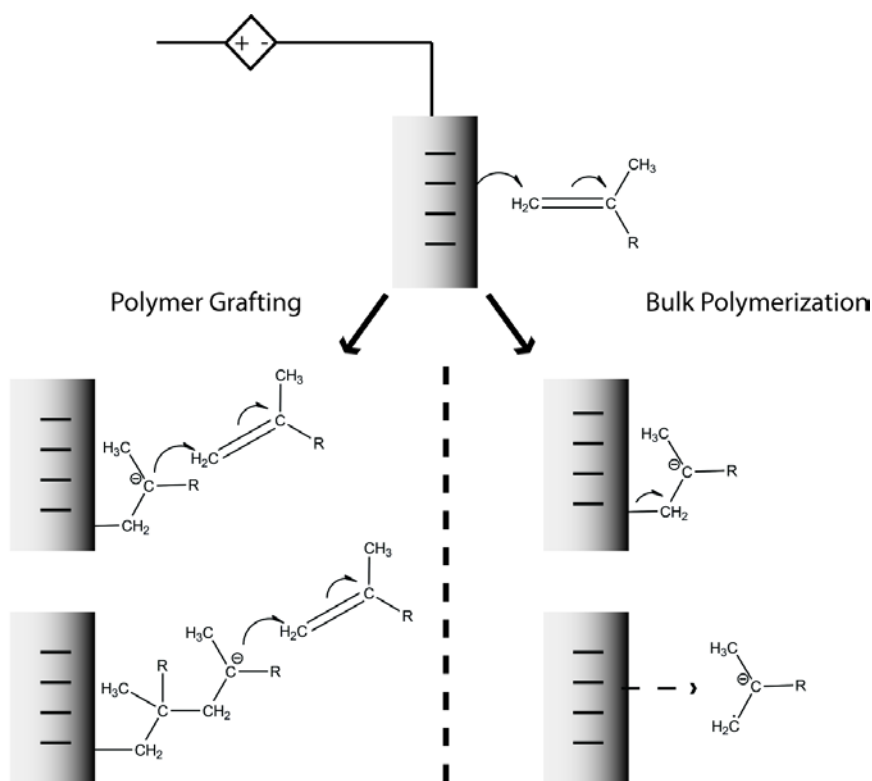


Figure 3.1. The competing mechanisms during the cathodic electropolymerization of methacrylate monomers, adapted from Ref²⁹. Electrografting is initiated if the propagation of the polymer can occur (left) before the repulsion of the carboanion (right).

When the monomer diffuses to the surface, heterogeneous electron transfer into the vinyl group creates a M-C bond and a carboanion. The difference between polymer grafting (Figure 3.1-left) and bulk polymerization (right) is the chemisorption lifetime (τ) of the electrode-bonded carboanion. If $\tau > (k_p C_m)^{-1}$ (where k_p is the rate constant of

polymerization and C_m is the monomer concentration), then polymer grafting process takes place. If $\tau < (k_p C_m)^{-1}$, then desorption of the carboanion, radical-radical coupling of two desorbed anions, and bulk polymerization occur sequentially. In both cases, τ is small due to the coulombic repulsion between the carboanion and the negatively polarized electrode. If k_p is constant for both processes, then grafting is induced by increasing the concentration of monomer, ($C_m = 2 - 5 \text{ M}$). A combination of both mechanisms is possible; that is, the desorbed polymer can be trapped within the chains of the chemisorbed layer. Since grafting of a polymer is not necessary to the 3D architecture, we did not conduct experiments to affirm M-C bond formation.

The electrografting of several vinylic monomers, has been reported since Deniau *et al.*'s initial work with acrylonitrile on metal surfaces. Sensing, decomposition-protection and selective grafting are all cited^{27,29-30} as motivation for the research. In those reports, the electrografting of GMA (Figure 3.2) caught our attention as a potential solid polymer electrolyte. The work presented here is the testing, control, and integration of electro-synthesized polymers as solid electrolytes in a 3D nanowire lithium-ion battery.

The successful electropolymerization on Au surfaces is the first reason that enticed us to choose the GMA as our neutral (contains no ionic charge) monomer. Though *polyglycidal methacrylate* (*pGMA*) formation has been reported²⁸ on Au surfaces only, the successful polymerization of *pZn(vbpy)₃* onto different surfaces encouraged us to extend the research to encompass a range of conducting electrodes. Second, GMA's structure also includes an ether linkage which is important for lithium-salt dissolution and Li-ion transport (Chapter 1.3). Finally, the epoxide moiety on the tail of the monomer can also be subjected to chemical modification after polymerization, a possible route for

transforming *p*GMA from a dielectric to an electrolyte (Chapter 1.3). Therefore, *p*GMA is amenable to all of the proposed methods for inducing Li-ion conductivity: salt-dissolution, chemical modification and co-polymerization.

Achieving ionic conductivity through copolymerization requires the intelligent selection of both monomers. There are two reasons to choose an anionic (contains a negatively charged group on the polymerizable portion of the molecule) monomer. Primarily, the difficulty experienced during $\text{Li}^+/\text{Zn}^{2+}$ exchange convinced us that Li-ion inclusion into polymers with a cationic backbone is electrostatically unfavorable.

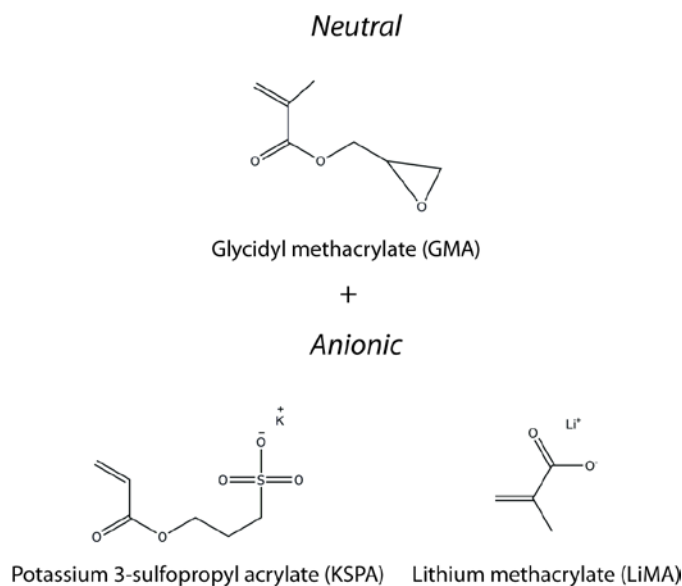


Figure 3.2. Structure of the neutral monomer GMA (top) and the anionic monomers KSPA and LiMA (bottom).

KSPA (Figure 3.2), in contrast, is polymerized through the vinyl group on the anion of the ionic monomer. Therefore, the negatively charged back-bone of the polymer remains intact while cations are exchanged³¹⁻³³. Polymer electrolytes for Li-ion batteries require that the vast majority of ion flow be due to Li^+ movement³⁴⁻³⁵, or $t_{\text{Li}}^+ \approx 1$. The

immobilization of the anion, achieved through co-polymerization, implies that the values obtained for σ_{ion} are only from the transportation of Li-ions. The ethereal oxygens found in the [SPA]⁻ also contribute to cation movement. The choice of anionic monomer is also subject to the following constraints: 1) the monomer must be very soluble (2-5 M) in the electrochemical solvent of choice (DMF if GMA is the neutral monomer) and 2) the monomer must be electrochemically polymerizable in a pre-determined voltage range.

KSPA is not soluble in DMF. Attempts to synthesize and electropolymerize tetramethylammonium 3-sulfopropyl acrylate (TMA SPA) are ongoing. However, KSPA is very soluble in water, and the results for aqueous electropolymerization of KSPA are insightful (Chapter 3.3). In 2009, Ryu *et al.*³⁶ reported on the synthesis and chemical polymerization of lithium methacrylate (LiMA). The monomer is very soluble in DMF, and copolymerization with GMA was achieved and evidenced (Chapter 3.4). As we will discover, the rational choice of monomer does not necessarily guarantee a functional polymer electrolyte. The field of electropolymerization, specifically for the fabrication of electronic, nanostructured devices, is very novel. The reductive electropolymerization onto Cu₂Sb is entirely novel, but the success of the research is vital to achieving the 3D nanowire architecture.

3.2 Experimental

Chemicals: Dimethyl formamide (DMF – Sigma Aldrich 99.8 % anhydrous) was distilled over Na_(m) for 24 h before use. Acetonitrile (Sigma Aldrich – 99.99 % Optima grade), tetrabutyl ammonium perchlorate (TBAClO₄ – Fluka ≥ 99.0 %), and potassium 3-sulfopropyl acrylate (KSPA – Sigma Aldrich) were used as received. Glycidyl methacrylate (GMA – Sigma Aldrich 99.0 %) was bubbled with N₂ and kept at 0 °C in a N₂-filled glove box. Lithium methacrylate (LiMA) was synthesized from literature methods³⁶ and provided by Dan Bates (Prieto/Elliott Group).

Physical characterization - X-ray photoelectron spectroscopy (XPS) (Phi 6500) was used to characterize the surface of the polymer-modified electrodes. Measurements were performed with a 5800 series Multi-Technique ESCA system and analyzed using Multipak software. An Al monochromatic source operating at 350.0 W was scanned with a pass energy of 58.7 eV in intervals of 0.125 eV step⁻¹ over the range indicated on the spectra. All XPS spectra were shifted so that the adventitious C1s peak was located at 284.7 eV. $\chi^2 \leq 1$ for all fitted peaks. Peak positions and atomic ratios are reported from peak-fitting of the data. Scanning electron microscopy (SEM) micrographs were taken using a JEOL JSM 6500F. Atomic-force microscopy (AFM) images were taken with a Nanosurf *EZscan* AFM in contact mode. Analysis was done on the *EZscan 2.0* software package. UV-Vis measurements were taken with an Agilent 8453 spectrometer. ATR-IR spectra were taken with a Thermo Nicolet 380 FTIR spectrometer.

Planar Au and Cu electrode construction: Microscope slides (Ted Pella) were cleaned in 10 vol.% HNO₃ for 1 h, then sonicated in DD H₂O and isopropanol, and dried under N₂. Kapton tape (Ted Pella) was used to mask off a 1 cm² square in the pattern displayed in Figure 3.3a, followed by thermal evaporation of 3-5 nm of chromium then 1-1.5 μm of copper or gold (Denton Vacuum BTT-IV Evaporator).

Freeze-fracture of planar electrodes: The back of the planar metal electrodes were scored as shown in Figure 3.3b. The electrodes were then submerged in liquid-N₂ for 1 min, removed and snapped along the score. Polymer thickness was determined through SEM imaging of the electrode profile.

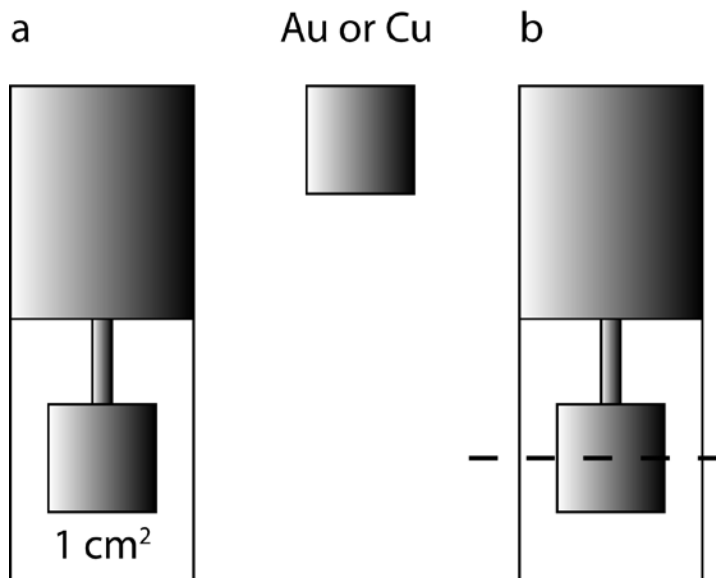


Figure 3.3 a) Planar geometry for Au, Cu and Pt electrodes. b) The location where planar electrodes were scored for freeze-fracture breaking.

Planar Pt and Pt NWA electrode deposition: Pt NWA electrodes were made with previous methods (Chapter 2.3). Evaporated Au electrodes were used as working electrodes in the electrochemical growth of Pt metal. The solution was a 10 mL deposition 0.01 M H_2PtCl_6 solution with 1 mL of HClO_4 (70 wt.%). The potential was cycled between +0.463 V and -0.237 V (vs SSCE) at 0.05 V/s for 20 cycles.

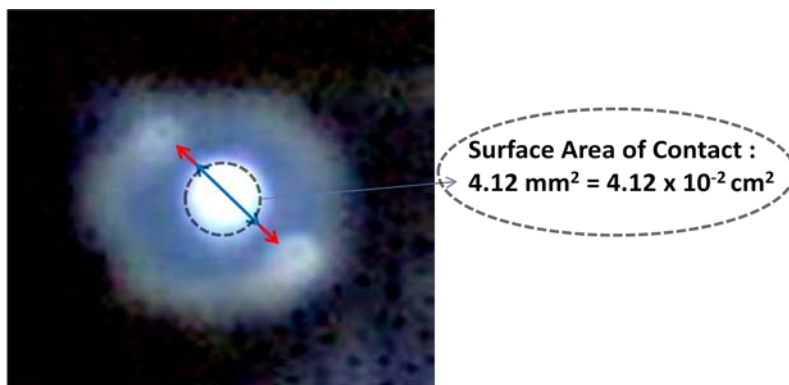
Patterned ITO, Si and Cu_2Sb electrodes: Patterned-ITO electrodes were fabricated with previous methods (Chapter 2.3). *n*-type silicon electrodes were cut into 1 cm x 1 cm squares and the rough side covered with epoxy (*TorrSeal*). The electrodes were then dipped in 1 M HF for 10 seconds, rinsed with isopropanol and dried under N_2 . Copper antinomite electrodes were deposited from aqueous solutions at a single potential³⁷. Electrodes were provided by Jake Kershman (Prieto Group). The deposition was on Cu-foil, therefore, freeze-fracture techniques did not make a clean electrode break. Polymer thickness measurements on Cu_2Sb or Si were not taken.

Electropolymerization: GMA and comonomer depositions were performed in a three-electrode cell in a N_2 -filled glovebox. The counter electrode was a Pt-mesh and the reference was a Ag/AgCl (sat. LiCl / DMF) electrode. The supporting electrolyte is 0.05 M TBAClO₄. *p*KSPA was polymerized out of aqueous solutions in a Van Duyne cell (Chapter 2.3). All electropolymerization were performed with a CHI-660C potentiostat/galvanostat.

“Redox-probe” experiments: The complexes $[\text{Ru}(2,2',2'')\text{-terpyridine}]_2(\text{PF}_6)_2$ (Elliott Group – CSU), $[\text{Co}(\text{cyclopentadienyl})_2](\text{PF}_6)$ (Elliott Group – CSU), and $[\text{Fe}(\text{cyclopentadienyl})_2]$ (Aldrich, used as received) were used to make a 10 mM solution in 0.1 M TBAClO₄ \ CH_3CN . The three electrode cell was comprised of a platinum mesh

counter electrode, Ag/AgCl reference, and the stated working electrode. Cyclic voltamograms were taken at 0.05 V/s.

Solid-state impedance measurements: Making contact to a thin-organic layer is a challenging task. Following past successful procedures (Chapter 2.3), contact to a thin polymer layer was made with a liquid-metal eutectic (Ga-In - Sigma Aldrich). However, the surface area of contact was constrained within a glass capillary. The procedure was adapted from Whitesides *et al.*³⁸ method for contacting self-assembled monolayers. Figure 3.4 is an optical micrograph illustrating the surface area of liquid metal contacting a glass substrate. For temperature-dependent measurements, the electrode was heated on top of a sand bath with a thermometer. The temperature was controlled with a hot-plate, measurements were not taken until the sand-bath temperature was constant for 30 min.



I.D of glass capillary : 3.39 mm
Diameter of eutectic : 2.29 mm

Figure 3.4. Photograph of a constrained liquid metal within a capillary tube. The contrast was changed to dark to improve the resolution between the Ga-In/ air / capillary parts. Distances were measured through a ratio between measured caliper values and pixel counting.

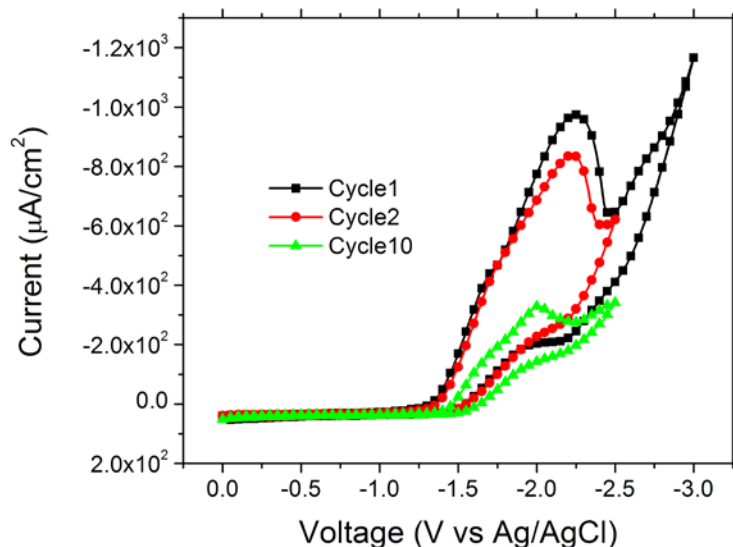


Figure 3.5 Potentiodynamic electropolymerization of 2 M GMA on a planar Au electrode. The supporting electrolyte (SE) is 0.1 M TBAClO₄/DMF and the scan rate is $v = 0.2$ V/s.

3.3 The electropolymerization of GMA

The cyclic voltammograms (CVs) of the potentiodynamic reductive electropolymerization of GMA on a planar Au electrode is presented as Figure 3.5. A decrease in the current of the cathodic peak, $E_{pc} = -2.3$ V (cycle 1), mimics self-limiting behavior. However, 0.31 mA/cm^2 of current still passes ($E_{pc} = -2.0$ V) during the 10th cycle, about 30% of the initial value. The amount of charge passed, the area under the reduction peaks, is not consistent between samples. The values ranged from < 1% to 30% in cycle 10. We hypothesize the inconsistent result is due to the high-concentration of monomer used in the polymerization solution, which is much higher than monomer concentrations in self-limiting polymer growth on surfaces. Self-limiting polymers often

retain no charge by the 2nd or 3rd cycle. As reported in the literature²⁸, the best *p*GMA films were made when the potential is cycled to the E_{pc} .

The concentration of monomer needed, as reported²⁸ for the electrografting of GMA, produces very interesting electrochemical responses. Typically, in self-limiting electropolymerization, the [monomer]:[supporting electrolyte] is 1:50 to negate the effect of migration (Nernst-Planck equations). Also, the effect on the viscosity of the solution with high monomer concentration is unknown. Solution viscosity has a direct correlation to the diffusion of the analytes. Figure 3.6 illustrates that the potentiodynamic response of GMA in smaller, more typical self-limiting concentrations (10 mM) is much different GMA electropolymerization under grafting conditions (2 M).

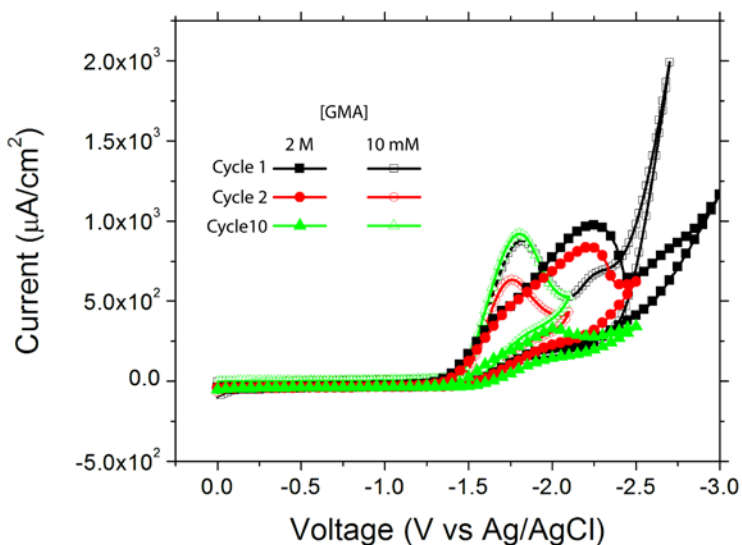


Figure 3.6 Cyclic Voltammograms of 2 M GMA (filled shapes) and 10 mM GMA (empty shapes) on a planar Au electrode. SE: 0.1 M TBAClO₄/DMF and $v = 0.2$ V/s.

The first observation about the cyclic voltammograms is that there is no corresponding oxidation current for the reduction of GMA; thus, the reductions are electrochemically

irreversible. The cathodic peak, $E_{pc} = -1.80$ V (cycle 1), in low concentration solutions is + 0.5 V of the peak in high concentration solutions. The electroreduction of the 10 mM solution displays a single peak comprised of an electron-transfer limited current rise and a diffusion limited tail. At low concentrations, there is no indication the electroreduction of GMA during the first potentiodynamic scan inhibits the reduction of more monomer. The current-density at the gold electrode during cycle 10 is almost exactly the same as cycle 1. XPS analysis shows no polymer present on the surface of the Au electrode (not shown). As the proposed model illustrates (Figure 3.1), the electropolymerization of GMA requires high concentrations to form a polymer film and the polymerization on the surface of the electrode is not self-limiting.

The electropolymerization of GMA on different surfaces is important for three reasons: Cu_2Sb is not amenable to redox-probe experiments, high annealing temperatures and thickness measurements, because of electrochemical oxidation, antimony evaporation and electrode fabrication (experimental) restrictions, respectively. Therefore, experimenting with a host of electrodes would help us avoid experimental hurdles due to the anode material. Figure 3.7 shows the potentiodynamic electropolymerization of a 2 M GMA solution on four different conducting electrodes. The current response with respect to the cycle number is similar between noble metal electrodes, such as Au and Pt, which do not form a surface oxide layer in ambient conditions.

*p*GMA can successfully deposit on a film of Cu_2Sb and Pt nanowire array (NWA) electrodes (Figure 3.7a and b). The decrease in current with increasing cycle number is similar to the response of a planar Au electrode (Figure 3.5). If the same voltage window

is used to deposit on a freshly cleaned *n*-Si electrode, then no polymer is detected (via XPS). When the voltage window extends from -2.3 V to -3.2 V (vs Ag/AgCl), the characteristic drop in current is observed (Figure 3.7c) and *p*GMA successfully deposited on the surface of the electrode (via XPS). Tin-doped indium oxide (ITO) is a very attractive electrode for a variety of reasons. The conducting glass substrate is extremely flat (rms = 17 ± 8 nm) and it is very conducting (5-15 ohms, *Delta Technologies*).

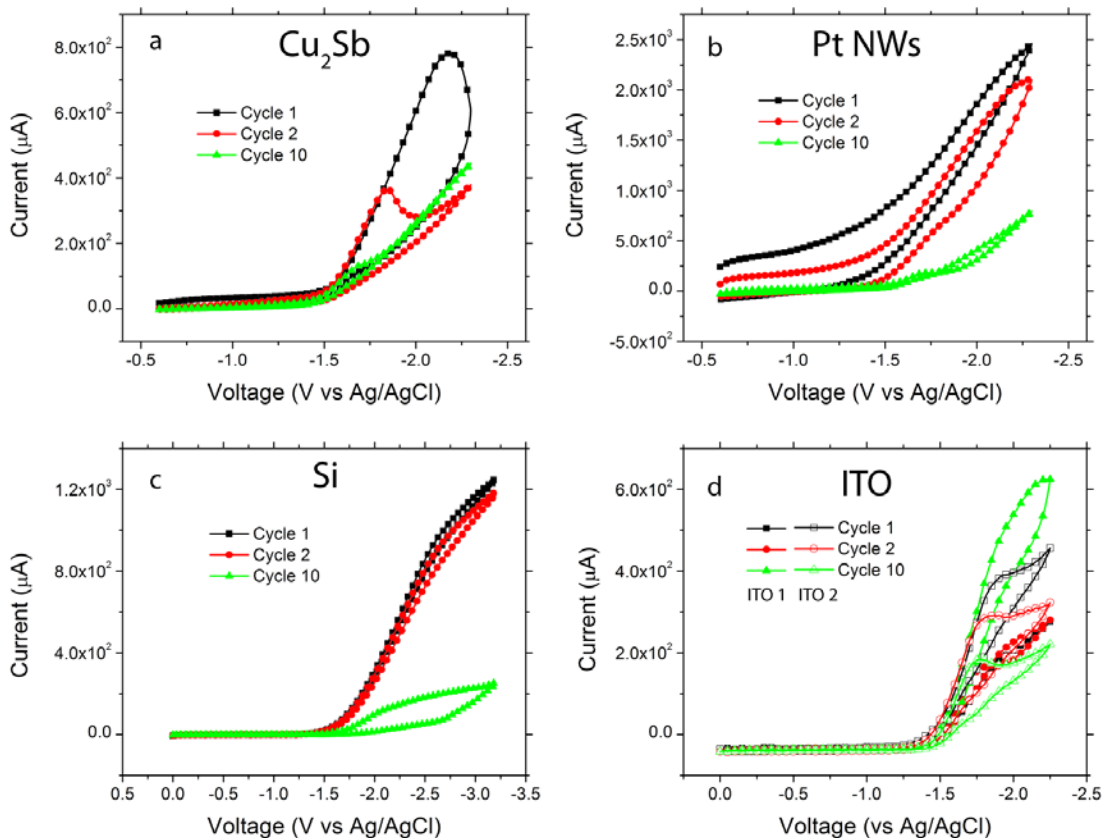


Figure 3.7 Potentiodynamic electropolymerization of 2 M GMA on a) Cu_2Sb , b) Pt nanowires, c) *n*-Si, and d) ITO electrodes. SE: 0.1 M $\text{TBAClO}_4/\text{DMF}$ and $v = 0.2$ V/s.

Additionally, it is transparent, which is useful for spectroscopic measurements, and we have followed established lithographical methods to control the conductive surface area.

However, for the electropolymerization of GMA, using ITO as the working electrode surface produces very inconsistent results. Figure 3.7d shows the potentiodynamic scans of two patterned ITO electrodes (experimental) electropolymerized under the exact same conditions. ITO 1 displays a growing current response, similar to the electropolymerization of conducting polymers. ITO 2 displays a decreasing current response, much like the electropolymerization of GMA on Au or Pt electrodes. There is the appearance of a thick, translucent solid that is displaced from the surface of both ITO electrodes during the polymerization or washing steps. XPS survey scans determined that no *p*GMA adhered to the surface of ITO 1 or ITO 2, but the solid material displaced is indeed *p*GMA. Due to the above inconsistent electrochemical results on ITO, further analysis was not completed. The surface, solution and electrochemical sensitivity of GMA electropolymerization limit the options of electrode material, electrochemical solvents and supporting electrolytes. Under the right conditions, consistent electropolymerization on a surface is possible, including chemically and electrochemically cleaned Cu₂Sb. Once consistent electrochemical results were established, we moved to measure the thickness and conformal coverage of the *p*GMA.

3.4 Physical characterization of *p*GMA

Thickness measurements

The “scratch” method, established in the literature³⁹ and used previously by us, was giving unreliable thickness results. Au and Cu metal were evaporated onto the surface of microscope slides, and the poor choice of glass substrate had unfortunate consequences. The underlying glass has surface roughness (rms ~ 500 ± 200 nm) that makes nanoscale

thickness determined by the scratch method unreliable. However, a freeze-fracture method was established (experimental) utilizing SEM profile images to determine the thickness of the *p*GMA on planar Au, Cu and Pt (from electrodeposition of Pt_(m) on Au) electrodes. Due to electrode fabrication restrictions (experimental), thickness measurements on Cu₂Sb and Si were not established with this method. Figure 3.8 is an SEM micrograph profile image of a doped and annealed *p*GMA:LiClO₄ on Au electrode. Doping procedures are discussed shortly. Table 3.1 is a summary of the SEM thickness measurements on Au, Pt and Cu surfaces.

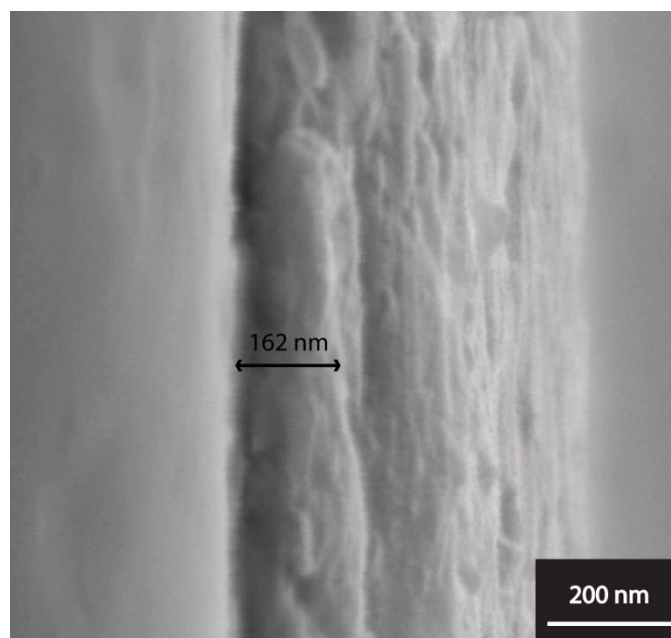


Figure 3.8. SEM profile image of a freeze-fractured Au electrode modified with *p*GMA:LiClO₄. Thickness measurements were made using the JEOL 6400 software.

Table 3.1 Thickness measurements *p*GMA and *p*GMA:LiClO₄.

Electrode surface	<i>p</i> GMA Thickness via SEM (nm)	<i>p</i> GMA:LiClO ₄ Thickness via SEM (nm)
Au	78 ± 12	160 ± 15
Pt	85 ± 13	172 ± 12
Cu	65 ± 19	135 ± 21

The average thickness of *p*GMA on Pt is slightly larger than on Au. The polymer films are thinner on Cu electrodes. The potentiodynamic polymerization method is a suitable method for controlling the thickness of *p*Zn(vbpy)₃, but other methods may produce consistently thinner layers. Optimization of the thickness of *p*GMA will be vital to maximizing the power of the three-dimensional battery, but experiments to this end are not presented in this dissertation.

The electrochemical response *p*GMA growth on electrode surfaces is different, and so are the thickness measurements for the polymers. We have to make measurements directly on Cu₂Sb electrodes to accurately describe *p*GMA formation, thickness and coverage on the anode.

Uniformity of pGMA on planar electrode surfaces

There are several methods to detect the presence of pinholes in a polymer layer. XPS survey scans were taken immediately after drying (no heat) to detect the presence of any macroscopic pinholes in the polymer layer. No substrate peaks were seen for Au, Pt, Cu, or Si planar electrodes. Complete coverage of surfaces is vital due to intercalation of the cathode material by drop-casting small nanoparticles or a sol-gel. We require that the coverage of *p*GMA be on the nanoscopic level.

To check for a conformal coating, a series of redox-probe experiments were performed with 5 mM $\text{Fe}(\mu^5\text{-cyclopentadiene})_2$ and 5 mM $\text{Ru}(\text{terpyridine})_2(\text{PF}_6)_2$. The experiments were done with a planar Pt electrode in a 0.1 M $\text{TBAPF}_6/\text{CH}_3\text{CN}$ solution.

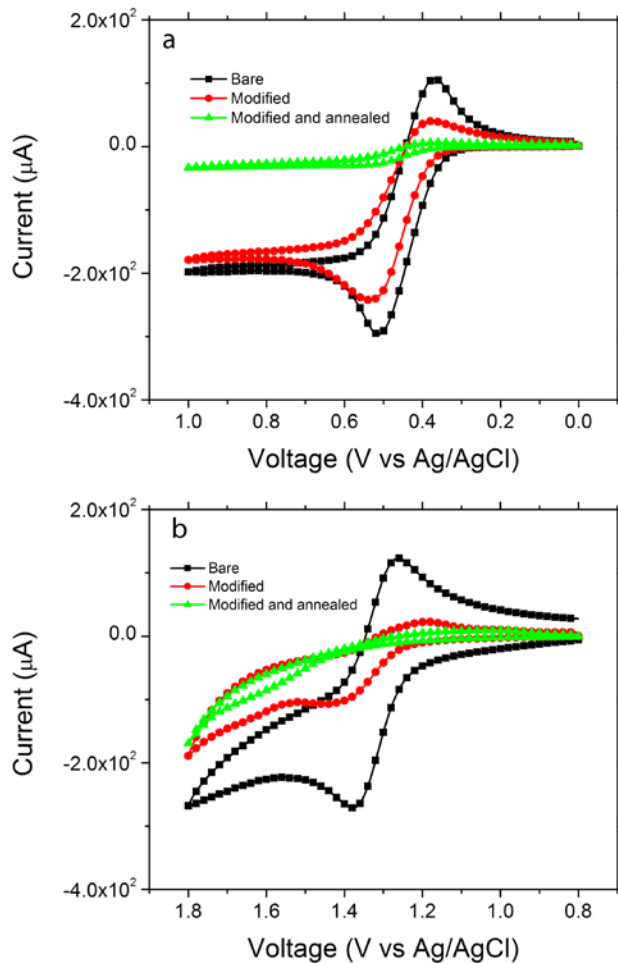


Figure 3.9. Redox-probe experiments for a *p*GMA. CVs of a) 5 mM ferrocene or b) 5 mM $\text{Ru}(\text{terpyridine})_2(\text{PF}_6)_2$ were taken with bare (square), as modified (square) and annealed (triangle) Pt electrodes. SE: 0.1 M $\text{TBAClO}_4/\text{ACN}$ and $v = 0.05$ V/s.

Figure 3.9 shows the importance of annealing the polymer layers to achieve better coverage on the electrode surface. When probed with a small neutral molecule (ferrocene), the as-modified layer still passed ~80 % of the current-density (determined

by peak height), while annealing the polymer at 80 °C for 12 h reduced the current to ~7%. For a larger, positively charged molecule (Ru(terpyridine)₂(PF₆)₂), the amount of current passed was only ~33 % and < 1 % of the original value for the as-modified and annealed layers, respectively. *p*GMA is a neutral polymer and a response due to charge exclusion is unlikely. Rather, the decrease in current for the annealed films can be attributed to a conformal coating on the nanometer scale after annealing. Rolison *et al.*³⁹ suggested heat-induced crosslinking and polymer-chain reformation as two possibilities for the increase in electrode coverage of annealed electropolymerized layers. It should be mentioned here that the Cu₂Sb films tested by solid-state impedance measurements were only annealed at 40 °C for 12 h to avoid Sb_(m) evaporation. The physical requirements of uniform polymer coverage and nanoscale thickness are achievable with *p*GMA.

The capability to conduct Li-ions is another vital part of a polymer electrolyte. The process can be achieved *in situ* through copolymerization (section 3.3), or *ex situ*, by doping the polymer with a Li-ion containing salt. Doping a polymer with Li-ion salt is experimentally the simplest route. The solvent used must not dissolve the polymer from the surface, but also must be capable of partially solvating the polymer to introduce the lithium salt. Evaporation of the solvent produces a solid polymer electrolyte.

Solution-phase doping of pGMA with LiClO₄

To establish Li-ion conductivity in *p*GMA, the polymer films were soaked in a 1 M LiClO₄/PC solution for 24 h and then annealed (experimental). The choice of GMA as a monomer was partly due to the presence of ethereal oxygens. Lithium conducting polymers with ethereal oxygens, such as PEO, have been used successfully in commercial batteries⁹. Dissolving ions within polymers preserves the electrical insulation

of a film and is the synthetically simplest route. The *p*GMA:LiClO₄ films were analyzed with XPS, SS impedance measurements and optical microscopy.

XPS of pGMA and pGMA:LiClO₄ films

The XPS survey scans of as-modified, annealed and LiClO₄-doped polymer films on planar Au, Pt, Cu and Cu₂Sb surfaces show that all the two-dimensional electrodes were completely modified with *p*GMA. Analysis of the HRES XPS scan can accurately determine the constituents of the polymer-film. In particular, it can provide direct evidence for salt-doping. Figure 3.10a is the HRES XPS scan over the Li 1s and Cl 2p region.

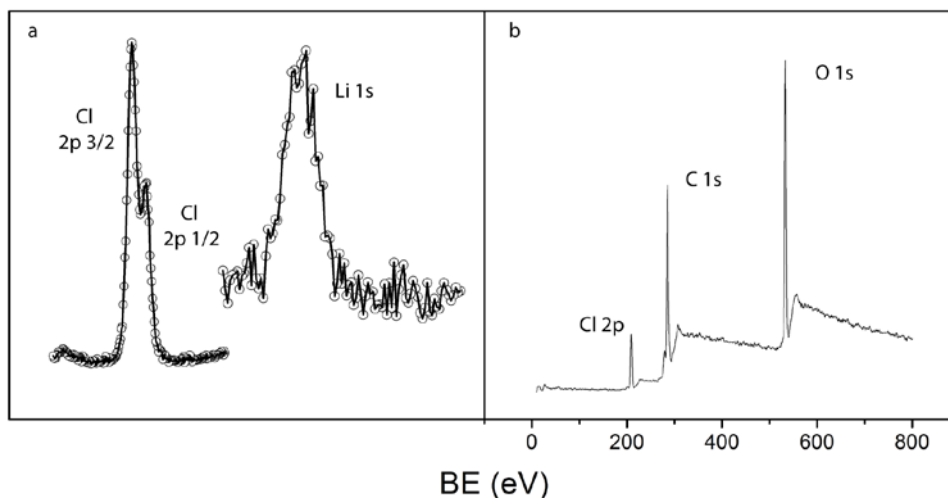


Figure 3.10 a) XPS HRES scans over the Li 1s and Cl 2p region and b) the XPS survey scan of a *p*GMA:LiClO₄ on Au.

The presence of a Li 1s signal and the position of the Cl 2p 3/2 peak (214.5 eV) establishes the presence of LiClO₄. The lack of any substrate peaks in the XPS survey scan (Figure 3.10b) after the doping process suggests that complete coverage of the electrode was retained. The doping of the polymer was accomplished before annealing to

ensure the maximum amount of salt was solvated by *p*GMA. No molecular probe experiments were completed after the doping procedure, but similar effects on uniformity are assumed when soaked or un-soaked films are annealed. Thickness measurements after doping show a ~107 % increase in thickness (Table 3.1), consistent with literature reports for similar doping procedures^{35,40}.

The consistent swelling of the polymer after the introduction of ions is important when designing AAO templates for NWA electrodes (Chapter 1). Optimal separation of anode and cathode will fully maximize the 3D battery architecture. The physical characteristics of *p*GMA and *p*GMA:LiClO₄ has met the requirements set forth by the Prieto Group battery design, the solid-state electrical characteristics will determine if the doped-polymer can be used as a solid-polymer electrolyte.

3.5 Solid-state electrical measurements of *p*GMA-modified electrodes

Making electrical contact to thin organic layers is not trivial^{38,41-43}. Previously, we have used reported liquid-metal methods to contact ≥ 15 nm films of *p*Zn(vbpy)₃. In the experimental section, a procedure is outlined to control the surface area of Ga-In eutectic electrical contacts. The new procedural step was key to calculating values for the ionic conductivity (σ_{ion}) of the polymer layer.

The two solid-state measurements used to ascertain the properties of the polymer were solid-state impedance (SS Imp) and linear sweep voltammetry (LSV). The results of a bare, as modified and LiClO₄-doped gold electrode are shown in Figure 3.11a, b and c, respectively. The two-point AC impedance measurement of a bare Au electrode (Figure 3.11a) is a point on the real impedance axis (Z_{real}) in the Nyquist plot. That point is a

summation of all the interfacial contact resistance in the system: 1) $W_{(m)}$ -wire/Ga-In interface, 2) Ga-In/Au interface and 3) stainless-steel (alligator clip)/ $W_{(m)}$ -wire or Au. The sum of these resistance values was $<2\Omega$, implying that the majority of any dielectric response could be attributed to the polymer. The LSV measurement (Figure 3.1.7a, inset) gives a linear current response when the potential was swept in the forward or reverse direction. The resistance calculated from Ohm's law is 2.5Ω , which is close to the value obtained from SS Imp measurements (3.1Ω).

The annealed *p*GMA layers were also subjected to solid-state electrical measurements to determine the dielectric properties of the polymer. The Nyquist plot (Figure 3.11b) shows a straight line that extends from $Z_{\text{real}} = 0$. The shape is characteristic of a dielectric material and can be modeled as a resistor and a capacitor in series. The theoretical capacitance of a dielectric material can be described by

$$C_{\text{theory}} = \frac{\epsilon \epsilon_0 A}{d} \quad (1)$$

where ϵ is the effective dielectric constant of the material, ϵ_0 is the permittivity of free-space, A is the area, and d is the distance between the electrodes. The capacitance is obtained by a fit to the impedance data. By using (1), values for the ϵ of *p*GMA were calculated (Table 3.2). The wide variation in values for the dielectric constant may arise from the different surfaces used to make the capacitance measurements. The ϵ values obtained with Au and Pt (2-3), typical non-blocking electrodes used in solid-state electrical measurements, are very similar to other polymer dielectrics. The dielectric window of *p*GMA is wider than 5 V, and no dielectric breakdown is observed for the polymer within that range (Figure 3.11b – inset). The result implies that *p*GMA is

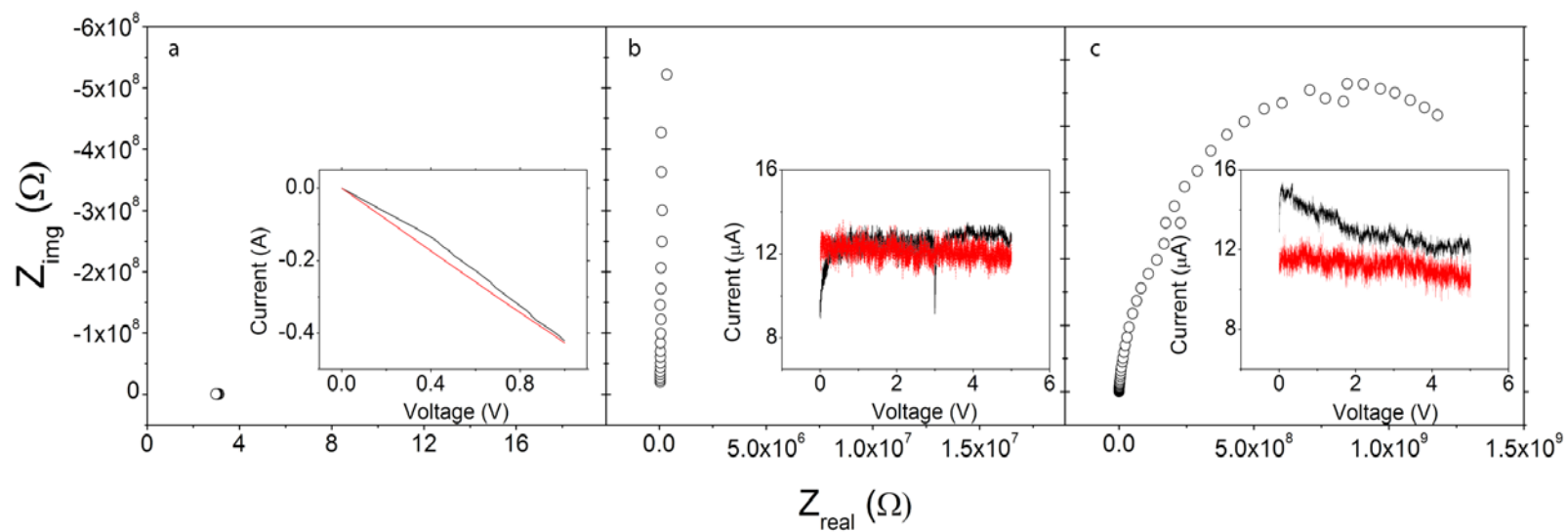


Figure 3.11 Solid-state electrical properties of pGMA. The Nyquist plots of a) bare Au electrode, b) pGMA modified and annealed Au electrode, and c) pGMA:LiClO₄ modified Au electrode are shown. The LSV results for the same electrodes are shown as insets.

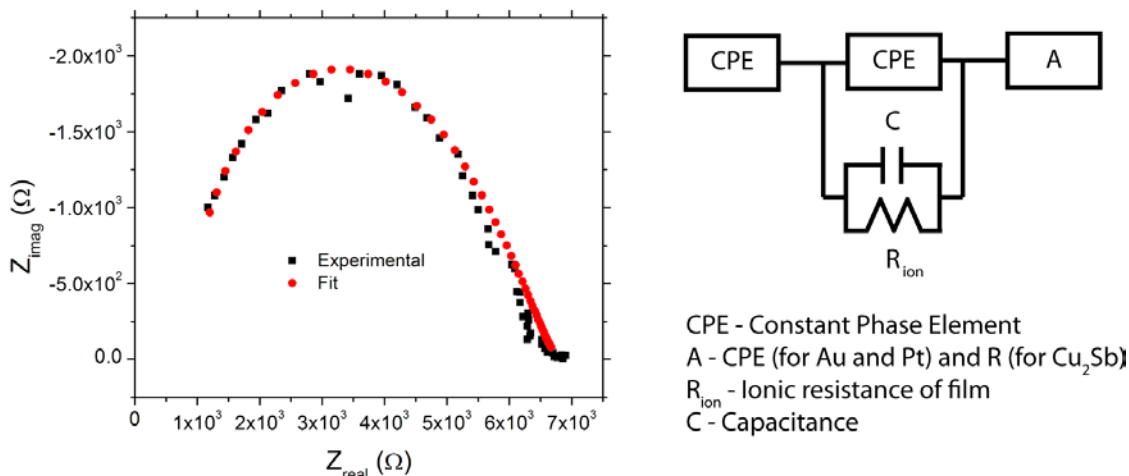


Figure 3.12. Nyquist plot of $p\text{GMA}:\text{LiClO}_4$ on Cu_2Sb (black). The fit to the data was modeled after the electrical circuit. Values for R_{ion} and C were generated from the mathematical model.

capable of withstanding > 5 V difference between the anode and cathode. The voltage difference in most Li-ion batteries is 3.0-4.2 V.

The retention of electrical insulation during salt-soaking is essential to the preparation of a polymer electrolyte. The drying procedure eliminates the majority of the PC used for doping. XPS HRES scans of the C1s region show no peak at 292.5 eV, indicative of the carbonyl carbon in PC. This suggests that the polymer films are not plasticized by the solvent within the analysis depth of the XPS (10-15 nm). The experimental plan includes solution-phase introduction (drop-cast or sol-gel) of the cathode, followed by an annealing step. Any liquid in the polymer could possibly evaporate during the annealing step and leave porous regions within the polymer. Therefore, maximizing the ionic conductivity in the solid-state is a key element to the 3D architecture.

Injection of Li-ions from the electrode into the polymer, diffusion of Li-ions from anode to cathode and injection from the polymer to the counter-electrode are all essential

processes for battery charging and discharging. The ionic conductivity of a polymer is expressed as a hemispherical shape in a Nyquist plot (Figure 3.1.7c). The LSV (inset) scans does not show a dielectric breakdown within +5 V after the doping procedure. Modeling the impedic response with the equivalent circuit presented in Figure 3.12, generates values for the R_{ion} . The ionic conductivity of the polymer is found with

$$\sigma_{ion} = d/(A * R_{ion}) \quad (2)$$

The values are presented in Table 3.2. Values for the ionic conductivity of $pGMA:LiClO_4$ on Cu_2Sb assume a 150 nm thick layer, but the difference in the σ_{ion} of $pGMA:LiClO_4$ on Cu_2Sb is large (10^5). There are two reasons that we hypothesize for the difference. First, the model for the impedic response of Cu_2Sb is slightly different than the model used on the metallic electrodes. Since Cu_2Sb can be reduced in the presence of Li-ions, a resistance to charge transfer replaced the CPE in the impedic model. Therefore, R_{poly} could encompass the flow of ions due to reduction at the Cu_2Sb electrode. Second, the annealing step for Cu_2Sb is done at a lower temperature (40 °C). XPS scans display no substrate peaks and SS Imp determined $pGMA$ to be an electrical insulator on Cu_2Sb . The effect of annealing temperatures on the solid-state electronic results of GMA is not fully analyzed. The lower annealing temperature may result in more PC being trapped between polymer chains. XPS HRES scans of $pGMA:LiClO_4$ do show the presence of PC on the surface, so the polymer may still retain doping solvent. Residual solvent would increase the thickness of the polymer and decrease the resistance to ion flow. Further investigations are needed to better understand impedic response of $pGMA:LiClO_4$ on Cu_2Sb .

Table 3.2. Solid-state electrical values of *p*GMA:LiClO₄ films on different electrodes.

Electrode	Capacitance X 10 ⁹ (F)	ε	σ _{ion} x 10 ⁻¹³ (S/cm)
Au	0.9 ± 0.4	1.9	2.5
Pt	1.1 ± 0.5	2.6	1.5
Cu	5.0 ± 2.7	8.9	3.2
Cu ₂ Sb	1.9 ± 1.2	3.91	5.3 x 10 ⁵

3.6 Discussion

The ionic conductivity of *p*GMA:LiClO₄ is far below the standard for battery operation, but the ~150 nm thick film is far thinner than 1-100 μm thick separators. The relevance of ionic conductivity values has been questioned when solid-electrolytes are in the < 50 nm regime.⁴⁰ We have not been able to experimentally validate this theory with *p*GMA up to this point because we have not succeeded in growing very thin layers. Controlling the thickness of *p*GMA:LiClO₄ with temperature, pressure or electrochemical techniques are possible avenues of research, but optical microscopy illustrates another issue with *p*GMA:LiClO₄.

The distribution of salts doped into an electropolymerized layer is also inhomogenous. The reason is that the doping of an electropolymerized layer is heterogeneous, relying on a solvent to only partially solubilize the polymer and introduce ions. Figure 3.13 are optical micrographs of Au electrodes that have been modified with *p*GMA (top), *p*GMA:LiClO₄ (middle), and *p*GMA-co-*p*LiMA (bottom). The large regions of salt clustering are present when the polymer is doped with LiClO₄. To fully utilize the power of the nanowire architecture, uniform conductivity of Li-ion between the electrodes is

required. The synthesis of *p*GMA-co-*p*LiMA is discussed later in this dissertation, but the optical image clearly shows far smaller regions of salt clustering than the doped homopolymer. Finding a copolymer for *p*GMA is the focal point of the next sections in this chapter.

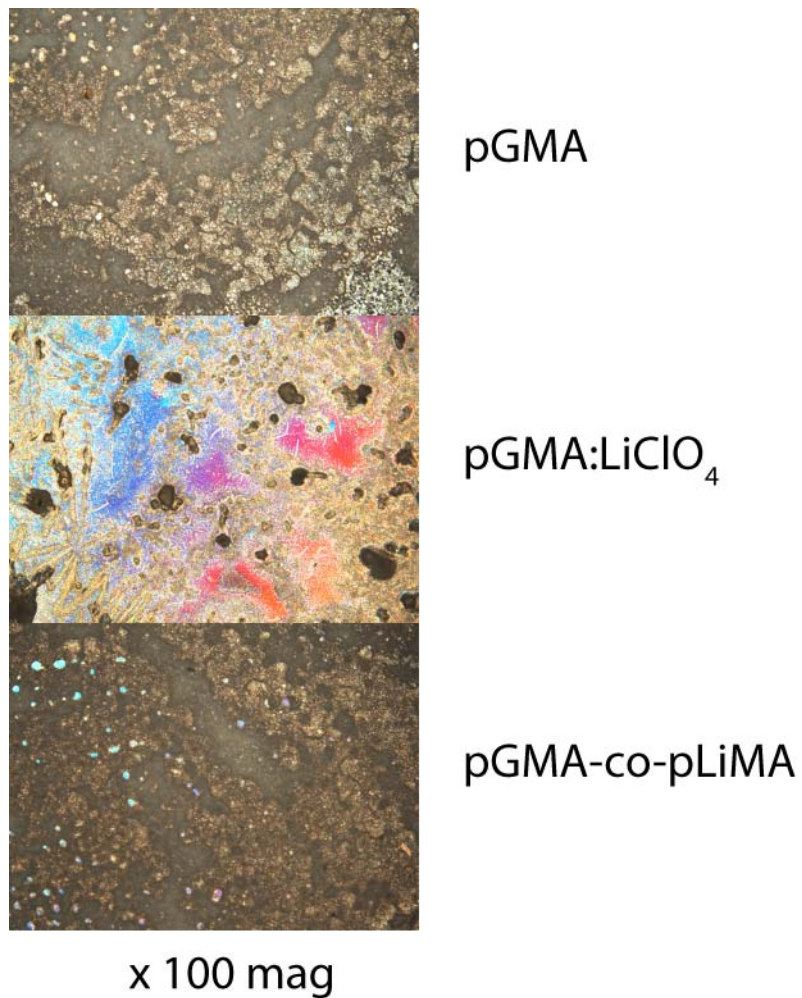


Figure 3.13 Optical micrograph a) *p*GMA, b) *p*GMA:LiClO₄ and c) *p*GMA-co-*p*LiMA.

3.7 The aqueous electropolymerization of KSPA

The experimental plan is to co-polymerize GMA with a lithium-ion conducting salt. The desired properties are: 1) the monomer's solubility in DMF 2) the monomer's capability to be reductively polymerized at potentials negative of Cu_2Sb electrochemical stripping, and 3) the monomer's cation must be Li^+ or easily substituted with Li^+ . As a target molecule, tetramethylammonium 3-sulfopropyl acrylate (TMASPA) was chosen. The synthetic precursor to the target molecule is potassium 3-sulfopropyl acrylate, a water-soluble molecule with a polymerizable vinyl tail and an anionic sulfonate head group (Chapter 3.1). Theoretically, the deposition of a thin ionomer would not require copolymerization with GMA. The ionomer would also have to withstand the physical and electrical restraints of a polymer electrolyte. As our group is very interested in aqueous electrochemistry, an attempt to electropolymerize KSPA out of water was undertaken.

The potentiodynamic scans for the electropolymerization of 2 M KSPA/DD H_2O are shown in Figure 3.14. If the voltage limits are set from 0 V to -1.20 V (Figure 3.14a), then reductive current begins to flow at a potential of $E_{\text{oc}} = -0.80$ V. On the reverse scan the appearance of two anodic peaks, $E_{\text{pa1}} = -0.60$ V and $E_{\text{pa2}} = -0.52$ V, is interesting because the potentiodynamic electropolymerization of acrylate monomers reported in the literature^{16,26,29}, and from our own results, never display any Faradaic oxidation current. A new cathodic peak, $E_{\text{pc}} = -0.72$ V, appears during the second cycle and the current of E_{pa1} and E_{pa2} grow in magnitude. The increase in current with each proceeding cycle resembles the electrochemical growth of conducting polymer on electrode surfaces. The E_{pc} peak height grows linearly up to 15 cycles, but after that point, the current remains

constant. The peak separation between E_{pa1} and E_{pc} , $\Delta E = 0.12$ V, suggests a coupled 2 electron transfer, but the large monomer concentration creates non-ideal solution conditions. According to the Nernst-Planck equations, migratory effects cannot be

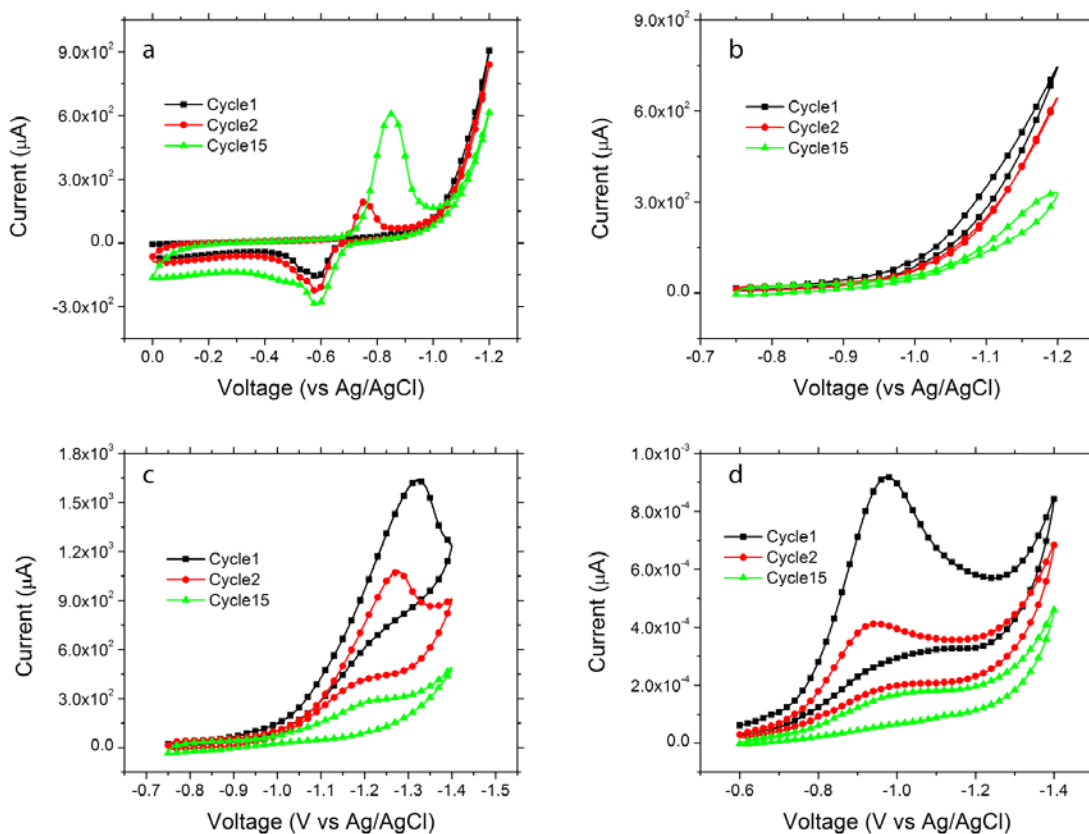


Figure 3.14. Potentiodynamic cycling of 2 M KPSA/DD H₂O on an a-c) PITO electrode and a d) planar Cu electrode. The difference potential limits for CVs a-c alter the response of electrode.

discounted under such conditions. If the voltage window is narrowed from -0.75 V to -1.20 V (Figure 3.14b), then E_{pc} does not appear in the potentiodynamic response indicating that the peaks are indeed coupled. Also, no observable faradaic current passed in the voltage window of 0 V to -0.70 V (not shown). Therefore, both E_{pa} and E_{pc} both rely on the initial reduction E_{oc} .

If the voltage limits are extended to a more reductive potentials, -0.75 V to -1.4 V (Figure 3.14c), then the current response is very similar to the electropolymerization of *p*GMA. The increase in current, E_{oc} , initially thought to be hydrogen evolution, forms a peak $E_{pc2} = -1.32$ V (cycle 1). The cathodic signal is the initiation of KSPA. The aqueous deposition of *p*KSPA is possible on all surfaces attempted: ITO, Pt, Au, Cu_2Sb and Cu (Figure 3.14d) and the potentiodynamic decrease in current with each cycle is consistent between electrodes. To simulate the electropolymerization of *p*GMA (section 3.1), all *p*KSPA films for future analysis were made by cycling the 2 M KSPA/DD H_2O between -0.6 V and E_{pc2} . The position of the cathodic wave for different surfaces sheds light on the surface-dependent energy required for direct electropolymerization of acrylate monomers on conducting surfaces.

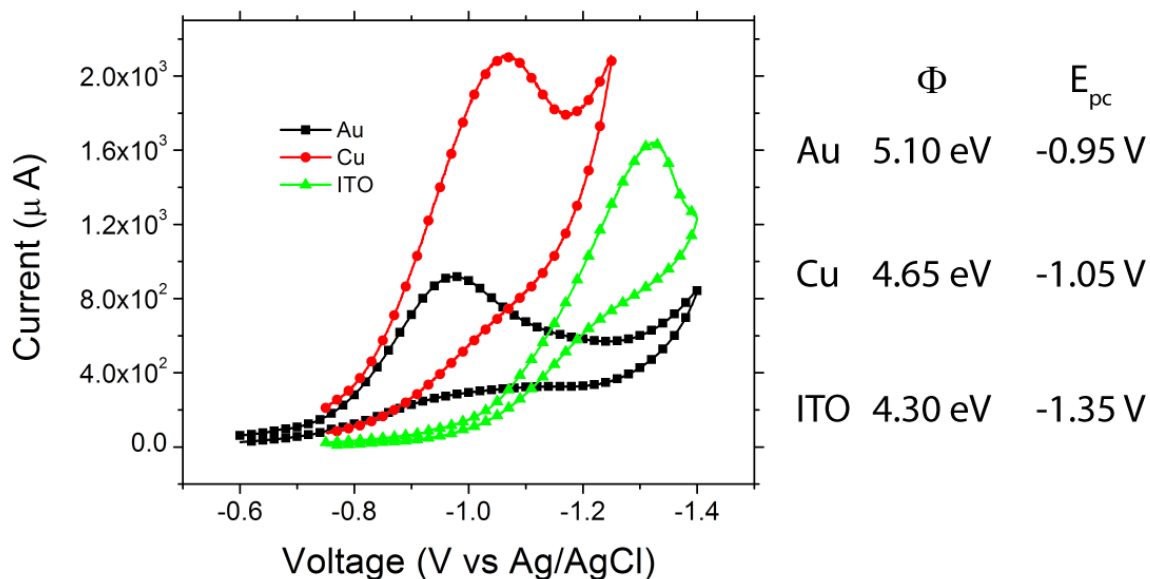


Figure 3.15. Cyclic voltammograms of 2 M KSPA/DD H_2O on a Au (square), Cu (circle) and ITO (triangle). A comparison of the work function (ref) to peak potential between electrodes is shown on the right.

The preferential electropolymerization of methyl-acrylonitrile, reported by Charlier *et al.*³⁰, describes the relationship between the work-function of a material (Φ) and the preferential growth of the electrografted polymer. Metals with lower work functions required a greater reduction potential to initiate polymerization. That theory is reflected through the shift in cathodic peak potentials for the electropolymerization of *p*KSPA on different surfaces (Figure 3.15).

The importance of having a homogenous surface for electropolymerization is essential to forming a conformal polymer layer. If a surface is comprised of multiple materials, then the monomer will preferentially polymerize on the surface with the higher work function. Charlier *et al.* conclude that composite materials will result in inhomogenous, or selective, polymer grafting. The flat, homogenous and conducting surface of ITO makes analyzing the physical characteristics of the anionic homopolymer simpler.

3.8 Physical characterization of *p*KSPA

*XPS of *p*KSPA*

An ITO electrode reduced in a 2 M KSPA/DD H₂O from -0.75 V to -1.32 V (E_{pc2}) with *p*KSPA is covered by an interesting, colored film. The elemental make-up of the film was determined through XPS survey and HRES scans. Figure 3.16a displays the HRES scans over the K 2p and S 2p regions. The elements are specific to the cation and anion of the polymer. The peak position for the S 2p 3/2 peak (167.8 eV) is significant because it distinguishes the sulfur in the deposited layer from any sulfide (160-164 eV) or sulfate (169-171 eV) decomposition products. The XPS survey scan displays a strong In 3d signal over the substrate region (Figure 3.16). The *p*KSPA layer is either extremely

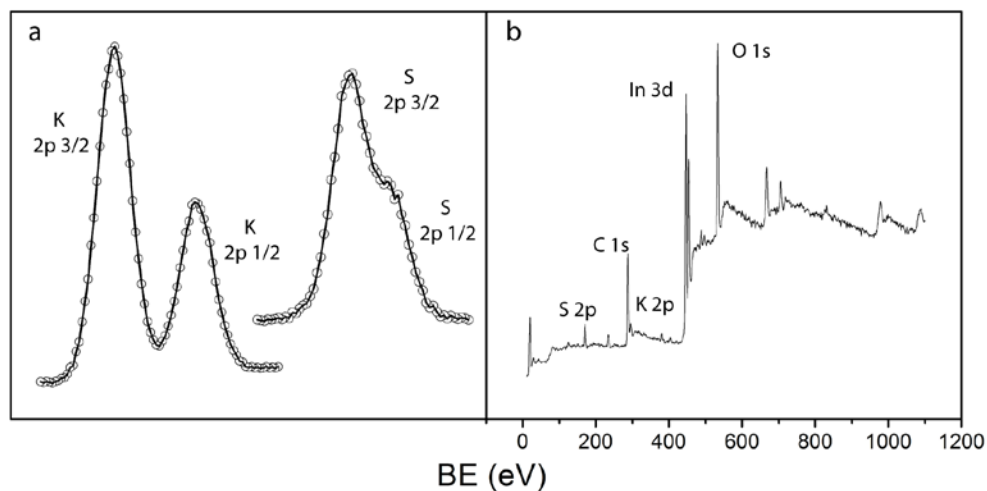


Figure 3.16. a) XPS HRES scans of the K 2p and S 2p regions of a *p*KSPA-modified ITO electrode. The b) survey scan of the electrode display a strong substrate (In 3d) signal.

thin or leaves an exposed electrode surface. The survey scan from all electrodes tested showed similar results for the K 2p and S 2p peak positions, but substrate peaks were also present.

Table 3.3 gives the values for the S 2p peak positions of KSPA and of *p*KSPA on different electrodes. On all electrodes, the S 2p 3/2 peak position (~167.5 eV) for the monomer indicates that the sulfur in the polymer is in the same chemical environment as the sulfur in the monomer. The table also gives atomic ratios between the S 2p peak and substrate peaks. Interestingly, the polymer to substrate ratios are similar between the electrodes, suggesting another factor besides electrode material that is controlling the amount of polymer on the surface.

XPS spectra is the first indication that the homopolymerization of *p*KSPA might not meet the stringent uniformity requirements of the 3D architecture. We wanted to elucidate if the patchiness of the polymer is random or patterned across the surface of

ITO. A nanoscopic structural analysis of the surface could provide vital insight about the growth of the anionic polymer.

Table 3.3. S 2p position and substrate to anion ratios of *p*KSPA on multiple surfaces. Data is obtained from curve-fit analysis of XPS HRES scans.

Sample	S 2p 3/2 (ev)	Atomic Ratio (Peak) Substrate : S 2p
ITO	167.8	(In 3d) 9.5 : 1
Au	167.7	(Au 4f) 11 : 1
Pt	167.7	(Pt 4f) 11 : 1
Cu	167.8	(Cu 2p) 10 : 1
Cu ₂ Sb	167.8	(Cu 2p) 10.5 : 1
Monomer	167.5	----

AFM measurements of pKSPA on ITO

The benefit of electropolymerizing on an extremely flat surface like ITO is the capability to determine the height of very thin conformal polymer layers (Chapter 2.3). When attempting to scratch through the layer of *p*KSPA, a visible scratch pattern was not apparent. Successful experiments using the “scratch” method to determine polymer thickness were not accomplished. However, AFM analysis is still very useful.

Differences in the line profiles of a bare ITO electrode and one modified with *p*KSPA is shown with the AFM topography micrograph in Figure 3.17. The 62 ± 29 nm rms value for the modified electrode is much larger than the 17 ± 8 nm rms roughness value of bare ITO. The AFM topography image displays no large features that would indicate non-uniformity. The height distribution of the $25 \mu\text{m} \times 25 \mu\text{m}$ AFM image is shown in Figure 3.18. The broader distribution for the modified ITO indicates deposition of a layer on the surface of the ITO, but the monomodal distribution suggests that the thickness of *p*KSPA is consistent within the sample region.

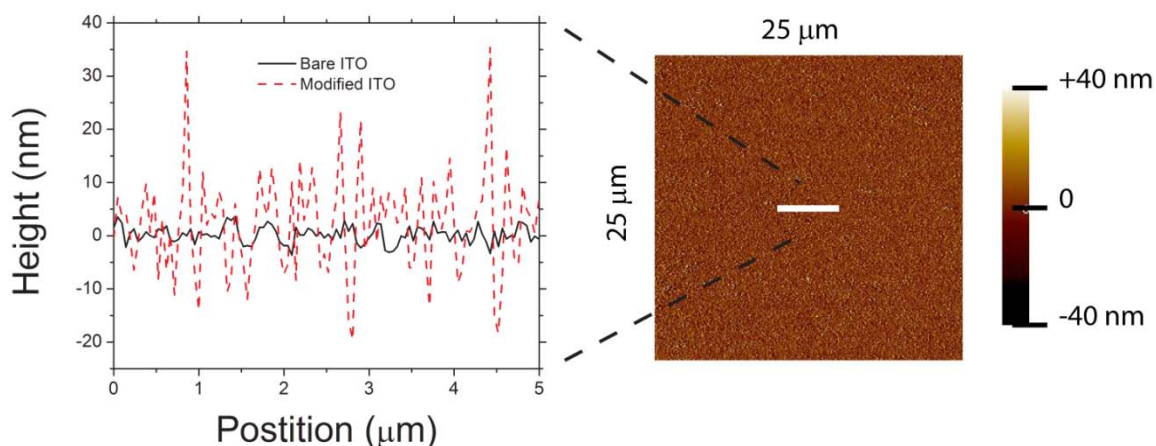


Figure 3.17. AFM topography micrograph of a *p*KSPA-modified ITO electrode. The line profile of a bare (straight) ITO electrode is compared to a *p*KSPA-modified (dash) ITO electrode.

In conjunction with XPS measurements, the presence of *p*KSPA can be confirmed with AFM analysis. The presence of substrate peaks in the XPS survey scans tell us that the 34 ± 5 nm features seen in AFM images are isolated islands of polymer. If we analyze multiple line-profiles in both the x and y direction, then we see that features ≥ 30 nm tall are about $0.5 \mu\text{m} \times 0.5 \mu\text{m}$ and spaced $1.7 \pm 0.2 \mu\text{m}$ apart. The XPS analysis-depth is only $\sim 10\text{-}15$ nm and the detection substrate peaks excludes complete polymer coverage. The polymer would have to be less than 10-15 nm in height, and AFM measurements show regions which are 30 nm. Therefore, we conclude that the aqueous electropolymerization of KSPA produces islands of polymers on the electrode surface.

Potentiodynamic scanning for more than 15 cycles does not produce a polymer layer with taller features; however, the polymerization solution does become very viscous.

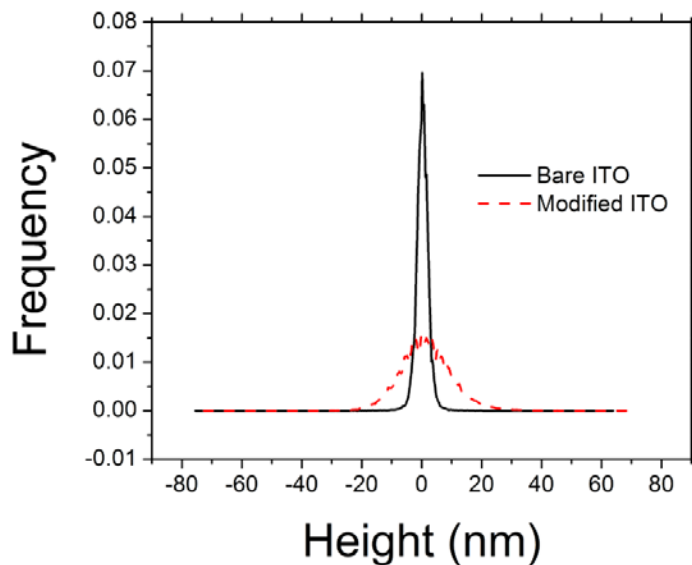


Figure 3.18. Height distribution of a bare (straight) and *p*KSPA-modified ITO electrode.

Bulk polymerization is being initiated on the electrode surface, and the multiple cycles are electrochemically initiating polymerization in solution. Island growth of *p*KSPA on ITO stops after the polymeric regions reach 34 ± 5 nm in height. We will display that the lack of sustainable growth of the polymer is also observed spectroscopically.

UV-Vis measurements of pKSPA on ITO

The discoloration of ITO by the electropolymerization of KSPA led us to perform a UV-vis spectroscopic investigation of *p*KSPA on the surface of ITO. Figure 3.19 shows an absorbance maxima from the polymer layer at $\Delta_{\max} = 310$ nm. The growth of the peak is linear up to 15 cycles. This result resembles the linear growth of E_{pc} (Figure 3.14a) during the potentiodynamic electropolymerization of KSPA on ITO; that is, E_{pc} stopped growing after 15 cycles when cycled at $v = 0.1$ V/sec. Cycling past 15 cycles does not produce spectra with higher Δ_{\max} values. The absorbance of the 50 cycle modified ITO sample does have a slightly lower absorbance between 400 nm and 600 nm.

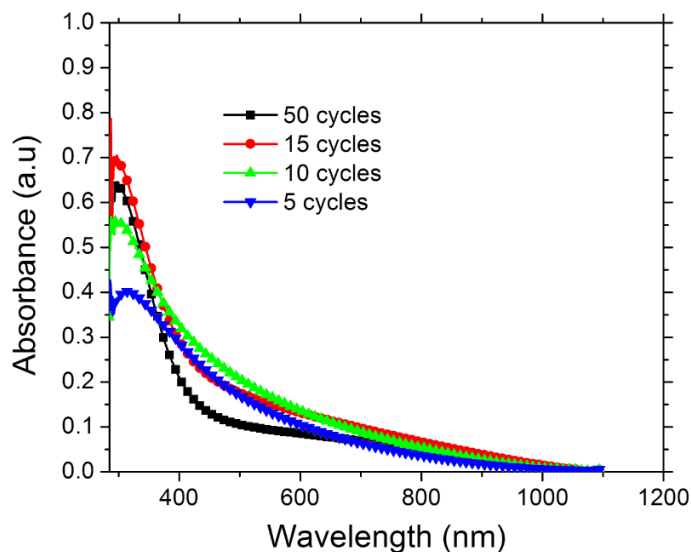


Figure 3.19. UV-Vis spectra of *p*KSPA-modified ITO electrode.

UV-Vis measurements confirmed the growth of a layer on the surface of ITO. The polymer thickness is limited, and AFM micrographs illustrate the uniform distribution of polymeric regions. However, if the conducting regions between the polymer are too prevalent, then liquid-metal methods could make direct contact to the substrate. Contact to individual polymer regions is not possible, and the electronic characteristics would be a summation of responses over the entire liquid-metal contact (4.2 mm^2).

3.9 SS electrical measurements of *p*KSPA-modified electrodes

All electrodes are electrically conducting when modified with *p*KSPA. The resistance observed with SS impedance measurements are within the same range as the resistance calculated with LSV measurements ($5 - 15 \Omega$), and similar to the resistance of a bare electrode. Annealing of the electrodes at $80 \text{ }^\circ\text{C}$ does not alter the SS electronic measurements. Islands of *p*KSPA are electrically conducting or spacially too far apart, the latter allows for direct contact between conducting electrodes. Though the solid-state

electrical results are disappointing, understanding the electropolymerization of a monomer with an anionic backbone is a step towards the goal of co-polymerization.

3.10 Discussion

The aqueous electropolymerization of KSPA promotes electrochemical island growth of a polymer. The results are not unique to the electropolymerization of sulfonated-monomer backbones. In the oxidative electropolymerization of sodium 4-hydroxybenzenesulfonate (HBS) to make poly-4-sulfonic acid-1,2-phenylene oxide (*p*SPO) by Rolison *et al.*³⁹, the presence of aggregates between 20-50 nm was detected. Though extensive cycling work was not reported, the authors claim that the polymerization is not self-limiting and thick films of the polymer are capable of forming on the electrode surface. The authors attribute the island growth to the presence of oligomers that preferentially aggregate instead of adhere to the ITO surface. Here, we continue the discussion for electrochemical growth of *p*KSPA.

The importance of charge in electropolymerization is first observed with the formation of *p*Zn(vbpy)₃ on surfaces. During our study of the system, we confirmed literature reports that the 1 electron reduction of the Zn(vbpy)²⁺ monomer results in patchy deposition. The monocationic monomer is still capable of polymerizing, but the growth is not conformal due to the repulsive coulombic positive charge. Charge is partly responsible for the patchy growth of *p*SPO. During electro-oxidation of HBS, the anionic backbone is reduced to a formal charge of 0 and a uniform layer can initially form on the surface of the electrode. It is unknown whether the formation of clusters is driven by attractive forces between oligomers, repulsive forces between sulfonate groups, or a

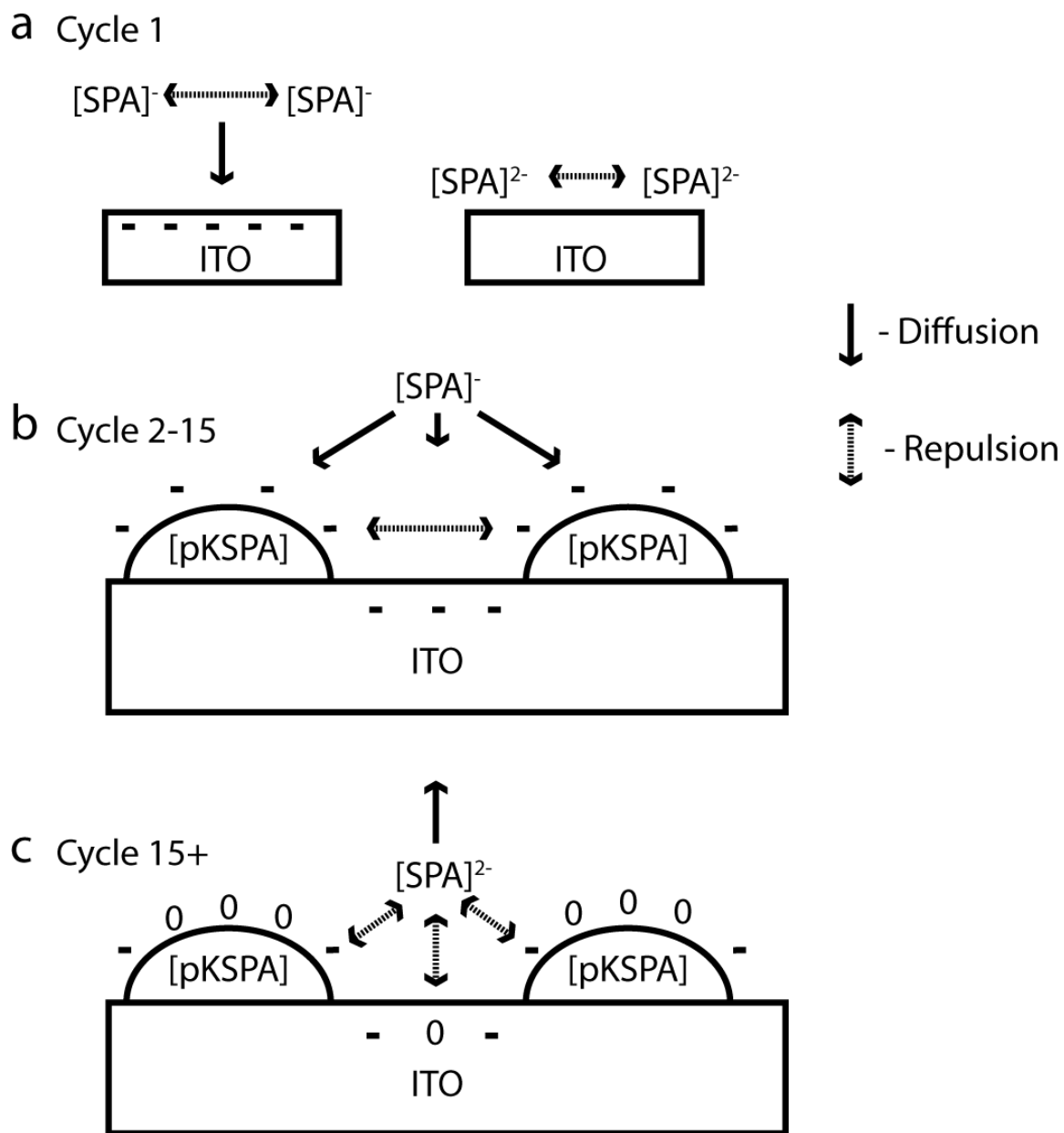
combination of both. From that point, the aggregation of the polymer promotes island growth. The concentration of monomer at the top of the island is higher due to the lower solubility of monomer solution at the base of the aggregates. Once aggregates form, preferential growth of the polymer is towards the bulk solution.

The electro-reduction of KSPA accentuates the repulsive forces between monomer units on a surface (Scheme 3.1a). Assuming a one electron transfer, the reduction of the monomer increases the formal charge of the molecule to $[\text{SPA}]^{2-}$. The dicationic moieties repel each other before and after the electron injection step. In contrast, the oxidized $[\text{HBS}]^0$ does not have any coulombic repulsion during the initiation step, therefore polymerization between the islands may occur. Rolison *et al* do not report the presence of an In 3d substrate peak during XPS analysis, but there is mention of an extra oxygen peak attributed to ITO. Of interest to note here, the physical dimensions observed for the *p*SPO clusters, $1\ \mu\text{m} \times 1\ \mu\text{m}$, are twice as large as the *p*KSPA islands. The repulsion between the *p*KSPA units is constant under reducing conditions, keeping large areas of ITO exposed (Scheme 3.1b). Propagation of the polymer continues with subsequent cycles but happens preferentially on the top of the islands. Growth continues until *p*KSPA cannot conduct electrons to the top of the islands (Scheme 3.1c). For the potentiodynamic polymerization of KSPA, this limit occurs ~15 cycles into the polymerization ($v = 0.1\ \text{V/s}$). Current still passes as island growth limits because the monomer can still be reduced by the bare ITO regions between the islands; however, strong coulombic repulsion forces (a combination between the negatively biased ITO electrode and the electro-reduced base of the polymer islands) propel the $[\text{KSPA}]^{2-}$ into

the bulk. The initiation at the electrode surface and bulk polymerization continues with repeated cycling, increasing the viscosity of the solution.

The charge-driven island formation during the reductive electropolymerization of anionic monomers does not provide the electrode coverage required for a successful polymer electrolyte. The missing polymeric regions are too extensive; cathode materials could hypothetically make direct contact to the anode. Later in this chapter, we reductively electrodeposit *pLiMA*. The results from the homopolymerization of *pKSPA* help us to understand limitations of a polymer with an anionic backbone. Interestingly, the physical and electronic properties are similar between the two systems.

The co-polymerization of an anionic monomer with a neutral one will solve the unique problems expressed by the homopolymerization of each monomer. To resolve the non-uniform distribution of LiClO_4 in *pGMA*, the *in situ* electropolymerization of an anionic monomer can evenly distribute ions through *pGMA*. The uniform deposition of the polymer layer will be controlled by the electropolymerization of *pGMA*. Together, the formation of a thin and uniform polymer electrolyte is achievable.



Scheme 3.1. Proposed formation method of *p*KSPA islands during the potentiodynamic polymerization of KSPA. a) Diffusion of the anionic monomer, [SPA]⁻, to the surface, electron injection and surface repulsion. b) Diffusion of fresh monomer to the tops of the *p*KSPA islands. c) Repulsion of surface initiated monomer to the bulk of the solution.

3.11 Towards electro-copolymerization of polymer electrolytes for Li-ion batteries

Important discoveries were made during in the electroreductive polymerization of GMA and KSPA. The direct deposition of *p*GMA requires a clean and chemically homogenous surface to produce conformal and thin polymer layers. Redox-probe experiments shows that nanoscale coverage of *p*GMA is not achieved without annealing the polymer at 80°C under vacuum for 12 h. The salt-doping procedures are successful in producing a dry, polymer layer with solid-state ionic conductivity. The reductive electropolymerization of KSPA is not conformal, and does not meet the stringent requirements of the nanowire architecture⁴⁰; that is, the coulombic repulsion of anionic monomers promotes island growth. As a result, direct contact between the liquid-metal eutectic and the underlying ITO creates a direct pathway for electrons to flow, and the solid-state electronic properties of the islands could not be ascertained.

During co-polymerization experiments, Cu₂Sb and Pt planar electrodes were simultaneously modified, but annealing temperatures were decreased to 45 °C under vacuum for 24 h. Decreasing the annealing temperature may result in solvent being present in the polymer. Complete coverage of the electrode is illustrated via XPS, and dielectric solid-state properties are observed for both electrodes. Here, we present potentiodynamic observations, evidence of copolymerization via XPS, and solid-state impedance results for the copolymerization of lithium methacrylate (LiMA) and glycidyl methacrylate (GMA).

3.12 The electropolymerization of LiMA

LiMA has many attractive qualities as the anionic monomer for co-polymerization: 1) it is highly solubility in DMF, 2) it is electrochemically active when scanned over similar potentials to GMA polymerization, and 3) it is a Li-ion salt. The potentiodynamic cycling of 0.5 M LiMA/DMF on Cu₂Sb and Pt is shown in Figure 3.20a and b, respectively. Both electrodes display a reduction and an oxidation peaks, though the current reponse with cycle number is different for both electrodes.

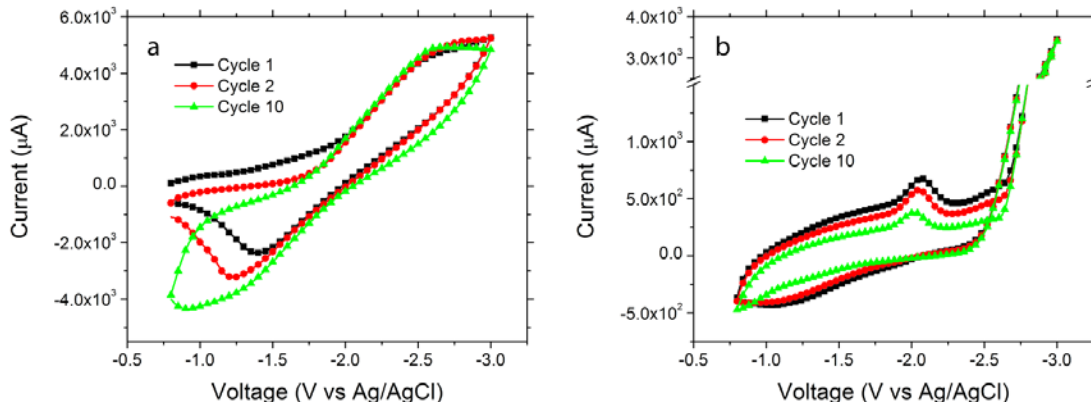


Figure 3.20. The potentiodynamic electropolymerization of 0.5 M LiMA in DMF on a) Cu₂Sb and b) Pt planar electrodes. SE: 0.1 M TBAClO₄/DMF and $v = 0.2$ V/s.

The electroreduction on a Cu₂Sb electrode displays a broad cathodic signal, $E_{pc} = -2.75$ V, and a corresponding oxidation, $E_{pa} = -1.25$ V (1st cycle). The anodic peak grows in intensity and shifts to more positive potential, $E_{pa} = -1.05$ V (10th cycle). During SEI analysis (Chapter 4), we observe the intercalation of Li-ions into Cu₂Sb at 0.9 V (vs Li/Li⁺). The corresponding potential is -2.3 V vs Ag/AgCl, 0.7 V less reducing than the voltage applied to the Cu₂Sb. In the presence of Li-ion salts, the Li-ion intercalation into the electrode limits the possible reduction potential. Oxidation of the lithiated anode

releases the Li-ions back into solution, but the charge passed during the experiment is a combination of multiple processes. The reduction of Cu_2Sb to Li_3Sb happens in three electrochemical steps, and E_{pc} could be reflective of any or all three of the processes. Electropolymerization on Pt shows us that LiMA is also electrochemically active in the potential window. The results suggest that an alteration to the polymerization potentials or method is necessary to avoid charging the anode during polymer modification.

The electropolymerization on the Pt electrode under the same potential limits is much different. On Pt, the cathodic peak, $E_{\text{pc}} = -2.15$ V, and the anodic peak, $E_{\text{pa}} = -1.25$ V, decrease in intensity as the electrode was cycled between -0.8 V and -3.0 V. The decrease in charge passed is similar to the potentiodynamic cycling of *p*GMA and *p*KSPA. Non-conformal growth of the polymer on the surface is confirmed by the presence of substrate peaks during the XPS survey scans. The presence of a corresponding E_{pa} is also a difference to be noted.

The electrochemical results from the formation of *p*LiMA helped us set the potentiodynamic window from -0.8 V to -2.3 V vs Ag/AgCl. The potentiodynamic copolymerization of 1.5 M GMA and 0.5 M LiMA (Figure 3.20a) on Pt is similar to the homopolymerization of *p*GMA (Figure 3.5) on Au. Specifically, the cathodic charge passed decreases as the potential is cycled, and the CVs display no observable oxidation current. The presence of a reduction peak, $E_{\text{pc}2} = -2.25$ V, is preceded by a shoulder, $E_{\text{pc}1} = -1.75$ V. XPS survey scans always detect the presence of Pt peaks after annealing the electrode at 45 °C for 24 h, indicating to us that the potentiodynamic copolymerization produces patchy films. Solid-state impedance experiments also indicate ohmic contact between the Ga-In eutectic and the underlying Pt electrode. Though

changing the potential window during co-polymerization successfully eliminates oxidation current from the electrode response, the dynamic polymerization method does not successfully generate uniform films. A change in the applied electrochemical waveform was made to address these concerns.

3.13 The electropolymerization of *p*GMA-*co-p*LiMA

To alleviate concerns about the electrochemical oxidation of LiMA, copolymerization was attempted under reducing potentials only. A “sweep-step” method (experimental), reported for the reductive electropolymerization of vinylic monomers by Chalier *et al.*³⁰, is also capable of producing thin films of *p*GMA. The applied waveform for the polymerization method is shown in Figure 3.21b. The potential was swept from -0.8 V to A (A = -1.95 V for Cu₂Sb and A = -1.8 for Pt) vs Ag/AgCl at $v = 5 \times 10^{-3}$ V/s and held at A V for 150 sec. The “sweep-step” current response of a Pt electrode in a 1.5 M GMA/0.5 M LiMA/DMF solution is presented in Figure 3.21c. The choice of ending potential is 50 mV more reductive than the shoulder observed in the potentiodynamic deposition. Experiments to discern the origin of the E_{pc1} and E_{pc2} are still on-going, but choosing an ending potential for the “sweep” step between the two signals would hopefully incorporate both polymers into the deposited layer. Conformal, thin films are visible on the surface of Pt and Cu₂Sb electrodes. XPS survey scans detect no Cu 2p or Pt 4f signals and the Ga-In eutectic does not make direct contact to the electrode surface during solid-state electrical measurements.

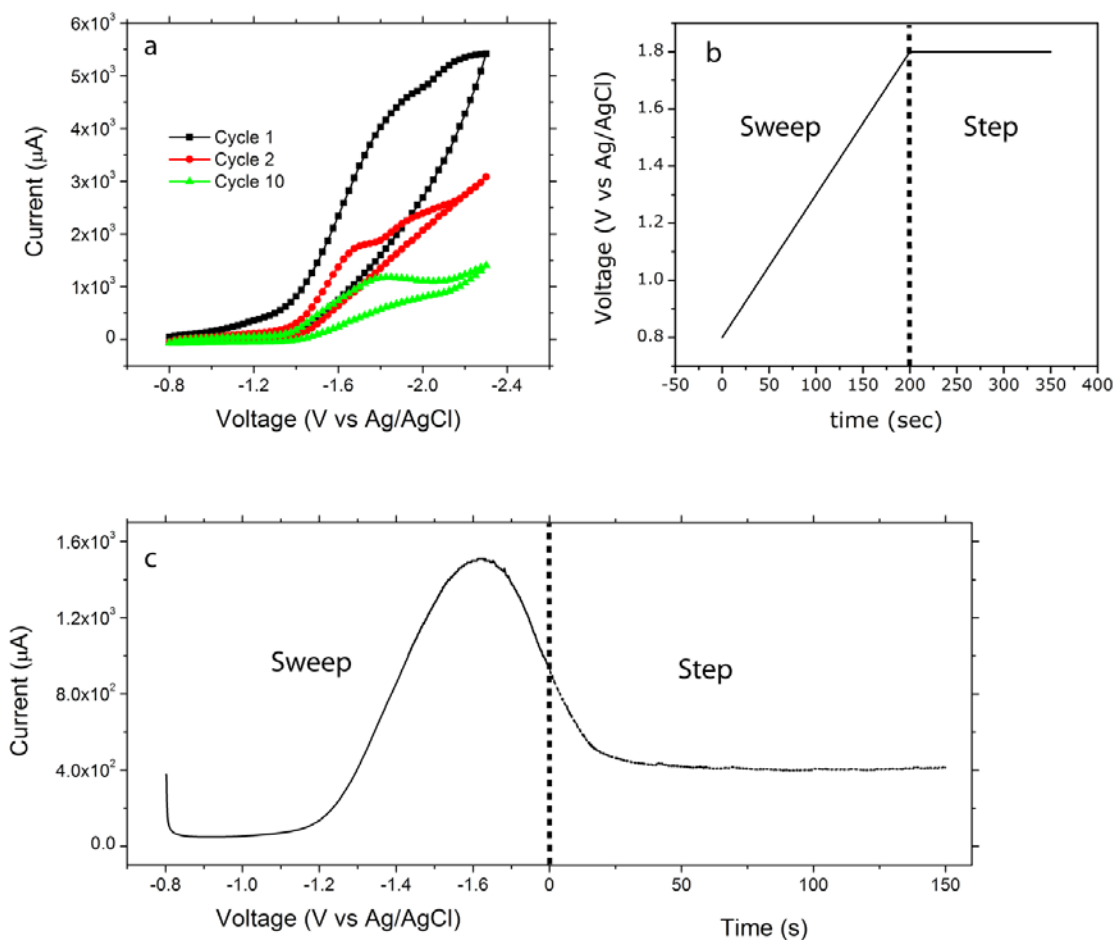


Figure 3.21. a) The potentiodynamic electropolymerization of 1.5 M GMA/0.5 M LiMA in DMF on Cu₂Sb. SE: 0.1 M TBAClO₄/DMF and $v = 0.2$ V/s. b) The "sweep-step" potential wave-form for electropolymerization on Cu₂Sb. c) The "sweep-step" current response of 1.5 M GMA/0.5 M LiMA in DMF on Cu₂Sb.

3.14 Physical characterization of *p*GMA-*co-p*LiMA

The incorporation of LiMA in the comonomer-derived films may result from various processes: 1) LiMA is reduced and forms a *p*LiMA phase that separates or is solvated by a *p*GMA phase; 2) LiMA monomers are immobilized within a *p*GMA polymer phase; 3) LiMA and GMA chemically couple to form a copolymer. Any combination of these processes may also take place. Reduction rates, stability of reduced monomers and

annealing under vacuum are all factors that can affect the structure of the co-polymer. The polymer film will be referred to as *pGMA-co-pLiMA*, though copolymerization is only one of the possibilities.

XPS of pGMA-co-pLiMA

The elemental make-up of *pGMA* and *pLiMA* is mainly oxygen and carbon, and since hydrogen is invisible to X-rays in XPS, then the Li-ion is the only difference between the two polymers. The evidence for *pLiMA* deposition is shown through HRES XPS experiments. Furthermore, analysis of the C 1s peak in the XPS HRES scans reveals interesting differences between the homopolymers and *pGMA-co-pLiMA*.

The binding of core electrons is sensitive to the chemical environment of the element. For example, the C 1s peak of $-\text{CF}_3$ will be at distinguishable higher binding energies than the C 1s peak seen for $-\text{C}(\text{CH}_3)_3$ because the electronegativity of the F atoms will increase the effective nuclear charge (Z_{eff}) of the carbon. When the carbon is excited with high energy X-rays, the higher Z_{eff} causes ejected photoelectrons to have a lower kinetic energy (or higher binding energy). Through careful fitting of XPS HRES scans, precise comparisons of peak positions can be analyzed.

The C 1s XPS HRES scans of LiMA and *pLiMA* are shown in Figure 3.22a. The monomer (top) fits to two peaks. The splitting of the peaks is due to the different environments of the alkane carbons ($=\text{CH}_2$, $-\text{CH}_3$, $=\text{C}-$) and the carbonyl carbon ($\text{O}-\text{C}=\text{O}$), labeled peak I and III respectively. When the peak for the alkane carbons is aligned to 284.7 eV, the splitting between I and III is retained. The quantitative analysis between the different C 1s signals suggests retention of the LiMA backbone during polymerization (Table 3.4). A Li 1s signal for *pLiMA* (Figure 3.22c) means that lithium

remains the mobile counter-ion after polymerization; although the atomic ratio of C:Li is slightly higher for *p*LiMA. As previously mentioned, the homopolymerization of LiMA is patchy; that is, substrate peaks are observed in the XPS survey scans. The similarities between LiMA and KSPA monomers suggest similar coverage results for the reductive electropolymerization. The growth of *p*KSPA islands on the surface of ITO is hypothesized to originate from coulombic repulsion between reduced anionic backbones (Chapter 3.10). The size of the islands may be different due to the steric differences between the monomers, but the repulsion forces remain. Therefore, the presence of substrate peaks is due to patchy growth of the monomer.

There is a slight shoulder on the *p*LiMA C1s spectrum (Figure 3.22a, bottom). Literature reports by Lecayon *et al.* detect a splitting of the C 1s signal due to a grafted M-C bond on electrografted films < 5nm, though the reported peak was located at 283.8 eV, before the alkane peak at 285.0 eV. The peak area of II, as compared to peak I, is never consistent between samples, suggesting that the signal is due to a surface impurity. The affinity of *p*LiMA for DMF is unknown, and the reduced temperature for drying may not completely remove all the DMF from the very thin polymer. The binding energy for peak II, 285.5 eV, is similar to the position of N-CH₃ signal in DMF reported by NIST, 285.7 eV. When Pt electrodes modified with *p*LiMA are dried at 80°C, then peak II does not appear in the C 1s HRES spectrum. The presence of DMF in the XPS HRES scan of *p*GMA and *p*GMA-*co*-*p*LiMA is never detected. The spectral differences may be due to a lower *p*GMA-DMF affinity, or lack of solvent within the detection limit of the spectrometer (10-15 nm).

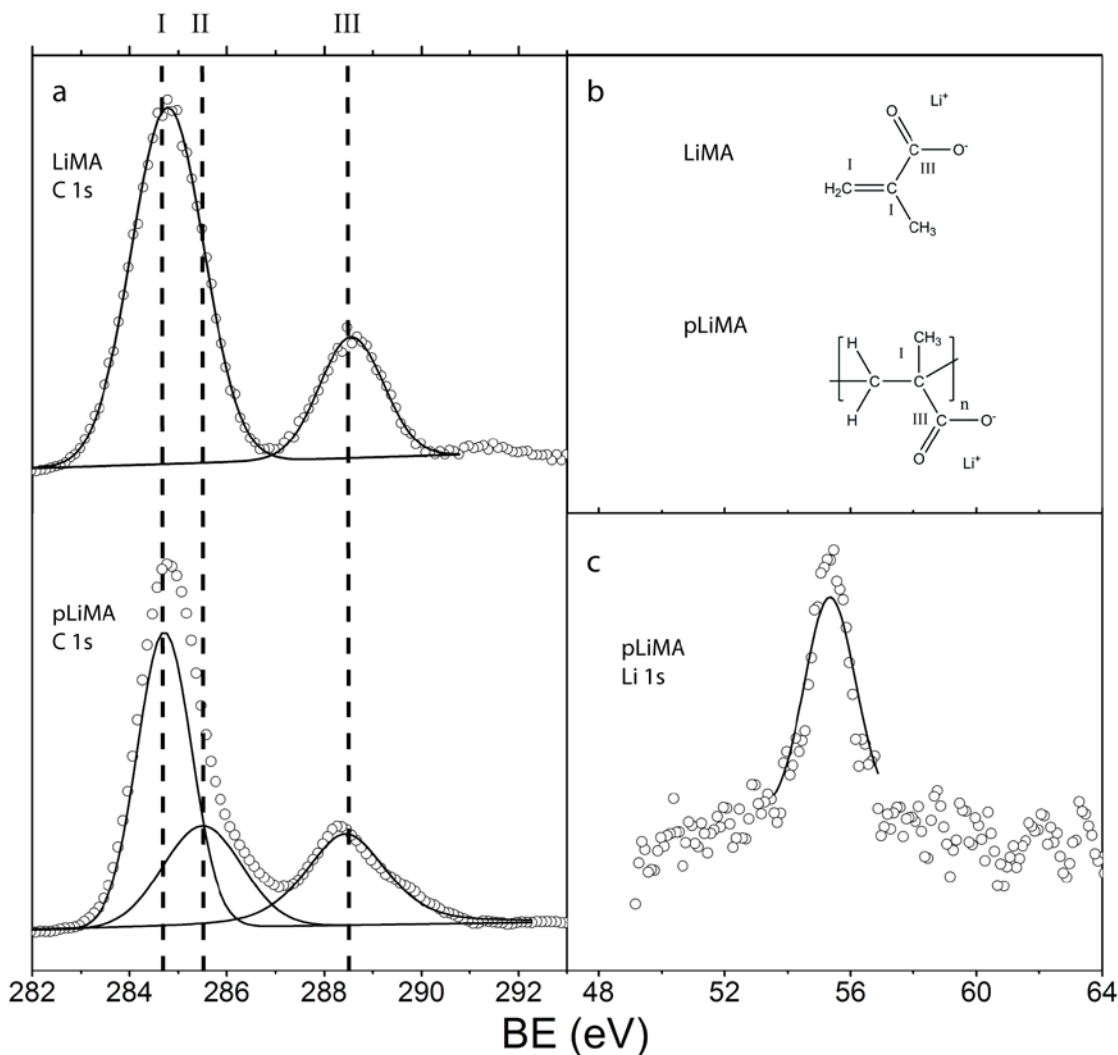


Figure 3.22. a) XPS HRES spectra of LiMA (top) and *p*LiMA (bottom) C1s region. b) structures of the monomer and polymer, indicating the different types of carbons that cause the splitting of the C1s signal. c) XPS HRES spectrum of the Li 1s region of *p*LiMA.

It must be noted here that spectra are usually shifted so that the alkane peaks is centered at 287.4 eV. Insulators are notorious for causing large shifts in XPS spectra. There was often no, or very little, spectral shifting for *p*LiMA; thus, the retention of static charge is very low. The *p*LiMA on the surface of Pt and Cu₂Sb effectively shuttles electrons away from the electrode surface.

Table 3.4. Quantitative results obtained from XPS HRES scans of LiMA and pLiMA. C:C and C:Li ratios are determined by curve-fit analysis.

Sample	C : C Atomic ratio	C : Li
LiMA	I : III 2.1(2) : 1	4.1 : 1
pLiMA	(I + II) : III 2.3(2) : 1	4.3 : 1

The XPS HRES scan of the C 1s region of *pGMA* (top) and *pGMA-co-pLiMA* (bottom) is shown in Figure 3.23a. The electropolymerization of *pGMA* results in a C 1s spectra that can be fit to three peaks: 1) peak I is due to carbons in an alkane environment (vide supra), 2) peak II is due to carbons in a -CH₂-O environment and 3) peak III is due to carbons in a -O-C=O carbonyl environment. Analysis of the peak areas from curve-fit analysis show that the carbons are in a 3:3:1 ratio (I:II:III), consistent with the structure of *pGMA* (Figure 3.23b). The chemical environment of the -CH₂-O carbon, peak II at 286.3 eV, is unique to *pGMA*.

Some evidence for co-polymerization was found by comparing the C 1s region for *pGMA* to *pGMA-co-pLiMA* (Figure 3.23a - bottom). A peak located at 286.3 eV in the C 1s region of the co-polymer is evidence of GMA intercalation into the electropolymerized layer. A comparison of the C 1s peak positions determined by curve fit analysis over multiple samples is shown in Table 3.5. The data clearly shows the presence of *pGMA* and an interesting splitting of the carbonyl peak. The splitting is a small indication of copolymerization but not direct evidence of *pLiMA*. The presence of a signal in the Li 1s region provides evidence for the inclusion of LiMA (Figure 3.23c).

The presence of mobile Li-ions in the polymer is a big step towards a successful polymer electrolyte on Cu_2Sb , and the mobility will be discussed during the solid-state impedance results.

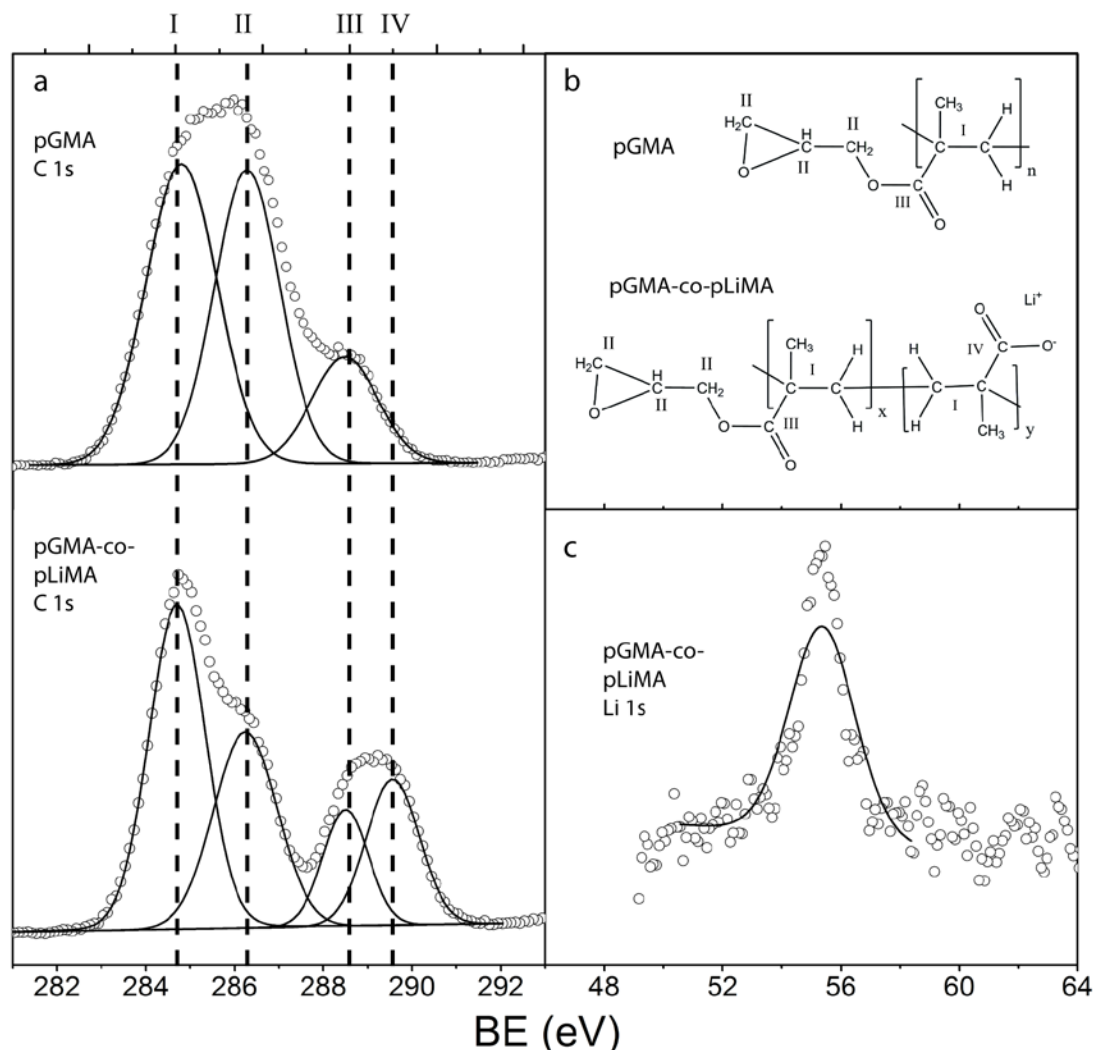


Figure 3.23. a) XPS HRES spectra of *pGMA* (top) and *pGMA-co-pLiMA* (bottom) C1s region. b) Structures of the polymers, indicating the different types of carbons that cause the splitting of the C1s signal. c) XPS HRES spectrum of the Li 1s region of *pLiMA*.

The splitting of the $-\text{O}-\text{C}=\text{O}$ environment is a consistent result that deserves some discussion. XPS analysis of heterogeneous solid surfaces has been used to determine the elemental make-up of insulating and conducting domains. The XPS HRES spectra of

insulating materials, such as *p*GMA and *p*GMA-*co*-*p*LiMA, charge during data acquisition. As a result, good spectra require sufficient grounding and a reliable shifting procedure. Along with use of an internal static-charge neutralizer, precautions were taken to ground the metal electrode and the surface of the polymer films. Some steady-state charging was unavoidable, and all polymer films were shifted so that the alkane signal was fitted to 284.7 eV. Our hypothesis is that the conductivity of *p*LiMA causes the splitting of the carbonyl peak. Microscopic conducting domains on an insulator remain at the spectrometer potential, while the insulating domain reaches a steady state charge. Consequently, an element in the same chemical phase, such as a -O-C=O carbon, will display one peak for each phase. The supply of low energy electrons that stabilize the surface charge, will move the spectral peaks of insulating region relative to the conducting region. The splitting of the carbonyl peak into III and IV is due to the difference in conductivity of the separate phases of the polymer.

Table 3.5. Peak positions for the splitting of the C 1s spectra.

Sample	Peak Position (eV)			
	I	II	III	IV
<i>p</i> LiMA	284.7	285.5 ± 0.2	288.4 ± 0.2	----
<i>p</i> GMA	284.7	286.3 ± 0.2	288.4 ± 0.1	----
<i>p</i> GMA- <i>co</i> - <i>p</i> LiMA	284.7	286.3 ± 0.3	288.4 ± 0.3	289.5 ± 0.2

Quantitative analysis of surfaces with XPS is popular technique. Curve-fitting analysis of peak areas, coupled with unique spectrometer sensitivity factors, affords comparisons of peak areas between different elements and/or elements in different chemical environments. The effect of salt-concentration in polymer electrolytes is studied extensively in the literature.^{35,44-45} Specifically, the σ_{ion} of a polymer increases as the salt-content increases. The rise in σ_{ion} limits at an optimum concentration for the salt.

After the concentration has been exceeded, the ionic conductivity of the polymer decreases drastically. There are two reported reasons: 1) ion-coupling between Li-ion and the high concentration of anions and 2) changes to the T_g of the polymer with increasing salt-concentration. Therefore, controlling the concentration of *pLiMA* in the copolymer is an important step to increasing the ionic conductivity of the polymer.

An initial attempt to vary the amount of *pLiMA* is performed by altering the concentration of the monomer in the deposition solution (Figure 3.24). The concentration of GMA was held constant at 1.5 M while the concentration of LiMA was varied. The

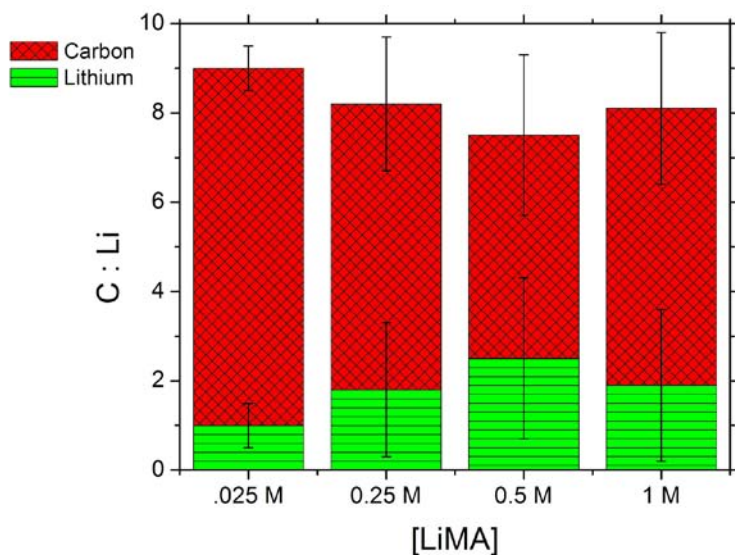


Figure 3.24. C:Li atomic ratios for *pGMA-co-pLiMA* as determined by curve-fit analysis of XPS HRES scans. The concentration of GMA was 1.5 M for all experiments. Error bars are determined from the standard deviation (1σ) of 6 electrodes.

peak areas from the XPS HRES scans of the Li 1s and the C 1s regions are analyzed to find atomic ratios, C : Li, for the polymer films. If the *pLiMA* and *pGMA* are deposited in equal concentrations, then the C : Li ratio would be 9 : 1. The results from changing the concentration of LiMA show no clear trend for the amount of Li-ions detected in the

polymer. Inhomogeneities in the surface concentration of Li-ions and error in determining atomic percents of heterogeneous (conducting vs insulating) surfaces are possible explanations for the large standard deviation. Chain re-arrangement due to high-surface-tension has been reported for XPS analysis of amine functionalities on polydimethylsiloxane films³⁹.

The successful electro-copolymerization of a neutral monomer with an anionic monomer has been shown to produce polymeric layers with solid-state ionic conductivity^{31-33,39}. The inclusion of both monomers into the polymeric layer has been proven through XPS analysis. To determine the polymer's capability to transfer ions, the shape of the solid-state impedance response will tell us if the copolymer is an electrical conductor, electrical insulator or a polymer electrolyte.

3.15 Solid-state electrical measurements of *p*GMA-*co*-*p*LiMA

The inclusion of ions into a film does not necessarily result in the conduction of ions between electrodes. Electro-synthesized copolymers reported by Rolison *et al.*³⁹ were electrically tested in the solid-state. The contact area for metal eutectic testing was 0.5-2.5 mm², allowing for multiple measurements at different locations on the same electrode. They reported only seeing ionic conductivity in 43 % of sample spots on the electrode surface. Therefore, over 50 % of the electrode resulted in a dielectric response. Maier *et al.*⁴⁶ has shown nanoscale regions of mixed ionic conductivity on the surface of drop-cast PEO:LiA (A:PF₆, ClO₄ and CF₃-SO₃) using a conducting probe AFM. Their results prove that the regions of low structural order (amorphous) of a polymer electrolyte are regions of high ionic conductivity. Our measurements with a Ga-In eutectic were

made with a 4.2 mm^2 surface and only one measurement was taken per electrode. The only response seen for 100 % of the electrodes is an electrically insulating layer. However, there could be regions of ionic conductivity that are overshadowed by larger insulating regions. Heterogeneity has been implied by XPS, optical microscopy (Figure 3.13), and literature reports of electro-copolymerization. We conclude that *pGMA-co-pLiMA* has an abundance of low-conductivity, structurally ordered regions at room temperature that impede the flow of ions.

3.16 Temperature-dependent solid-state electrical measurements

To test the influence of temperature on the ionic conductivity of *pGMA-co-pLiMA*, SS Imp measurements were taken on a Pt electrode heated on top of a sand-bath (experimental). A series of Nyquist plots (Figure 3.25) illustrates the change in ionic conductivity of the polymer layer with temperature. The ionic conductivity of the copolymer is given as a function of the sand-bath temperature. The value is assuming a 150 nm thick layer and R_{poly} values are determined by fitting the data to the given model. The expression of ionic conductivity at elevated temperatures is not uncommon. PEO:LiA polymers, a common polymer electrolyte in Li-ion polymer batteries, require elevated temperatures for operational use. The influence of T_g on electropolymerized layers is recognized; a low T_g is essential to electro-depositing a polymer with superior ionic conductivity.

The glass transition temperature, T_g , of a polymer is the temperature where the polymer transforms from a hard, glass-like state to a flexible, rubber-like state. Broadly, polymers above the T_g are more amorphous than polymers below the transition

temperature. Vijayanand *et al.*⁴⁷ report that the T_g values for free-radical polymerization of *p*GMA with poly-4-cyanophenyl acrylate (*p*CPA) are 74 °C and 25 °C, respectively. The high glass transition temperature for *p*GMA means that the polymer is not very amorphous at room temperature, though our polymerization method may impose structural differences on the electro-synthesized polymers.

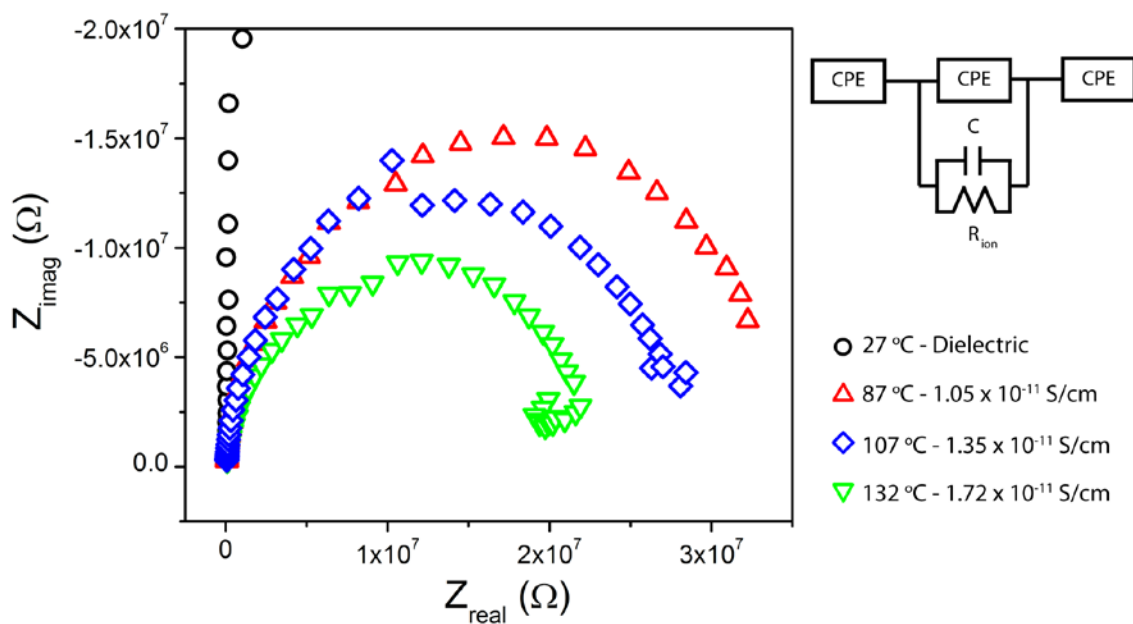


Figure 3.25. A series of Nyquist plots for a heated Cu_2Sb electrode (left). From fitting the impedic response to the model (right, top), values for the ionic conductivity at the different temperatures reported (right, bottom). Values assume a 150 nm thick polymer.

3.17 Discussion and Conclusions

The glass transition temperature of *p*LiMA has not been reported in the literature, but ionmers typically have higher T_g values than neutral polymers³². Crystallization of the copolymer film is detrimental to the ionic conductivity; however, high T_g of *p*GMA can be lowered through copolymerization. Vijayanand *et al.* successfully blended 45 mol%

*p*CPA with *p*GMA to lower the T_g of the polymer blend to 31 °C. Finding a new monomer, either as a replacement for GMA or as an addition to the polymer blend, is an immediate avenue of research. Possible candidates for future monomers for copolymerization can be screened with T_g , and the synthetic library for monomers is vast.

Reductive electropolymerization is a route to conformally coat the surface of Cu_2Sb with *p*GMA, *p*GMA:LiClO₄ and *p*GMA-*co*-*p*LiMA. Solid-state ionic conductivity is evidenced in a salt-doped polymer layer (*p*GMA:LiClO₄) at room temperature and in a copolymer (*p*GMA-*co*-*p*LiMA) at elevated temperatures. The presence of copolymers is illustrated with XPS analysis of LiMA, *p*LiMA, *p*GMA and *p*GMA-*co*-*p*LiMA. Increasing the temperature of *p*GMA-*co*-*p*LiMA induced ionic conductivity, therefore, the presence of ion-conducting, amorphous regions are still necessary to transfer Li-ions in polymers that are < 200 nm thick.

The conformal application of nanometer thick, electrically resistive solid layers that conduct Li-ions is a difficult task. However, we have set up methods to determine surface area and thickness to determine quantitative values for ionic conductivity. We have also formulated solution (redox-probe) and solid-state (AFM) procedures that can provide evidence for nanoscale coverage. Future experiments on new systems can utilize these methods towards finding and optimizing a polymer electrolyte for 3D Li-ion batteries.

3.18 References

- (1) Surridge, N. A.; Keene, F. R.; White, B. A.; Facci, J. S.; Silver, M.; Murray, R. W. *Inorganic Chemistry* **1990**, *29*, 4950.
- (2) Fenton, D. E.; Parker, J. M.; Wright, P. V. *Polymer* **1973**, *14*, 589.
- (3) Florjanczyk, Z.; Marcinek, M.; Wieczorek, W.; Langwald, N. *Polish Journal of Chemistry* **2004**, *78*, 1279.
- (4) Lapienis, G. *Progress in Polymer Science* **2009**, *34*, 852.
- (5) Quartarone, E.; Mustarelli, P.; Magistris, A. *Solid State Ionics* **1998**, *110*, 1.
- (6) Sirisopanaporn, C.; Fernicola, A.; Scrosati, B. *Journal of Power Sources* **2009**, *186*, 490.
- (7) Syzdek, J.; Armand, M.; Gizowska, M.; Marcinek, M.; Sasim, E.; Szafran, M.; Wieczorek, W. *Journal of Power Sources* **2009**, *194*, 66.
- (8) Xie, H. Q.; Xie, D. *Progress in Polymer Science* **1999**, *24*, 275.
- (9) Zhu, C. B.; Cheng, H.; Yang, Y. *Journal of the Electrochemical Society* **2008**, *155*, A569.
- (10) Hassoun, J.; Panero, S.; Reale, P.; Scrosati, B. *Advanced Materials* **2009**, *21*, 4807.
- (11) Funt, B. L.; Gray, D. G. *Journal of the Electrochemical Society* **1970**, *117*, 1020.
- (12) Funt, B. L.; Blain, T. J. *Journal of Polymer Science Part a-1-Polymer Chemistry* **1971**, *9*, 115.
- (13) Collins, G. L.; Thomas, N. W. *Journal of Polymer Science Part C-Polymer Letters* **1975**, *13*, 73.
- (14) Deniau, G.; Lecayon, G.; Viel, P.; Hennico, G.; Delhalle, J. *Langmuir* **1992**, *8*, 267.
- (15) Deniau, G.; Viel, P.; Lecayon, G.; Delhalle, J. *Surface and Interface Analysis* **1992**, *18*, 443.
- (16) Tanguy, J.; Viel, P.; Deniau, G.; Lecayon, G. *Electrochim Acta* **1993**, *38*, 1501.
- (17) Bureau, C.; Defranceschi, M.; Delhalle, J.; Deniau, G.; Tanguy, J.; Lecayon, G. *Surface Science* **1994**, *311*, 349.
- (18) Leonardstibbe, E.; Lecayon, G.; Deniau, G.; Viel, P.; Defranceschi, M.; Legeay, G.; Delhalle, J. *Journal of Polymer Science Part a-Polymer Chemistry* **1994**, *32*, 1551.
- (19) Tanguy, J.; Deniau, G.; Auge, C.; Zalczer, G.; Lecayon, G. *Journal of Electroanalytical Chemistry* **1994**, *377*, 115.
- (20) Bureau, C.; Deniau, G.; Valin, F.; Guittet, M. J.; Lecayon, G.; Delhalle, J. *Surface Science* **1996**, *355*, 177.
- (21) Bureau, C.; Deniau, G.; Viel, P.; Lecayon, G.; Delhalle, J. *Journal of Adhesion* **1996**, *58*, 101.
- (22) Tanguy, J.; Deniau, G.; Zalczer, G.; Lecayon, G. *Journal of Electroanalytical Chemistry* **1996**, *417*, 175.
- (23) Deniau, G.; Thome, T.; Gaudin, D.; Bureau, C.; Lecayon, G. *Journal of Electroanalytical Chemistry* **1998**, *451*, 145.
- (24) Lebrun, C.; Deniau, G.; Viel, P.; Lecayon, G. *Surface & Coatings Technology* **1998**, *100*, 474.
- (25) Viel, P.; Bureau, C.; Deniau, G.; Zalczer, G.; Lecayon, G. *Journal of Electroanalytical Chemistry* **1999**, *470*, 14.
- (26) Deniau, G.; Viel, P.; Bureau, C.; Zalczer, G.; Lixon, P.; Palacin, S. *Journal of Electroanalytical Chemistry* **2001**, *505*, 33.
- (27) Defever, T.; Deniau, G.; Palacin, S.; Goux-capes, L.; Barrau, S.; Mayne-l'hermite, M.; Bourgoin, J. P. *Journal of Electroanalytical Chemistry* **2006**, *589*, 46.
- (28) Deniau, G.; Charlier, J.; Alvado, B.; Palacin, S.; Aplincourt, P.; Bauvais, C. *Journal of Electroanalytical Chemistry* **2006**, *586*, 62.
- (29) Palacin, S.; Bureau, C.; Charlier, J.; Deniau, G.; Mouanda, B.; Viel, P. *Chemphyschem* **2004**, *5*, 1469.
- (30) Charlier, J.; Ameer, S.; Bourgoin, J. P.; Bureau, C.; Palacin, S. *Advanced Functional Materials* **2004**, *14*, 125.
- (31) de Araujo, C. C.; Kreuer, K. D.; Schuster, M.; Portale, G.; Mendil-Jakani, H.; Gebel, G.; Maier, J. *Physical Chemistry Chemical Physics* **2009**, *11*, 3305.

- (32) Dou, S. C.; Zhang, S. H.; Klein, R. J.; Runt, J.; Colby, R. H. *Chemistry of Materials* **2006**, *18*, 4288.
- (33) Lefebvre, M.; Qi, Z. G.; Rana, D.; Pickup, P. G. *Chemistry of Materials* **1999**, *11*, 262.
- (34) Armand, M.; Tarascon, J. M. *Nature* **2008**, *451*, 652.
- (35) Ahmad, S. *Ionics* **2009**, *15*, 309.
- (36) Kang, W. C.; Park, H. G.; Kim, K. C.; Ryu, S. W. *Electrochim Acta* **2009**, *54*, 4540.
- (37) Mosby, J. M.; Prieto, A. L. *Journal of the American Chemical Society* **2008**, *130*, 10656.
- (38) Rampi, M. A.; Whitesides, G. M. *Abstracts of Papers of the American Chemical Society* **1998**, *216*, 166.
- (39) Rhodes, C. P.; Long, J. W.; Rolison, D. R. *Electrochemical and Solid State Letters* **2005**, *8*, A579.
- (40) Long, J. W.; Dunn, B.; Rolison, D. R.; White, H. S. *Chemical Reviews* **2004**, *104*, 4463.
- (41) Haick, H.; Cahen, D. *Accounts of Chemical Research* **2008**, *41*, 359.
- (42) Haick, H.; Cahen, D. *Progress in Surface Science* **2008**, *83*, 217.
- (43) White, R. J.; White, H. S. *Langmuir* **2008**, *24*, 2850.
- (44) Niedzicki, L.; Kasprzyk, M.; Kuziak, K.; Zukowska, G. Z.; Armand, M.; Bukowska, M.; Marcinek, M.; Szczecinski, P.; Wieczorek, W. *Journal of Power Sources* **2009**, *192*, 612.
- (45) Tarascon, J. M.; Armand, M. *Nature* **2001**, *414*, 359.
- (46) Jamnik, J.; Maier, J. *Physical Chemistry Chemical Physics* **2003**, *5*, 5215.
- (47) Vijayanand, P. S.; Kato, S.; Satokawa, S.; Kojima, T. *Journal of Applied Polymer Science* **2008**, *108*, 1523.

Chapter 4

The decomposition of Li-ion battery liquid electrolytes on Cu₂Sb: SEI formation as a route to a solid electrolyte

Timothy S. Arthur, Matthew T. Rawls and Amy L Prieto

Timothy Arthur designed and performed all the experiments in this chapter. Matthew Rawls assembled electrochemical cells and repeated all experiments to ensure the accuracy of the data. Mathew Rawls also collected the data in Figure 4.1.

This dissertation chapter is adapted from a manuscript in preparation to be submitted to *Journal of Power Sources*.

4.1 Abstract

The effectiveness of the solid-electrolyte interface (SEI) as a solid electrolyte in Li-ion batteries was investigated. The addition of vinylene carbonate to a typical organic electrolyte solution was used as a medium to grow the SEI on an intermetallic anode material, copper antimonide (Cu_2Sb), by two methods; a galvanostatic/potentiostatic method and a galvanostatic cycling method. The dielectric capabilities of the SEI were tested with solid-state impedance; a thin insulating layer was only efficiently produced when Cu_2Sb was cycled between 1.8 V and 0.9 V vs Li/Li^+ . In addition, the morphology of the SEI was analyzed with scanning-electron microscopy. Peak-fitting analysis of the high-resolution X-ray photoelectron spectra found that the inclusion of lithium carbonate, and/or other organo-lithium salts, into the SEI upon galvanostatic cycling is vital to the dielectric capabilities of the solid electrolyte.

4.2 Introduction

Lithium-ion (Li-ion) batteries continue to flourish as the standard for powering high energy devices such as portable electronics, and are now finding a place in the automotive industry. The successful transition to transport applications will require high-power along with improved safety, increased cycle-life, and decreased cost¹. The radical increase in power and energy density required for widespread automotive application of Li-ion batteries may derive from 3d architectures comprised of nanostructured active materials. These nanoarchitectures will require a highly uniform and thin electrolyte/separator coating for optimal performance. These requirements suggest a move from gel and liquid electrolytes in current use to solid state separator coatings.

The main disadvantage to using a solid in place of a liquid electrolyte is the low ionic conductivity of solid materials²⁻⁴. There are two general avenues of research that focus on solving this problem. The first one involves synthetic approaches to chemically modifying solid layers with poor ion-transport properties through gelation techniques⁵⁻⁶, the development of novel solid lithium salts⁷⁻⁸, co-polymerization⁹⁻¹⁰ and/or adding ceramic fillers¹¹⁻¹². The second approach is to lower the ionic resistance with novel methods for applying the solid-electrolyte layer. Projects include the synthesis of multi-block polymer architectures that provide ion-conducting channels^{9,13-14} and the application of extremely thin layers (< 20 nm) through self-limiting electropolymerization^{10,15-17} and CVD¹⁸⁻¹⁹ techniques. However, a solid-state device utilizing high-surface area nanoarchitectures requires a uniform modification of a three-dimensional surface⁴, which precludes many of the options stated above.

The electrochemical deposition of organic materials on electrodes offers many advantages, such as uniform modification of non-linear nanostructures, nanoscale control of thickness and the deposition of a dielectric layer. Rolison *et al.*^{10,15-16} has investigated the anodic electropolymerization of neutral and charged organic monomers on conducting aerogel surfaces. Long *et al.*¹⁷ successfully used this soft-chemistry technique to build an ultracapacitor with excellent charge densities. Palacin *et al.*²⁰⁻²¹ modified nanotrenches using a reductive electrografting of acrylate monomers. Gonbeau *et al.*²² proposed a radical electropolymerization of vinylene carbonate (VC) on the surface of graphite as the reaction that protects the liquid electrolyte from further decomposition. To conformally coat the anode material with a Li-ion conducting, solid layer that maintains physical stability and dielectric capabilities over the large potential

range of a Li-ion battery (3.5-4.5 V) is a key step in fabricating an all solid-state Li-ion battery. This is a pivotal point in the ground-up fabrication of nanostructured devices; an approach pursued by our group.

Organic liquid electrolytes used in state-of-art lithium-ion batteries decompose under the very reducing and oxidizing conditions of battery operation; the products comprise what is termed the solid-electrolyte interface (SEI) layer. There is much discussion in the literature on the use of SEI stabilizing organic additives such as 2-cyanofuran²³, vinylene carbonate²² and succinic anhydride²⁴ that have improved safety and decreased capacity-loss over long cycle numbers²⁵⁻²⁷. However, only one report²⁸ exists where the SEI is utilized as a solid electrolyte.

It is known that SEI layer forms on most anodes during the first ten to fifteen charge/discharge cycles of the material¹. This allows a solid-state electrolyte based on the formation of the SEI layers to be applied to a variety of anode materials. However, the attributes of the SEI may be different when formed on alloying electrodes^{24,29-31} (such as graphite, silicon and tin-carbon composites for example) and intermetallic electrodes (such as Cu₂Sb). Part of our research is to investigate this possibility. There is abundant research investigating the nature of the electrode/electrolyte interface on anode and cathode materials for lithium ion batteries. Experiments have focused on the effect of additives on SEI formation with the goal of improving liquid cell battery performance²⁷. Our work differs as the goal is to fabricate a solid electrolyte layer with the SEI, not to improve capabilities in a solution-based battery cell. This means the SEI must coat electrodes with different morphologies and surface areas allowing the cathode material to be intimately integrated with the anode material. The goal of our work presented in this

dissertation chapter is (1) to physically characterize the SEI layer formed on Cu_2Sb from a typical organic electrolyte solution with X-ray photoelectron spectroscopy and scanning-electron microscopy, and (2) to ascertain the dielectric capabilities of the SEI with solid-state impedance.

4.3 Experimental

Chemicals: Dimethyl carbonate (DMC, anhydrous, $\geq 99\%$), diethyl carbonate (DEC, anhydrous, $\geq 99\%$), vinylene carbonate (VC, 99.9%), lithium perchlorate (LiClO_4 , battery grade, 99.999%), lithium carbonate (Li_2CO_3 , $\sim 99\%$) and gallium-indium eutectic (Ga-In) were all purchased from Aldrich, kept at room temperature in an Ar-filled glovebox and used without further purification. Ethylene carbonate (EC, anhydrous, 99% - Aldrich) was recrystallized from ethanol, dried and kept in the Ar-filled glovebox. *polyVC* was synthesized using a literature procedure²².

Anode preparation: Copper antimonide (Cu_2Sb) was electrodeposited on mechanically polished Cu foil (99.999% - Aldrich) using our previously described method³². All Cu_2Sb electrodes were dipped in 5 vol % HNO_3 , washed well with water (1 Ω) and isopropanol, dried under a N_2 flow and immediately brought into the Ar-filled glovebox to decrease the chance of native-oxide growth. Cu_2Sb electrodes were then cut into 0.64 cm diameter circles for cell assembly.

Electrochemical half-cell preparation: All symmetrical Swage-lok cells were assembled in an Ar-filled glovebox. Cu_2Sb circle electrodes were sealed against a 0.32 cm diameter circular cell holder filled with a 1M LiClO_4 1 : 1 : 1 EC/DEC/DMC (vol) solution (prepared in the Ar-filled glovebox). A $\text{Li}_{(m)}$ counter electrode was sealed on the

opposite end and the air-tight assembly and the cell was removed from the Ar-filled glovebox for SEI growth. All voltages stated in this work are referenced to Li/Li⁺.

SEI preparation: Figure 4.1 is the charge curve for the galvanostatic reduction of Cu₂Sb in the electrochemical half-cell. From the curve, potentials were chosen to border regions for SEI growth. The approximate open-circuit potential (OCP) of the described half-cell is 3.0 V (point A). Points B-D (2.2 V, 2.0 V and 1.8 V respectively) are potentials before the lithiation of Cu₂Sb. At approximately 0.9 V (point E) the reduction of Cu₂Sb begins and the anode material begins to charge with complete lithiation of Cu₂Sb at 0.05 V (point F) The discussion of the potential choices is presented *vide infra*.

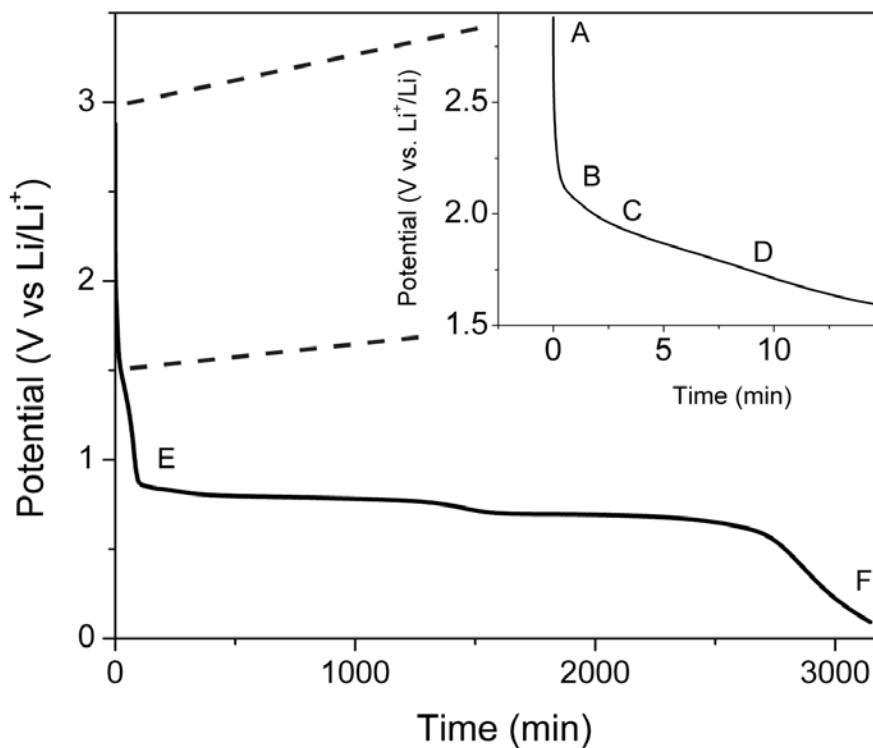


Figure 4.1. Potential vs time curve for a Cu₂Sb electrochemical half-cell galvanostatically charged at 10 $\mu\text{A cm}^{-2}$ in a 1M LiClO₄ EC/DEC/DMC (1:1:1) electrolyte solution. Added potential points A-D (inset) and points E, F are labeled.

1. *Method A*: Galvanostatic/Potentiostatic deposition. All SEI growth experiments were performed on a Maccor Model 4200 Battery Cycler. The two-electrode electrochemical cells were galvanostatically charged (Cu_2Sb reduced) from the open-circuit potential (point A - ~ 3.0 V) at a $10 \mu\text{A cm}^{-2}$ current density. Once the cell reached a pre-determined voltage (points B-E), the voltage was held until the current reached a $1 \mu\text{A cm}^{-2}$ current density. Point F was not selected as a possible potential limit since a goal of the research is to form a solid electrolyte on an uncharged anode material. Cells were then disassembled by removing the $\text{Li}_{(m)}$ and electrolyte solution, but keeping the Cu_2Sb sealed in one-half of the Swage-lok cell. All Cu_2Sb electrodes were washed thoroughly with DMC and dried at 40°C for ~ 15 hs.
2. *Method B*: Galvanostatic cycling deposition. Similar to Method A, the half-cells were galvanostatically reduced at a $10 \mu\text{A cm}^{-2}$ current density until a voltage limit was reached. Then the current polarity was switched so that the Cu_2Sb is oxidized at the same rate to a higher, predetermined potential. At that point, the cells were cycled galvanostatically between the potential limits for a number of cycles. One cycle begins with the reduction at the Cu_2Sb surface and ends after the oxidation at the Cu_2Sb surface. Method B is subdivided into 3 potential ranges: (i) The high potential range (HPR) is between 3.0 V and 1.8 V (vs Li/Li^+), (ii) the medium potential range (MPR) is between 1.8 V and 0.9 V (vs Li/Li^+), (iii) and the low potential range is between 0.9 V and 0.05 V (vs Li/Li^+). All electrodes were washed and dried as in Method A.

Solid-state electrical measurements: Ga-In eutectic was used to contact the SEI surface. The liquid metal was placed on top of the SEI directly in the 0.32 cm diameter plastic Swage-lok cell. Tungsten wire, pre-wetted by immersion in Ga-In for 30 sec, was used to contact the eutectic on the surface of the electrode. Two-electrode impedance measurements with the Ga-In as the working electrode and the Cu₂Sb as the counter/reference electrode were taken in a N₂-filled glovebox on a CHI 660c potentiostat/galvanostat. The impedic responses were collected in the 100 kHz – 0.1 Hz range with a 0 V DC bias and a 100 mV AC amplitude. This method is hereafter referred to as SS Imp.

Physical characterization - X-ray photoelectron spectroscopy (XPS) (Phi 6500) was used to characterize the surface of Cu₂Sb. Measurements were performed with a 5800 series Multi-Technique ESCA system and analyzed using Multipak software. An Al monochromatic source operating at 350.0 W was scanned with a pass energy of 58.7 eV in intervals of 0.125 eV step⁻¹ over the range indicated on the spectra. All XPS spectra were shifted so that the adventitious C1s peak was located at 284.7 eV. During curve-fit analysis of XPS HRES spectra, all fitted-peak had $\chi^2 \leq 1$ values. Peak positions and atomic ratios are reported from peak-fitting of the data. Scanning Electron Microscopy (SEM) micrographs were taken using a JEOL JSM 6500F.

4.4 Results

Method A – SS Imp

An SEI must be an electrically insulating layer to be used as a solid electrolyte in Li-ion batteries. Galvanostatic charging until ending potentials B-E result in an electrically conducting layer whose resistivity (2Ω - 75Ω) is the sum of the contact resistances between the different interfaces. The SEI is either a conducting or a non-uniform film; the latter allows for direct contact between the Ga-In eutectic and the Cu_2Sb . Point F was not selected as an ending point for Method A since the objective is to make an SEI on Cu_2Sb , not on Li_3Sb (the completely charged version of the anode). Since the experimental plan involves the intercalation of an uncharged cathode, we need to keep Cu_2Sb (the uncharged anode) as the substrate. Any conversion to the lithiated versions of the anode will decrease the capacity of the full battery cell. Method A, under our conditions, is insufficient to form an SEI with functional solid-state dielectric properties.

During half-cell battery cycling, the surface of Cu_2Sb is both reduced (during charge) and oxidized (during discharge). The differences in solid-state electrical properties between Method A and Method B (vide infra) encouraged us to determine the molecular composition of each SEI layer. By investigating the compounds that make up the SEI layer during each electrochemical process, we can illustrate which constituents contribute to the solid-state dielectric properties.

Method A – XPS

C 1s peak analysis – XPS is a powerful technique to elucidate the elemental make-up of the SEI^{22,24,30,33}. Figure 4.2a shows high-resolution spectra of the C 1s and Cu 2p (inset) region of a Cu_2Sb electrode reduced to point D. The C 1s spectrum consists of

three peaks. The first peak corresponds to an (-CH₂-) or (-C-C-) environment (284.7 eV). The second peak corresponds to a carbon in a (-C-O) environment (286.3 eV) and the final peak is a carbon in a (O-CO-O) carbonate environment (289.0 eV). The peak positions match well with the C1s spectrum for the reductive decomposition of 1M LiPF₆ in EC/DMC/DEC (2:1:2 by volume) with a few volume percent VC²². Figure 4.2a (inset) illustrates the presence of Cu 2p peaks in the HRES XPS spectrum, indicating that the SEI formed by this method forms a layer that is thinner than the analysis depth of the XPS (for ending potentials B, C and D). If the electrode is charged to point E, the Cu 2p peaks disappear from the spectrum.

Method A – SEM

Figure 4.2b is a SEM micrograph of the surface of a Cu₂Sb electrode reduced to point D. The cubic morphology of the underlying anode (Figure 4.2b – inset) material is visible under a thin organic layer. Charging the anode until ending potentials points B and C are similar. The surface morphology of Cu₂Sb is not visible for the ending potential point E, indicating a thicker SEI layer. With this result, we expected the SS Imp results to reflect a dielectric layer. However, all of the electrodes charged to this potential displayed electrically conducting properties.

Method B – SEI formation

Method A was successful in producing an SEI layer that could be evidenced by XPS and SEM. However, reducing the anode to ending potentials B-E form a conducting layer. From literature results, it is known that an increase in resistance to charge transfer observed in electrochemical impedance spectroscopy occurs as a battery is cycled^{25,29,34-35}. We also detect a change in the electrochemical impedance spectroscopy as the battery

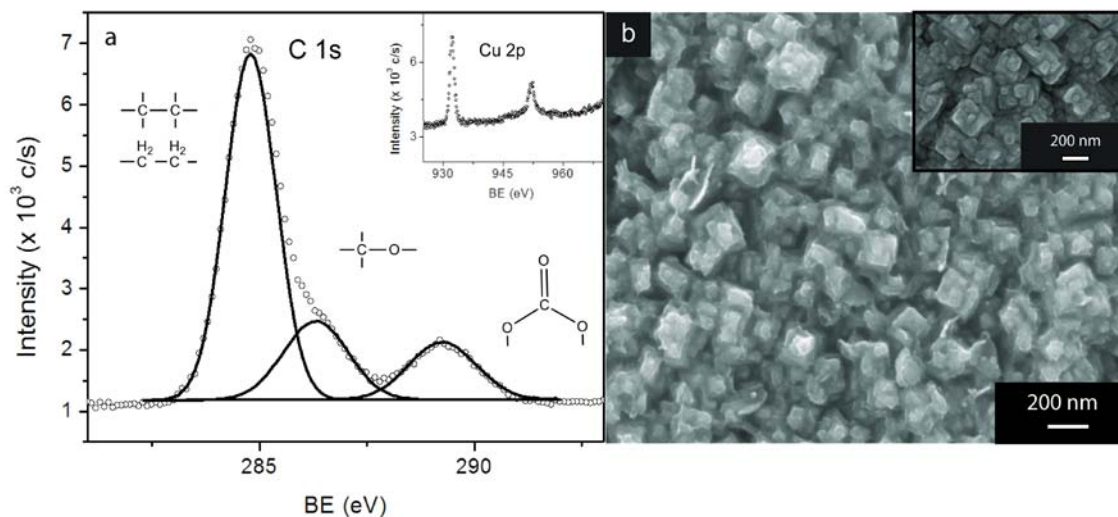


Figure 4.2. (a) XPS HRES C1s and Cu2p (inset) spectra of a Cu_2Sb electrode charged to 1.8 V vs Li/Li^+ . (b) SEM micrographs of the SEI layer formed on the surface of the Cu_2Sb . The cubic morphology of the bare electrode (inset) is still present under the SEI layer.

is cycled (results not shown). The physical and solid-state electronic property changes as an SEI is cycled cathodically and anodically must be better understood.

To investigate the effect of cycling on elemental make-up, morphology and solid-state electronic properties of an SEI, we devised Method B. Research groups have altered the attributes of the SEI by increasing the temperature and/or increasing the concentration of additive^{22,27,29}, for example. Our goal is to efficiently produce an SEI layer with the desired solid-state electrical properties through a galvanostatic cycling method at room temperature.

Method B – SEM

Micrographs of the three potential ranges, high-potential range (HPR), medium potential range (MPR), and low potential range (LPR) are shown in Figure 4.3a, b and c, respectively. The HPR cycling method shows a very thin SEI, but also regions of the Cu_2Sb that had been stripped from the $\text{Cu}_{(m)}$ back-electrode (SI). The cubic morphology

of the Cu_2Sb is visible through the thin HPR and MPR SEI, though the MPR electrodes do not have regions of the anode that had been stripped from the current collector. The morphology of the SEI formed at the LPR is very different than the higher potential ranges. While no polymer could be visibly detected after cycling through the HPR and the MPR, a film was apparent on the surface of the LPR Cu_2Sb electrodes. No Cu_2Sb cubic structures are visible on the surface and there are porous regions on the surface of the SEI. The potential range selected has a strong effect on the thickness of the organic layer.

Method B – SS Imp

The solid state impedance results of the three potential ranges, HPR, MPR and LPR are shown in Figure 4.3d, e and f respectively. All three electrodes were galvanostatically cycled for 20 cycles. For the HPR experiments, Cu_2Sb anodes were cycled for 5, 10, 15, 20, 50 and 100 cycles with no change in the solid-state impedance result. The MPR experiments result in a solid dielectric layer after 20 galvanostatic cycles (5, 10 and 15 cycles result in a conducting layer). The Nyquist plot displays a vertical line extending from $Z_{\text{real}} = 0$ on the horizontal axis indicative of an electrically insulating layer. LPR Nyquist plots show an impedic response indicative of an ionically conducting layer. The hemispherical shape, modeled by a resistor in parallel with a capacitor, was only present in 80% of the samples (20% displayed a dielectric response) and was also present only after 20 galvanostatic cycles (5, 10 and 15 cycles result in a conducting layer).

Method B – XPS

C 1s peak analysis – Figure 4.4 displays distinct differences in the C 1s region between Method A and B. A new peak at 290.5 eV is only present when an oxidizing current is applied to Cu₂Sb. Our initial hypothesis is that the new peak is representative of a Li₂CO₃, or other organo-lithium species (see *Discussion/Conclusions*). A noticeable increase in peak area for the peak at 286.3 eV indicates an increased concentration of (-C-O) environments within the SEI.

O 1s peak analysis – Figure 4.4 shows the presence of two peaks in the O 1s region for the SEI formed by Method A and B. The O 1s region for the chemically synthesized *poly*VC is also shown.

Li 1s and Cl 2p 3/2 peak analysis – The HRES XPS spectra and fitting analysis of the Li 1s spectral peak and Cl 2p 3/2 peak was done to determine atomic ratios. The presence of only one Cl 2p 3/2 was detected; the peak position position (208.7 eV) indicates only perchlorate (ClO₄²⁻) chlorine atoms in the SEI.

Atomic ratios – To determine the relative contributions of Li-ions between the lithium perchlorate and the organo-lithium salts, the Li to Cl ratio was investigated. The average ratio for the SEI obtained in Method A and Method B (20 cycles) is 1.1 : 1 and 4.3 : 1, respectively. Method B shows a significant increase in organo-lithium salts present in the SEI. To elucidate the concentration of Li-ions in the SEI, differences in the carbon to lithium ratio between the three potential ranges of Method B were investigated. The HPR and MPR are 2.9 : 1 and 3.2 : 1, respectively. However, the LPR has a C : Li ratio of 1.2 : 1 (Table 4.1). This result can be explained by remembering that the LPR is cycled between potentials where Cu₂Sb is lithiated and delithiated. There is an extra

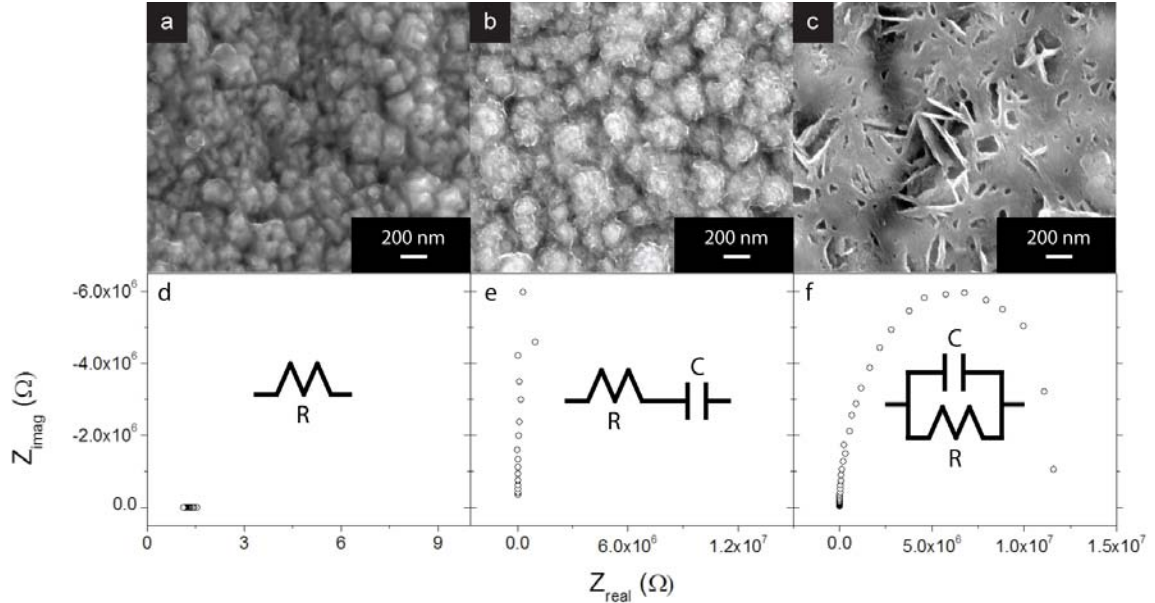


Figure 4.3. SEM micrographs and solid-state impedance Nyquist plots for Cu_2Sb electrodes formed in the HPR (a,d), the MPR (b,e) and the LPR (c,f).

driving force carrying the Li-ions through the SEI layer and more lithium salts are likely to be trapped in the growing SEI layer.

4.5 Discussion and Conclusions

The deposition of SEI on the surface of Cu_2Sb was pursued to evaluate the potential for the SEI to act as a solid electrolyte. VC is an organic additive that reductively deposits at higher potentials than common carbonate-based solutions^{22,27}. VC's inclusion in electrolytes improves capacity retention and increases cycle life for batteries operating with an organic liquid electrolyte. We are primarily focused on the electrochemical reduction of VC which grows a thin and uniform SEI layer. The deposition of VC is a reductive, radical electropolymerization which provides a soft, non-line-of-sight coating technique to modify the surface of two- and three-dimensional electrodes. We

hypothesize that the SEI formed with VC additive will uniformly cover the surface of the electrode.

The galvanostatic/potentiostatic deposition method has provided many insights into the formation of the SEI during the first charge of Cu_2Sb . The XPS C 1s spectra, for all points of charge, were fit to 3 peaks; the peak corresponding to the (O-CO-O) carbon environment is the most interesting. The (O-CO-O) peak obtained from a powder sample of Li_2CO_3 (290.5 eV) and *polyVC* (290.1 eV) were indistinguishable and located at higher binding energies than the carbonate peak found in Method A's SEI. Therefore, an

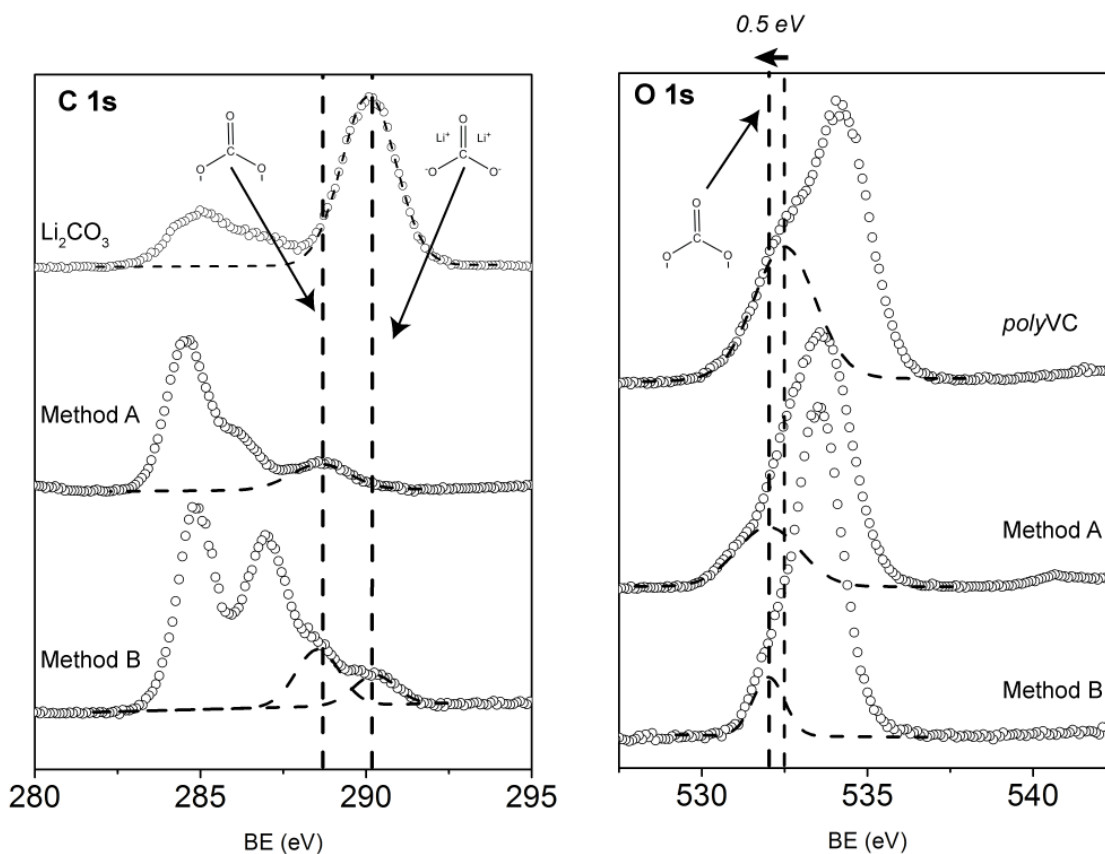


Figure 4.4. XPS C 1s and O 1s HRES spectra of a representative SEI formed with Method A and B. The (O-CO-O) C 1s peak position is compared to Li_2CO_3 . The (O=C) O 1s peak position is compared to *polyVC*. A 0.5 eV shift to lower binding energies is apparent.

analysis of the O 1s region was performed to determine the origin of this (O-CO-O) peak. Li_2CO_3 has three equivalent oxygen atoms, and therefore has a single peak at 532.0 eV (Table 4.1). The O 1s XPS spectra of the SEI formed in Method A and B, both fit to 2 peaks, much like *polyVC* (Figure 4.4). However, a 0.5 eV shift to lower binding energies for the carbonyl oxygen (O=C) is indicative of the electron-rich SEI. Similar shifts in the XPS HRES spectra have been shown in the literature^{10,22}. The shift for the (O-CO-O) carbon in the SEI is approximately double (1.1 eV), but is mirrored by the shift of the (-C-O) carbon (1.0 eV) between *polyVC* and the SEI (Table 4.1). More evidence for the polymerization of VC over the production of lithium salts through degradation is shown by the Li : Cl ratio of 1.1 : 1 obtained in Method A. The majority of the Li-ions present in the SEI are from LiClO_4 ; however, the presence of some lithiated decomposition products cannot be discounted.

The SEM micrographs indicate that the SEI formed by Method A is uniform but thin (< 10 nm) for the ending potentials at or above 1.8 V (points B, C and D). The presence of Cu 2p peaks in the HRES XPS spectrum confirms this hypothesis. For ending point E, there was a thicker, visible film without the presence of Cu 2p peaks in the XPS spectrum for galvanostatic/potentiostatic experiments, an increase in thickness of the SEI at more reductive potentials is not uncommon²²; however, SS Imp results implies a conducting layer, which is a contradictory result to the thick SEI layers we obtained from Method B.

We propose three possible explanations. First, the SEI formed from the methods A and B contain different constituents, as seen from the different C 1s XPS spectra. The low Li to Cl ratio of 1.1 : 1 also indicates that the SEI in Method A is mainly constituted of LiClO_4 trapped in an organic layer, with little contribution from organo-lithium salts.

Table 4.1. Binding energies of C 1s, O 1s, Li 1s and Cl 2p 3/2 and atomic ratios obtained from XPS curve-fit analysis.

Sample	C 1s (eV)	O 1s (eV)	Li 1s (eV)	Cl 2p 3/2 (eV)	C : Li	Li : Cl
Method A	284.7 286.3 289.0	533.5 532.0	55.8	208.7	2.7 : 1	1.1 : 1
Method B	284.7 286.3 289.0 290.5	533.5 532.0	56.0	208.7	2.9 : 1 (HPR) 3.2 : 1 (MPR) 1.2 : 1 (LPR)	4.3 : 1
Li₂CO₃	284.7 286.3 290.5	532.0	55.8	————	0.7 : 1	————
polyVC	284.7 287.3 290.1	534.2 532.5	————	————	————	————

A change in the HRES C1s and an increase in the Li : Cl to 4.3 : 1 upon oxidative cycling of Cu₂Sb suggests inclusion of Li₂CO₃ and other organo-lithium salts into the SEI. This has a profound effect on the electrical conductivity. While the decrease in electron flow may be non-advantageous for capacity retention and cycle-life in wet battery cells, electrical insulation is a vital characteristic of a solid-electrolyte. Second, the ending potential 0.9 V is on the border for reported lithiation potentials of Cu₂Sb. If some lithiation of Cu₂Sb did occur, then one of the products is a very conductive Cu_(m). It is not detected within the first 10 nm (the penetration depth of the XPS) of the SEI, but its presence below that depth cannot be discounted, and neither can the effect on the conductivity of the SEI. To investigate this theory, a pXRD pattern was taken of the Cu₂Sb electrode after SEI formation, and no lithiation products of the anode were

detected. Finally, only microscopic uniformity is observed on the SEM (although, observed over 10-12 different regions). Since the electrode surface area is 0.4 cm^2 , a macroscopic technique for determining uniformity is needed and redox-probe experiments to this end are underway.

The galvanostatic cycling method of forming the SEI was divided into the HPR (points A to D), the MPR (points D to E) and the LPR (points E to F). The XPS analysis identified a new peak in the spectrum upon electrochemical oxidation of the of the Cu_2Sb electrode. The binding energy of the new carbeneous species (290.5 eV) suggested a carbonate (O-CO-O) species. Figure 4.4 shows a shift to higher binding energies (1.5 eV) than the carbonate species observed in the SEI formed by Method A. The electropositivity of the carbon in the CO_3^{2-} anion is greater than the carbonate carbon found in the *polyVC* within the SEI, thus the CO_3^{2-} carbon will bind more tightly to the core 1s electrons. The (O-CO-O) peak position aligns well with Li_2CO_3 , suggesting the presence of the CO_3^{2-} anion in the SEI formed by Method B. As the literature suggests, the HRES C 1s spectrum of lithium methyl carbonate^{22,29-30,33} has also been investigated. We found that the binding energy of the carbonate electrons indistinguishable from Li_2CO_3 and the species cannot be excluded via XPS. The large increase in Li : Cl ratio for Method B also indicates the inclusion of lithiated organic products upon cycling. Future experiments will include detailed ATR-IR experiments to give further insight into the bulk constituents of the SEI on Cu_2Sb and UPS valence band analysis to further study the surface.

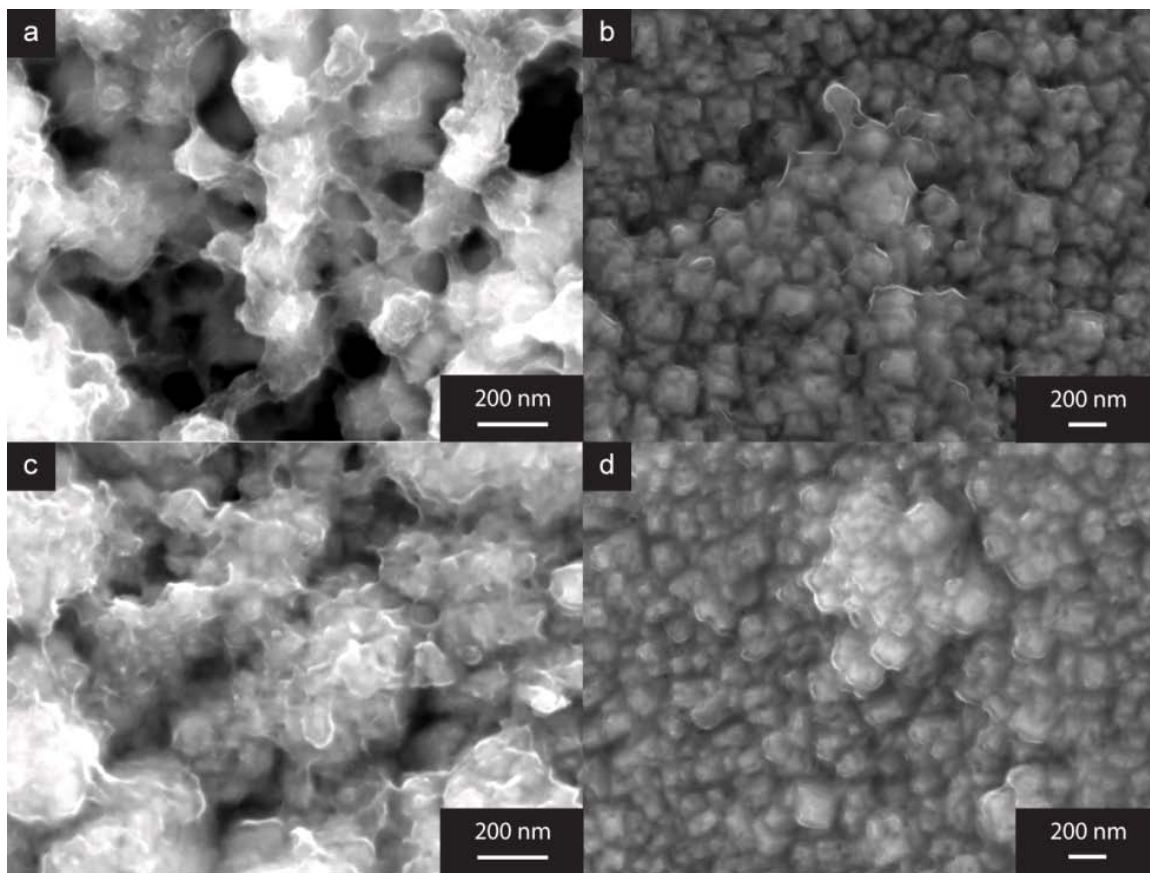


Figure 4.5. SEM micrographs of an SEI grown in the MPR for (a) 5 cycles and (c) 20 cycles. The SEI formed in the HPR for (b) 5 cycles and (d) 50 cycles.

However, lithium methyl carbonate and lithium carbonate are products of the reduction of ethylene carbonate and dimethyl carbonate, respectively. Therefore, we suggest that the lithium salts are formed at the surface of the $\text{Li}_{(m)}$ counter electrode during the oxidation of Cu_2Sb . VC should also protect the surface of $\text{Li}_{(m)}$ from electrolyte decomposition, but there is less monomer present in solution after the initial reductive polymerization on Cu_2Sb . The problem is compounded by the reduction of Li^+ ions at a $\text{Li}_{(m)}$ electrode, which produces more $\text{Li}_{(m)}$ surface sites for electrolyte decomposition. Once formed at the $\text{Li}_{(m)}$ electrode, the lithium salts can diffuse through the wet cell through concentration and electrical gradients. Upon cycling, Li_2CO_3 and

other salts become part of the SEI on Cu_2Sb , and their inclusion is a significant part of the SEI's dielectric properties.

We chose the ending potentials based on previous results. Potential A (3.0 V) is the approximate OCP of the fabricated cell before any electrochemistry. As the cell cycles, the decomposition of the electrolyte will inevitably change the OCV of the two electrode cell. If the electrochemical stripping potential of Cu_2Sb is lowered below 3.0 V during cycling, then dissolution of the Cu_2Sb will occur. This would explain the missing regions of Cu_2Sb on $\text{Cu}_{(\text{m})}$ electrodes that oxidized to 3.0 V. Potentials B-D (2.2 V-1.8 V) are in the range of potentials where the SEI and *poly*VC are formed. Potential E (0.9 V) is the voltage where the reduction of Cu_2Sb begins and F (0.05 V) is the potential after the complete charging of the anode.

Cycling in the HPR, between A and D, never formed a dielectric layer. There was no significant difference in thickness between cycle 5 and 50 (Figure 4.5b and d, respectively). There is a slight observable difference in thickness between cycle 5 and 20 (Figure 4.5a and c, respectively) for the SEI formed in the MPR. The result suggests a mechanical destruction or chemical dissolution of the SEI at higher potentials. To confirm this result, we cycled Cu_2Sb between points A and F for 5, 10, 15 and 20 cycles. The results observed are similar to HPR cycling.

By separating the potential range between 1.8 V and 0.05 V into the MPR and the LPR, we can probe the effect on the SEI of Li-ion intercalation into the anode material. The HRES spectrum of the C 1s region reveals the same carbonaceous constituents in the MPR and LPR SEI, but comparison of the C : Li suggests the presence of more Li^+ ions in the LPR layer. This result explains the ionic conductivity observed in the LPR SS

Imp. The MPR only displays electron insulating properties, not Li^+ ion conductivity. The MPR does have two advantages over the LPR SEI. First, it is a very thin dielectric layer when compared to the thick layer formed at lower potentials (Figure 4.3b and c, respectively). Second, the MPR SEI was electrochemically deposited in 16 h, or 4% of the time of LPR deposition (350 h to 400 h). Therefore, modifying the ionic conductivity of the SEI grown in the MPR is a much more efficient and physically attractive route to forming a solid electrolyte on Cu_2Sb .

Using the MPR growth technique, we are capable of efficiently producing a thin, uniform layer that contains Li^+ ions but acts as a dielectric. There remains a breadth of work to create a solid electrolyte with an SEI. However, uniformity and electrical insulation have been exhibited by the SEI. These are 2 two major obstacles (Chpater 1.2) that have been overcome through the careful electrochemical growth of the SEI. Beyond the aforementioned experiments, our focus will be on inducing ionic conductivity into the SEI. Producing a solid electrolyte on the surface of a three-dimensional nanostructure is a pivotal step towards the fabrication of a solid-state nanowire battery.

4.6 References

- (1) Goodenough, J. B.; Kim, Y. *Chem Mater* **2010**, *22*, 587.
- (2) Armand, M. *Advanced Materials* **1990**, *2*, 278.
- (3) Arora, P.; Zhang, Z. M. *Chemical Reviews* **2004**, *104*, 4419.
- (4) Long, J. W.; Dunn, B.; Rolison, D. R.; White, H. S. *Chemical Reviews* **2004**, *104*, 4463.
- (5) Kang, W. C.; Park, H. G.; Kim, K. C.; Ryu, S. W. *Electrochim Acta* **2009**, *54*, 4540.
- (6) Shanna, J. P.; Sekhon, S. S. *Solid State Ionics* **2007**, *178*, 439.
- (7) Lilley, S. J.; Andreev, Y. G.; Bruce, P. G. *Journal of the American Chemical Society* **2006**, *128*, 12036.
- (8) Du, Y. J. A.; Holzwarth, N. A. W. *J Electrochem Soc* **2007**, *154*, A999.
- (9) Dou, S. C.; Zhang, S. H.; Klein, R. J.; Runt, J.; Colby, R. H. *Chem Mater* **2006**, *18*, 4288.
- (10) Rhodes, C. P.; Long, J. W.; Rolison, D. R. *Electrochem Solid St* **2005**, *8*, A579.
- (11) Zhang, P.; Zhang, H. P.; Li, G. C.; Li, Z. H.; Wu, Y. P. *Electrochemistry Communications* **2008**, *10*, 1052.
- (12) Syzdek, J.; Armand, M.; Gizowska, M.; Marcinek, M.; Sasim, E.; Szafran, M.; Wieczorek, W. *J Power Sources* **2009**, *194*, 66.
- (13) Shimura, H.; Yoshio, M.; Hamasaki, A.; Mukai, T.; Ohno, H.; Kato, T. *Advanced Materials* **2009**, *21*, 1591.
- (14) de Araujo, C. C.; Kreuer, K. D.; Schuster, M.; Portale, G.; Mendil-Jakani, H.; Gebel, G.; Maier, J. *Physical Chemistry Chemical Physics* **2009**, *11*, 3305.
- (15) Long, J. W.; Rhodes, C. P.; Young, A. L.; Rolison, D. R. *Abstr Pap Am Chem S* **2003**, *225*, 306.
- (16) Rhodes, C. P.; Long, J. W.; Doescher, M. S.; Dening, B. M.; Rolison, D. R. *Journal of Non-Crystalline Solids* **2004**, *350*, 73.
- (17) Long, J. W.; Sassin, M. B.; Fischer, A. E.; Rolison, D. R.; Mansour, A. N.; Johnson, V. S.; Stallworth, P. E.; Greenbaum, S. G. *Journal of Physical Chemistry C* **2009**, *113*, 17595.
- (18) Gordon, R. G.; Hausmann, D.; Kim, E.; Shepard, J. *Chemical Vapor Deposition* **2003**, *9*, 73.
- (19) O'Shaughnessy, W. S.; Baxamusa, S.; Gleason, K. K. *Chem Mater* **2007**, *19*, 5836.
- (20) Charlier, J.; Ameer, S.; Bourgoin, J. P.; Bureau, C.; Palacin, S. *Advanced Functional Materials* **2004**, *14*, 125.
- (21) Palacin, S.; Bureau, C.; Charlier, J.; Deniau, G.; Mouanda, B.; Viel, P. *Chemphyschem* **2004**, *5*, 1469.
- (22) El Ouatani, L.; Dedryvere, R.; Siret, C.; Biensan, P.; Gonbeau, D. *J Electrochem Soc* **2009**, *156*, A468.
- (23) Mosby, J. M.; Prieto, A. L. *Journal of the American Chemical Society* **2008**, *130*, 10656.
- (24) Korepp, C.; Santner, H. J.; Fujii, T.; Ue, M.; Besenhard, J. O.; Moller, K. C.; Winter, M. *J Power Sources* **2006**, *158*, 578.
- (25) Han, G.-B.; Ryou, M.-H.; Cho, K. Y.; Lee, Y. M.; Park, J.-K. *J Power Sources* **2010**, *195*, 3709.
- (26) Tobishima, S.; Ogino, Y.; Watanabe, Y. *J Appl Electrochem* **2003**, *33*, 143.
- (27) Shima, K.; Shizuka, K.; Ue, M.; Ota, H.; Hatozaki, T.; Yamaki, J. I. *J Power Sources* **2006**, *161*, 1264.
- (28) Zhang, S. S. *J Power Sources* **2006**, *162*, 1379.
- (29) Bridel, J. S.; Grugeon, S.; Laruelle, S.; Hassoun, J.; Reale, P.; Scrosati, B.; Tarascon, J. M. *J Power Sources* **2010**, *195*, 2036.
- (30) Dedryvere, R.; Laruelle, S.; Grugeon, S.; Gireaud, L.; Tarascon, J. M.; Gonbeau, D. *J Electrochem Soc* **2005**, *152*, A689.
- (31) Gireaud, L.; Grugeon, S.; Laruelle, S.; Pilard, S.; Tarascon, J. M. *J Electrochem Soc* **2005**, *152*, A850.
- (32) Dedryvere, R.; Gireaud, L.; Grugeon, S.; Laruelle, S.; Tarascon, J. M.; Gonbeau, D. *J Phys Chem B* **2005**, *109*, 15868.

- (33) Ruffo, R.; Hong, S. S.; Chan, C. K.; Huggins, R. A.; Cui, Y. *Journal of Physical Chemistry C* **2009**, *113*, 11390.
- (34) Winter, M.; Appel, W. K.; Evers, B.; Hodal, T.; Moller, K. C.; Schneider, I.; Wachtler, M.; Wagner, M. R.; Wrodnigg, G. H.; Besenhard, J. O. *Monatsh Chem* **2001**, *132*, 473.

PART II: PHYSICAL CHARACTERIZATION AND HYDROGEN SORPTION KINETICS
OF SOLUTION-SYNTHEZIZED MAGNESIUM NANOPARTICLES

Chapter 5

Size-dependent hydrogen storage properties of Mg nanocrystals prepared from solution

Nick S. Norberg, Timothy S. Arthur, and Amy L. Prieto

Nick Norberg completed all the physical characterization of the Mg NCs. Timothy Arthur and Nick Norberg equally contributed to the synthesis, sorption data collection, and sorption data analysis of the Mg NCs.

This dissertation chapter is adapted from a manuscript submitted to *The Journal of the American Chemical Society*.

5.1 Introduction

A significant challenge for the widespread use of hydrogen as a practical alternative to fossil fuels is the development of safe and efficient storage materials for hydrogen. Light metal hydrides, such as MgH_2 , are promising hydrogen storage materials due to their high gravimetric and volumetric hydrogen storage densities (e.g. 7.6 wt.% H_2 and $110 \text{ kg H}_2/\text{m}^3$ for MgH_2)¹⁻³. Practical use of MgH_2 has been limited by the slow kinetics and high temperatures required for hydrogen absorption/desorption.

One successful strategy for improving the hydrogen storage properties of Mg and doped Mg samples has been the preparation of Mg with nanoscale particle sizes⁴⁻⁵. Theoretical calculations show that both Mg and MgH_2 become less stable with decreasing particle size⁶. Mechanical milling has frequently been used to increase the hydrogen sorption kinetics of Mg and MgH_2 by reducing particle grain sizes^{5,7-10}. Despite these improvements, the quality of the materials prepared by ball milling is limited since the materials properties, such as grain size, size dispersion, and surface structure are difficult to control. Reports of Mg nanowires and nanocrystals made by chemical methods have also shown a strong improvement in the hydrogen storage properties with decreasing particle size¹¹⁻¹⁴, however size control and the ability to dope the materials in situ is not possible with these synthetic approaches. A better understanding of the direct correlation between particle size and sorption kinetics can only be achieved when a synthetic approach that affords a range of narrow size dispersed samples is developed. In this dissertation, we report a direct chemical solution synthesis for the rapid preparation of Mg nanocrystals in gram quantities and of controllable sizes, and show a clear size-dependence of the hydrogen sorption kinetics.

5.2 Experimental

Mg nanocrystals (Mg NCs) were prepared by reducing a magnesocene (MgCp_2) solution dissolved in 1,2-dimethoxyethane (glyme). All steps were performed in a N_2 glove box. Two equivalents of a reducing solution of 0.5 M potassium biphenyl (25 nm particles), potassium phenanthrene (32 nm particles), or potassium naphthalide (38 nm particles) in glyme was quickly added to a rapidly stirring solution with one equivalent of MgCp_2 heated to 70 °C with the MgCp_2 concentration (including the reducing solutions) of 0.02 M (25 nm), 0.04 M (32 nm), or 0.08 M (38 nm), all in freshly-distilled glyme. The reducing solutions were centrifuged before use to remove the undissolved alkali metal. After stirring and cooling the solution for several minutes, the reactions were centrifuged and rinsed several times with glyme until the supernatant solutions were clear after centrifuging. The final Mg product was then evacuated for several hours under mild heat (50 °C) to yield a black (smallest particles) to medium grey powder (larger particles). For full experimental details, see Chapter 6.2

5.3 Physical characterization of MgNCs

Figure 4.1 1-top shows X-ray powder diffraction of the Mg nanocrystals. All peaks match those for hexagonal Mg, but the width of the peaks increases from the larger to smaller particles, as expected. Scherrer analysis of the most intense peak at 2θ of 36.7° provides particle size estimates of 25 nm, 32 nm, and 38 nm. TEM images (Figure 4.1-bottom) of these nanocrystals show that the particles are composed of larger aggregates and vary in shape, but with no well-defined faceted features. Analysis of > 100 nanocrystals per sample yield particle size and size-distribution estimates of 24 +/- 7 nm,

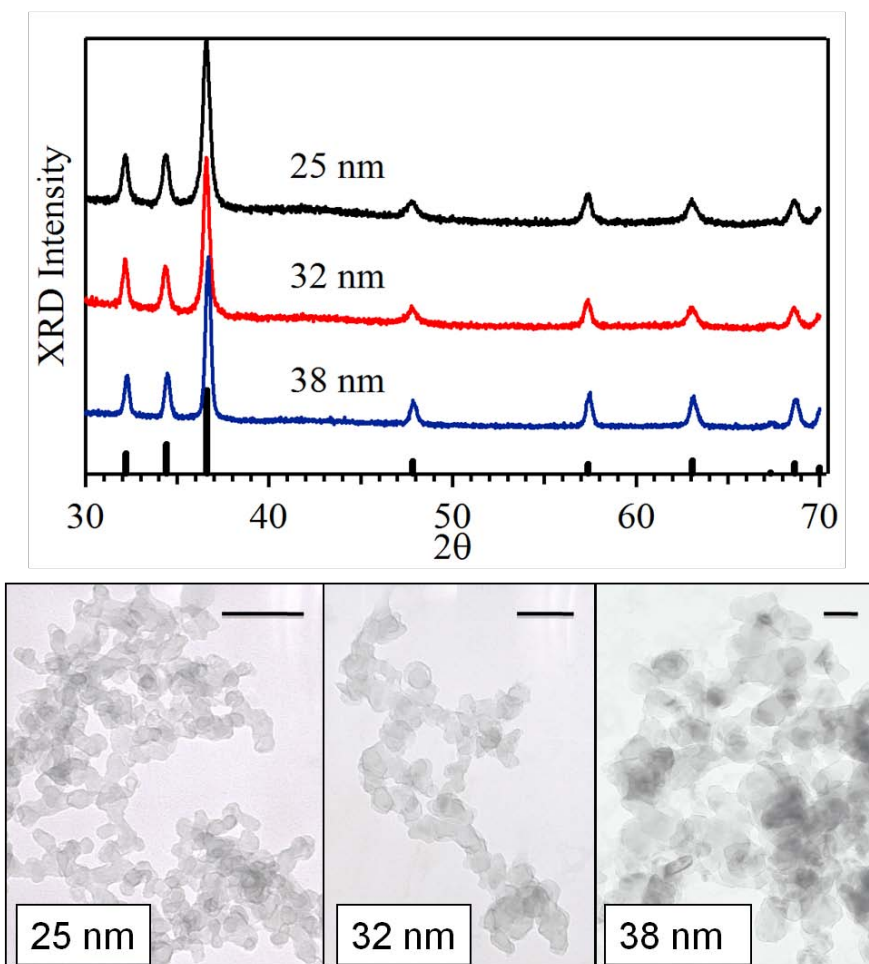


Figure 5.1. Powder XRD patterns (top) and TEM images (bottom) of Mg nanocrystals samples of 25 nm, 32 nm and 38 nm. The samples are labeled by the size calculated from Scherrer analysis. From left to right, the scale bar in the TEM images are 100 nm, 100 nm, and 50 nm.

35 +/- 10 nm, and 72 +/- 25 nm. Powder X-ray diffraction (XRD) measurements of the samples after hydrogen absorption show only the β -MgH₂ phase, confirming complete conversion from Mg to MgH₂ (Figure 5.2). The large difference in estimated particle size from the XRD pattern and TEM images of largest particles may be due to difficulties in seeing smaller particles or grains in the TEM images in the agglomerates of larger particles, and therefore the size estimated from the peak broadening in the XRD pattern will be considered more relevant for H₂ storage properties here. Scherrer analysis is more trustworthy here because it gives the average crystallite size over ~ 8 mg of sample

used in obtain the diffraction pattern, which is closer to the sample size used for sorption measurements (~25 mg). TEM analysis illustrates the low small size distribution of the material compared to ball-milled magnesium⁷.

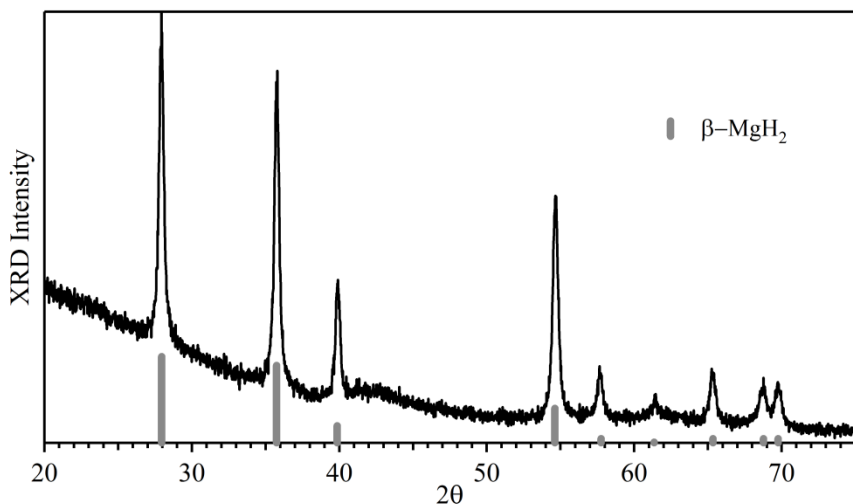


Figure 5.2 Powder diffraction pattern of 25 nm MgNCs after hydrogen absorption at 300 °C, with the indexed diffraction pattern for tetragonal β -MgH₂.

5.4 Hydrogen absorption/desorption properties of MgNCs

Figure 5.3 shows the hydrogen absorption for Mg nanocrystals in the pressure range of 11.5 to 9.9 bar, and desorption kinetics of the same particles recorded between 0.6 to 0.2 bar, measured through pressure change using Sievert's method. The 25 nm particles absorbed 95% of the maximum capacity within 60 seconds at 300 °C, with the 32 nm and 38 nm particles absorbing 95% of their maximum capacity within 140 seconds and 420 seconds, respectively. The same trend of increasing reaction time from small to large is followed at all temperatures for absorption and desorption, demonstrating the strong enhancement of kinetics that is observed for hydrogen absorption/desorption by decreasing the size of the Mg nanocrystals.

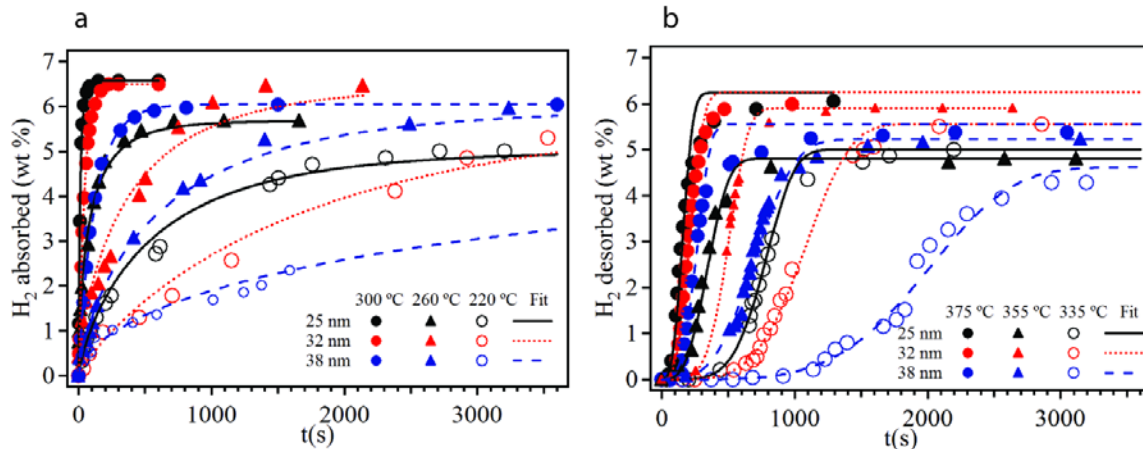


Figure 5.3. Hydrogen (a) absorption and (b) desorption of magnesium nanocrystals at different temperatures.

Peak broadening analysis of powder diffraction measurements of the 25 nm particles after heating to 300 °C under vacuum for several hours, and after hydrogen absorption at 300 °C and desorption at 375 °C, show that the Mg nanocrystals do not significantly change in size before absorption (27 nm), but do grow after an absorption/desorption cycle (Figure 5.4). Therefore the particles retain their differences in particle size through these measurements before the desorption measurements. The Mg nanocrystals do grow significantly after desorption measurements (98 nm) (Figure 5.4), however.

The sorption data shown in Figure 5.3 were fit using the Johnson-Mehl-Avrami equation, $x_{fr} = 1 - \exp(-kt)^n$, where x_{fr} is the fraction of Mg or MgH₂ that has reacted for absorption or desorption, k is the reaction rate, t is time, and n is the reaction exponent (See 5.5 for notes on calculations)¹⁵⁻¹⁶. The results from the best fits are displayed in Figure 5.3 as lines through the data points. The desorption data was fit up to 60% of the desorbed fraction since the data typically deviated from the fit beyond this point. Using

the k values obtained from the fit of the data, the activation energies (E_a) were calculated for absorption and desorption of hydrogen for each sample with the

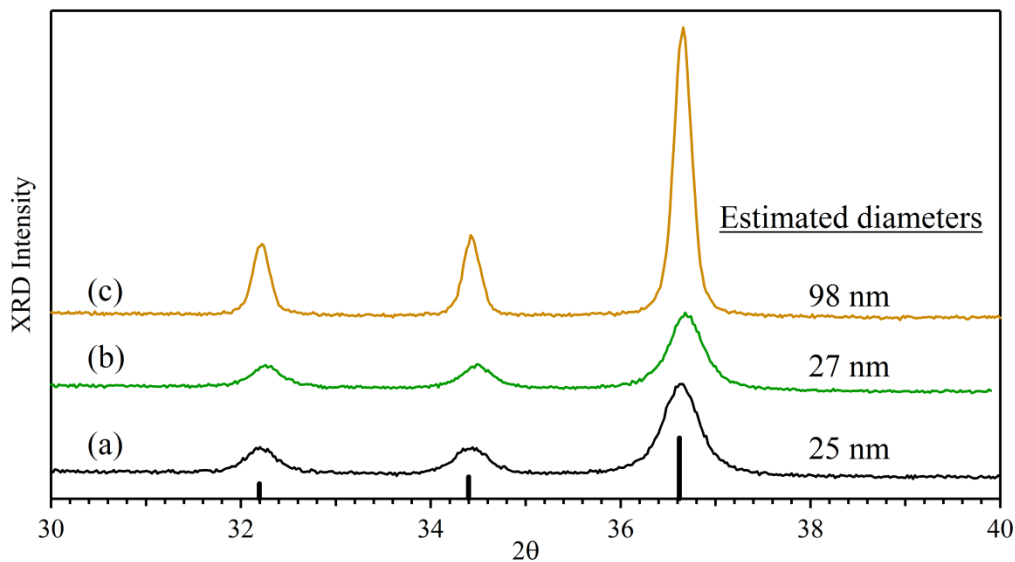


Figure 5.4. Powder diffraction pattern of 25 nm Mg NCs (a) as-prepared, (b) after annealing under vacuum at 300 °C for several hours and (c) after H₂ absorption at 300 °C and desorption at 375 °C. The particle size estimates based on the peak broadening at 2θ of 36.7 ° are listed.

Arrhenius equation (Figure 5.5). The calculated E_a values for hydrogen absorption were 122, 118, and 115 kJ/mol H₂ for 25 nm, 32 nm, and 38 nm, respectively. These values show a clear trend even over this small size range, and are within the range of previously reported E_a values for hydrogen absorption by bulk Mg (95-130 kJ/mol H₂)¹⁵. The calculated E_a values for hydrogen desorption were 126, 131, and 160 kJ/mol H₂ for 25 nm, 32 nm, and 38 nm, respectively. The size of the particles does appear to influence the E_a for desorption, but these energies are still in the range of previously reported values for bulk Mg (120-160 kJ/mol H₂)¹⁴.

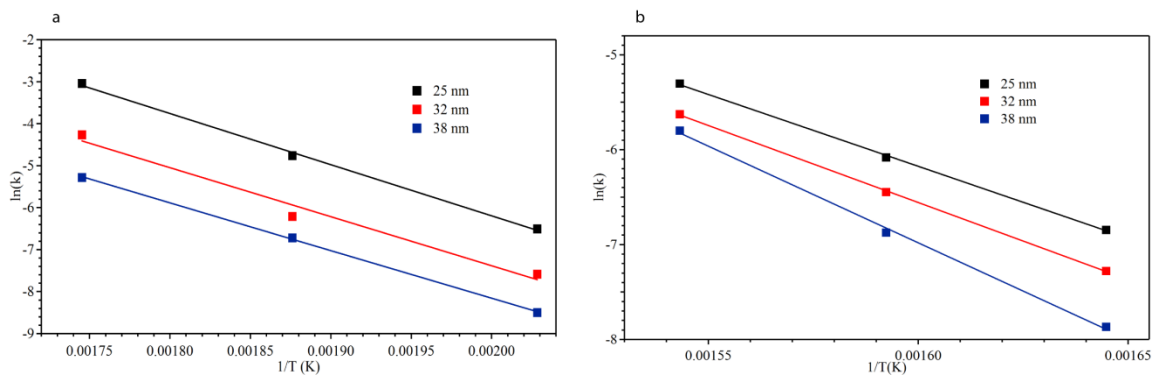


Figure 5.5. Arrhenius plots for (a) absorption and (b) desorption of H₂ from 25 nm, 32 nm, and 38 nm Mg nanocrystals.

5.5 Conclusions

Despite the small differences in activation energies, there is a dramatic difference in absorption/desorption reaction rates that was much greater than the size differences between the Mg nanocrystals, particularly for the H₂ absorption reaction. Figure 5.6 plots the H₂ absorption reaction rates for all the samples at each temperature relative to the largest samples versus the nanocrystal diameters estimated from the powder XRD patterns. The rates for 25 nm particles are over seven times higher than for 38 nm particles. This cannot be attributed to increasing surface area or decreasing diffusion distance alone, since the rate does not follow the inverse dependence to the particle diameter that would be expected (line in Figure 5.6). Since defect sites have been cited as important components of Mg-based materials to improving the kinetics of H₂ sorption^{5,10}, we hypothesize that there is an increase in the density of defect sites formed through the low-temperature solution synthesis described here as smaller nanocrystals are prepared. This demonstrates that the solution synthesis can provide a simple route to Mg nanocrystals with enhanced H₂ sorption kinetics.

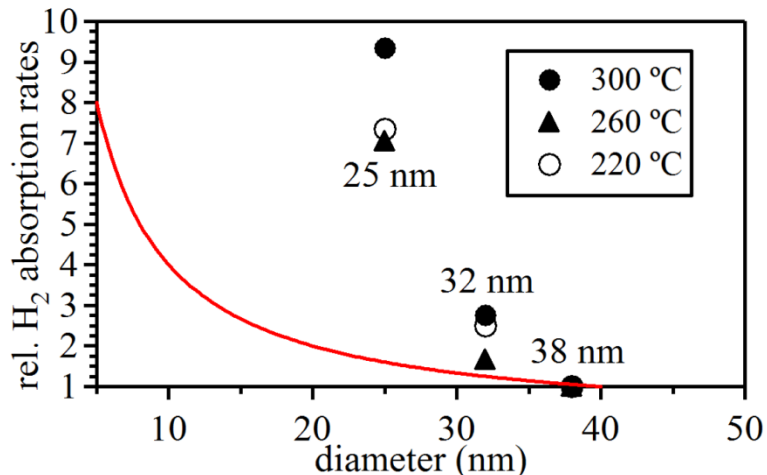


Figure 5.6. Hydrogen absorption rates for 25 nm, 32 nm and 38 nm magnesium nanocrystals at different temperatures. The solid line follows a 1/diameter relationship.

5.6 Notes on calculations of reaction rates and activation energies.

From rearrangement of the Johnson-Mehl-Avrami equation, $x_{fr} = 1 - \exp(-kt)^n$, plotting the data as

$$\ln(-\ln(1-x_{fr})) \text{ versus } \ln(t)$$

yields a straight line where $n = \text{slope}$ and $k = \exp(\text{y-intercept}/\text{slope})$. For determining the activation energies through the Arrhenius equation, the k values were corrected for the difference in driving forces due to changing Mg-H equilibrium pressures with the change in temperatures for each reaction,

$$k_{\text{meas}} = k_{\text{act}} * g(P).$$

Here k_{act} is the actual reaction rate and $g(P)$ represents the relationship between the driving force and pressure, which either follows a linear $(1 - P_{\text{eq}}/P)$ or parabolic $(1 - (P_{\text{eq}}/P)^{1/2})$ relationship for absorption and desorption (replace P_{eq}/P with P/P_{eq}). P is the H₂ pressure during the reaction and P_{eq} is the equilibrium H₂ pressure. Separate Mg absorption experiments show that the experiments here follow the parabolic relationship

slightly better than the linear relationship, and the calculation of activation energies uses this relationship, but these experiments could not rule out the possibility that the driving force follows the linear relationship.

5.7 References

- (1) Schlapbach, L.; Züttel, A. *Nature* **2001**, *414*, 353.
- (2) Schuth, F.; Bogdanovic, B.; Felderhoff, M. *Chemical Communications* **2004**, 2249.
- (3) Zaluska, A.; Zaluski, L.; Strom-Olsen, J. O. *Applied Physics a-Materials Science & Processing* **2001**, *72*, 157.
- (4) Berube, V.; Radtke, G.; Dresselhaus, M.; Chen, G. *International Journal of Energy Research* **2007**, *31*, 637.
- (5) Zaluski, L.; Zaluska, A.; Strom-Olsen, J. O. *Journal of Alloys and Compounds* **1999**, *290*, 71.
- (6) Wagemans, R. W. P.; van Lenthe, J. H.; de Jongh, P. E.; van Dillen, A. J.; de Jong, K. P. *Journal of the American Chemical Society* **2005**, *127*, 16675.
- (7) Huot, J.; Liang, G.; Schulz, R. *Applied Physics a-Materials Science & Processing* **2001**, *72*, 187.
- (8) Lu, J.; Choi, Y. J.; Fang, Z. Z.; Sohn, H. Y.; Ronnebro, E. *Journal of the American Chemical Society* **2010**, *132*, 6616.
- (9) Paskevicius, M.; Sheppard, D. A.; Buckley, C. E. *Journal of the American Chemical Society* **2010**, *132*, 5077.
- (10) Sakintuna, B.; Lamari-Darkrim, F.; Hirscher, M. *International Journal of Hydrogen Energy* **2007**, *32*, 1121.
- (11) Kalidindi, S. B.; Jagirdar, B. R. *Inorganic Chemistry* **2009**, *48*, 10856.
- (12) Li, W. Y.; Li, C. S.; Ma, H.; Chen, J. *Journal of the American Chemical Society* **2007**, *129*, 6710.
- (13) Aguey-Zinsou, K. F.; Ares-Fernandez, J. R. *Chemistry of Materials* **2008**, *20*, 376.
- (14) Bogdanovic, B. *International Journal of Hydrogen Energy* **1984**, *9*, 937.
- (15) Fernandez, J. F.; Sanchez, C. R. *Journal of Alloys and Compounds* **2002**, *340*, 189.
- (16) Rudman, P. S. *Journal of the Less-Common Metals* **1983**, *89*, 93.

Chapter 6

Solution-synthesized Mg nanocrystals: *In situ* doping with Ni_(m), physical characterization and H₂-storage properties

Sarah Frederick completed all XRD and TEM experiments in this chapter. Zhaoping Ni (Shores Group - CSU) synthesized the magnesocene precursor material. Timothy Arthur performed all other experiments in this chapter.

6.1 Introduction

Magnesium metal, when hydrogenated to form MgH_2 , is a potential solution towards finding an effective hydrogen-storage material due to the large gravimetric capacity (7.6 wt.% H_2) and volumetric capacity ($110 \text{ kg H}_2/\text{m}^3$)¹⁻³. As a bulk powdered material, Mg has slow rates of hydrogenation and dehydrogenation (H/D) at temperatures below 623 K. However, kinetic enhancements have been made by ball-milling bulk-Magnesium powder into micro- and nanoparticles⁴⁻⁸. Magnesium nanowires of different diameters have also been synthesized with elaborate high-temperature CVD techniques⁹, showing excellent adsorption and desorption kinetics at temperatures $< 573 \text{ K}$, but after 10 cycles, the wires sintered into nanoparticles.

The increased surface area of nanostructures offers larger number of H_2 dissociation sites and fast gaseous diffusion to the center of the material¹⁰. In addition, the rate-limiting step is the diffusion of H through $\beta\text{-MgH}_2$; therefore, particles of small sizes facilitate faster H-transport to the core of the particle as compared to larger particles. The rapid increase in kinetics, compared to bulk powdered-Mg, highlights the successful approach to increasing the sorption rate with nanostructured materials^{9,11-13}. Previously, we have illustrated a novel solution-based method of synthesizing Mg nanoparticles with low polydispersity and high-yield¹⁴. Hydrogenation and dehydrogenation rates were also found to be the fastest for solid Mg hydrogen storage materials. The rate of hydrogenation and dehydrogenation for our smallest solution-synthesized Mg NCs, ~16 nm, are superior to rates observed by other groups for ball-milled Mg particles and CVD-synthesized Mg-nanowires. However, our initial calculations for activation energy, E_a , of hydrogenation (90-120 kJ/mol)¹⁵ and dehydrogenation (130-150 kJ/mol)¹² are

comparable to values obtained for both microstructured Mg-powder and nanostructured, ball-milled Mg. A substantial decrease in E_a is observed by doping Mg with a catalyst particle. Zero valence transition metals have been shown¹⁶⁻¹⁷ to be catalytic towards the splitting of H₂-gas.

Using dopants in hydrogen storage materials facilitates faster kinetics and better rates at higher (adsorption) or lower (absorption) temperatures^{1-2,8,10,18-19}; however, the mass of the dopant decreases the gravimetric capacity of stored-H₂. Finding a minimum mass of catalyst is vital to achieving the maximum storage. It is also advantageous to find new ways of doping materials; in particular, solution-based synthetic methods can make homogenous nanomaterials whose physical properties differ within a very narrow range. Doping in solution uniformly may distribute the catalyst across the surface of the nanoparticles, but this method of doping Mg has not been reported. Doping with ball-milling techniques produces inhomogeneous doping products^{11,20-23}. For example, Hanada *et al.*²³ report the presence of three separate phases of Ni after ball-milling Mg with 5 wt.% Ni-powder: Mg₂Ni, Ni_(m) nanoparticles, and Ni_(m) on the surface of Mg. Deciphering the catalytic effect of each of phases is difficult to accomplish. Ares *et al.*²¹ also detect the presence of impurities from a milling procedure, and the hydrogenation and dehydrogenation kinetics varied drastically with the type, size, and purity of the milling material. As a result, hydrogen adsorption and desorption rates for Mg ball-milled with the same amount of catalyst can vary between reports^{16-17,24}.

The effect of doping on hydrogenation and dehydrogenation rates with various catalytic transition metal (TM)^{16-17,24-34}, transition metal alloys (TMA)³⁵⁻⁴⁰, and transition metal oxides (TMO)⁴¹⁻⁴⁶ has been extensively studied. In high-temperature storage

media, such as Mg, dopants have been found to lower the E_a , reflected by the faster rates at lower temperatures. Nickel metal is a popular choice of dopant for Mg because it is cheap (\$3.20/g – Sigma Aldrich), light (compared to 2nd and 3rd row TMs), and alloys with Mg to form another H₂-storage material, Mg₂Ni⁴⁷⁻⁴⁹. Ni also has a large nuclear cross-section, which permits small amounts to be detected with neutron diffraction. Fuji *et al.*⁵⁰ concluded that Ni_(m) is the best first-row TM catalyst for hydrogen storage in Mg.

Wronski *et al.*⁵¹ and Li *et al.*⁵², have also studied the effect of micro- and nanoparticles of Ni_(m) on the desorption kinetics of MgH₂. Though a substantial improvement in the E_a (desorption) was observed for doping levels as low as 5 wt% Ni_(m), the current, synthetic methods still relied on mechanical-milling techniques over a long period (20 h) or hydrogen-plasma metal reactions⁵³. The only solution-phased synthesis of Mg was demonstrated by Bogdanovic *et al.*¹², and was achieved by the hydrogenation of magnesium-based organometallic compounds. No solution-phase doping of MgNCs has been reported. Here we investigate the solution-based *in situ* Ni_(m)- doping of MgNCs and the effect of doping on the hydrogenation/dehydrogenation kinetics and cyclability.

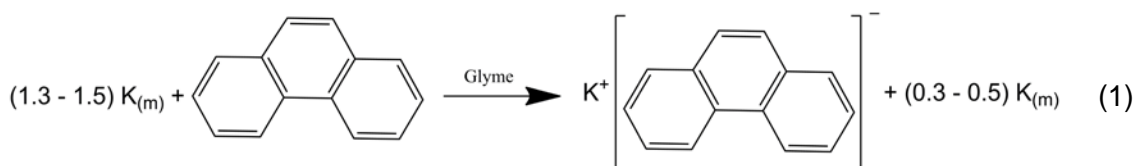
6.2 Experimental

Chemicals: 1,2-dimethoxy ethane (glyme, Sigma-Aldrich, anhydrous, 99.99 %) and hexanes (Sigma-Aldrich, anhydrous, 99.99 %) were refluxed over sodium for 12 h before use. Magnesiumocene (MgCp₂) was synthesized from literature methods by Zhoaping Ni (Shores Group - CSU), and the purity was confirmed with ¹H-NMR; all chemicals materials were purchased from Sigma-Aldrich and used as received. Phenanthrene

(Sigma-Aldrich, 99%) and nickelocene (NiCp₂, Strem Chemicals, 99%) were used as received. All chemicals were stored in a N₂-filled glove-box with O₂ and H₂O levels < 0.1 ppm.

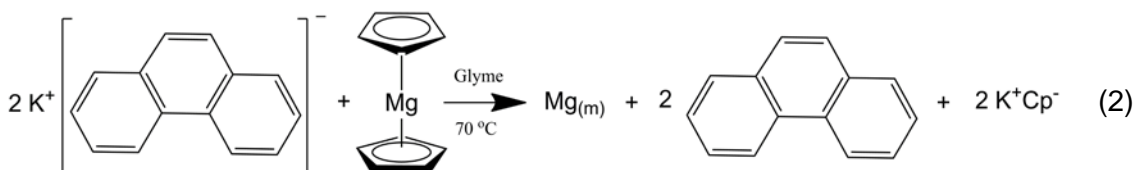
Synthesis of Mg NCs: All steps were performed in a N₂-filled glove-box.

A. *Preparation of reducing solution (RS):* The 0.1 M KPHEN/glyme homogenous reducing solution was synthesized via:



After centrifugation to remove the unreacted K_(m) or potassium salts, the product was a viscous dark-green solution.

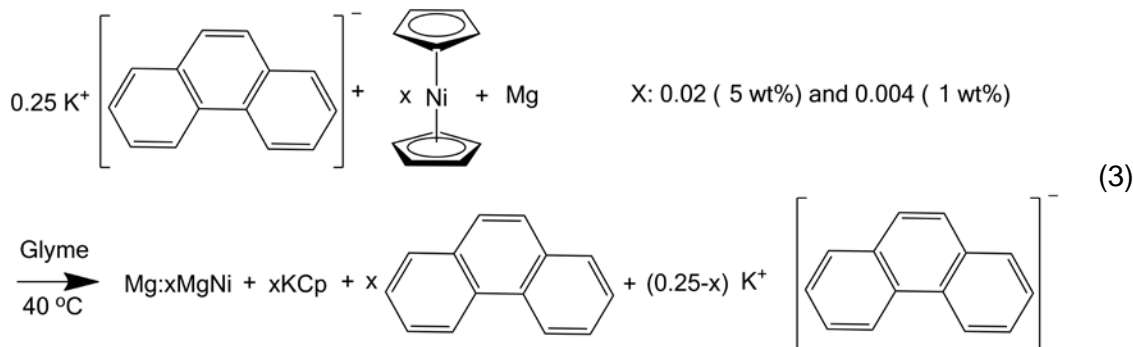
B. *Preparation of Mg NCs:* A 0.04 M MgCp₂/glyme solution was heated to 70 °C under vigorous stirring. The RS was then added rapidly and the temperature was reduced to 40 °C. Reaction (2):



produces a light-green solution with a black precipitate (MgNCs).

C. *Preparation of Ni_(m)-doped Mg NCs:* For Ni-doped samples (0, 1, 5 and 20 wt%), a 25 mol% excess of the RS was used. Once the Mg NC solution cooled to 40 °C, a predetermined volume (calculated assuming the complete

conversion of NiCp₂) of 0.01 M NiCp₂/glyme solution was added drop-wise with constant stirring (3):



The solution was stirred for 30 min. The product was then centrifuged and washed with clean glyme several times until the supernatant was clear. The product was dried under vacuum resulting in a light-black powder. The yield for the reaction is 90-95 % and it was consistent for Mg_(m) batches ranging from 25 mg to 1.5 g.

Hydrogenation/Dehydrogenation (H/D): Absorption and desorption isotherms were collected using a Seivert's type apparatus in the pressure range of 8.85-8.88 bar (hydrogenation) and 0.19-0.20 bar (dehydrogenation). The volume of the system was calibrated gravimetrically with isopropanol. Changes in pressure were monitored using a high-pressure gauge (MKS Model 627 Absolute Capacitance Manometer) for adsorption measurements and a low-pressure gauge (KJL 1500 series Diaphragm manometer) for desorption measurements. H₂-sorption measurements from our previous work were taken without digital pressure gauges or an automated timing system¹⁴. Cycling experiments were performed by hydrogenating each sample for 30 min at the given temperature, raising the temperature 50 K to the desorption temperature, and then recording the dehydrogenation kinetics at the new temperature. All samples were then dehydrogenated

at 573 K for an additional 1 hr before beginning a new cycle. Both pressure gauges were interfaced with a PC-controlled *LabView* program.

Physical characterization - X-ray photoelectron spectroscopy (XPS) (Phi 6500) was used to characterize the surface of the Mg NCs. Measurements were performed with a 5800 series Multi-Technique ESCA system and analyzed using Multipak software. An Al monochromatic source operating at 350.0 W was scanned with a pass energy of 58.7 eV in intervals of 0.125 eV step⁻¹ over the range indicated on the spectra. All XPS spectra were shifted so that the adventitious C1s peak was located at 284.7 eV. Peak positions are reported from peak-fitting of the data. Low magnification TEM images used for particle size analysis were obtained on a JEOL JEM 2000 at a working voltage of 160 kV. High resolution TEM images and selected area electron diffraction were obtained on a Philips CM200 TEM at a working voltage of 200 kV. EDX was obtained on the same TEM using a Princeton Gamma-Tech Prism Energy Dispersive X-Ray Spectrometer. The samples were prepared by sonicating a small amount of sample in a solution of glyme. Carbon-coated copper TEM grids (200 mesh, Structure Probe, Inc.) were dipped into this solution three times and dried. X-ray diffraction patterns were obtained on a Scintag X-2 Advanced Diffraction system equipped with Cu K α radiation ($\lambda=1.54$ Å). The XRD samples were prepared by covering Mg NC powder with a mixture of glyme and mineral oil to prevent oxidation.

6.3 Results and discussion

Synthesis of undoped and Ni_(m)-doped MgNCs

The synthesis of magnesium, and magnesium-halide salts in particular, has long been an important preparation step for Grignard chemistry. In 1981, Rieke *et al.*⁵⁴ reported the preparation of highly reactive magnesium metal by the reduction of MgCl₂ with lithium metal and a small amount of electron carrier (naphthalene and biphenyl) in glyme or THF. Since this reaction was merely a first step towards making highly reactive Grignard reagents, little physical characterization was done to optimize particle size or size-distribution of Mg. No H₂ absorption or desorption work was done.

To make Mg NCs, we have adapted this synthesis by using a metallocene precursor and a stoichiometric amount of reductant. By rapidly mixing the reducing solution with the heated metallocene solution, as in “hot-injection” methods for nanostructure synthesis, we obtained a high-yield of Mg NCs with a small size distribution. We have achieved this synthesis with a variety of alkali metals (K, Li and Na) and electron carriers (phenanthrene, biphenyl and naphthalene) in glyme and produced Mg NCs ranging from 16 nm to 38 nm (via XRD). In this work, however, we will report only on the synthesis of 32 nm Mg NCs with varying amount of Ni_(m) dopant, to determine the role of the catalyst on the sorption kinetics of the Mg NCs.

The next synthetic goal was to find a suitable H₂-sorption catalyst that could be uniformly distributed across the surface with Mg in the solution phase. The challenges involved the reactivity of Mg_(m) with the anions of many metal salts and solubility of the dopant-precursor in glyme. Table 6.1 outlines the reduction potentials for some of the reaction constituents of the Mg NC and Ni_(m)-doped Mg NCs. NiCp₂ does not deposit on

the Mg NCs without the presence of the reducing solution, although it is thermodynamically favorable. However, at 40 °C in the presence of excess reducing solution (0.25 mol), elemental Ni is detected on the surface of the nanoparticles (via XPS – discussed below). The reduction of NiCp₂ onto the surface of Mg NCs is an interesting process that deserves further discussion (6.4).

XPS analysis of undoped and Ni_(m)-doped MgNCs

The surface of the MgNCs was analyzed with high resolution scans of the Mg 2s, Mg 2p, Mg KLL, O 1s, Ni 3d 3/2 and Ni 3d 1/2 regions. Since keeping the MgNC samples totally air-free was not possible, all samples were exposed to an ambient environment for a short time (~3 sec). There is no apparatus to transport the Mg NCs from the N₂-filled glove-box to the X-ray spectrometer.

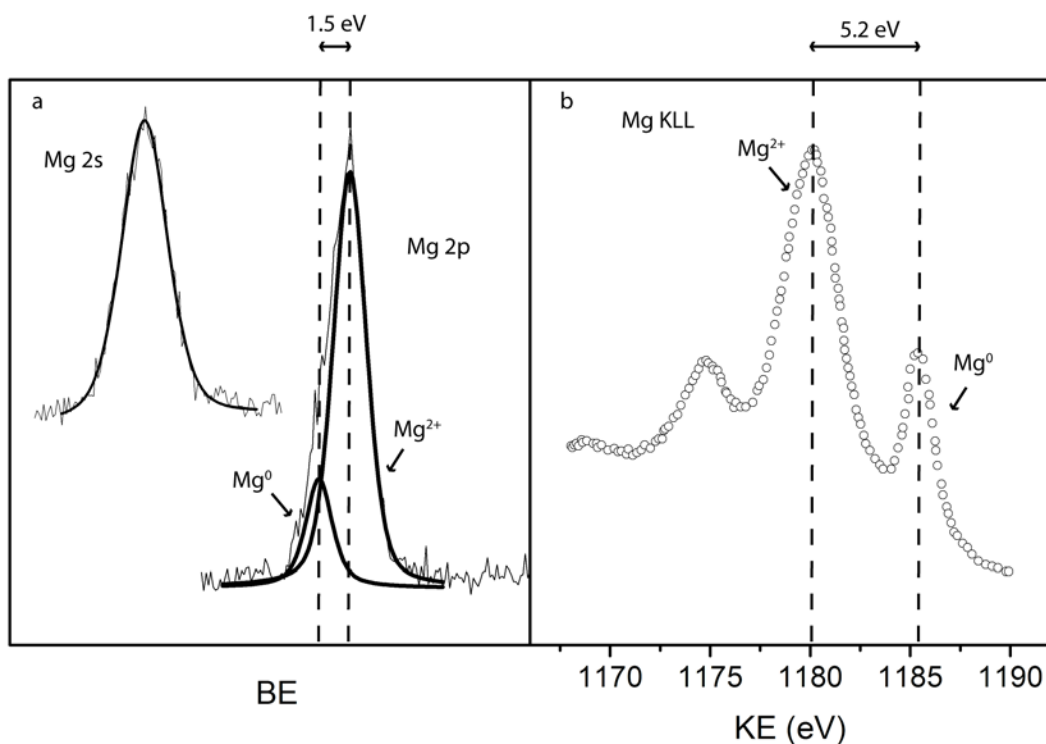


Figure 6.1. a) XPS HRES spectra of the Mg 2s and Mg 2p regions. b) The Mg KLL peak when binding energy (BE) has been converted to kinetic energy (KE).

The highly-exothermic reaction of Mg with O₂ (Mg_(m) is pyrophoric) and the nanoscale dimensions of the metal caused surface oxidation reactions to quickly form a shell of MgO. Experimentally, the surface-oxidation had two consequences. Friedrichs *et al.*⁵⁵ outlined a better means to resolve Mg_(m) and MgO. First, the separation of binding energies for the two oxidation states of Mg is small. the Mg 2p peak splitting (~1.5 eV) between Mg⁰ and Mg²⁺ compounds is better than that seen for the Mg 2s peak that typically fit to only 1 peak (Figure 6.1a). By plotting the kinetic energy (KE) instead of the binding energy (BE) for the Mg KLL signals, the larger peak separation (~5.2 eV) permits the two compounds to be resolved (Figure 5.1b). In addition, the KE for Mg_(m) and MgO in the Mg NCs match values found in literature⁵⁶⁻⁵⁷. Another consequence of surface-oxidation is the conductivity of the samples. Once MgO is formed, the conductivity of the Mg NCs decreases dramatically; 4.4 x 10⁻⁸ Ω m for Mg_(m) to 100 -0.1 Ω m) for MgO_x (depending on the oxygen content). The poor conductivity leads to poor signal to noise ratios for the Ni 3d peaks and atomic percentage comparisons are unreliable. Elemental analysis to determine the exact content of Ni_(m) on the surface is underway.

The peak positions were consistent between samples, and the curve-fitting analysis of the Ni 3d 1/2 and 3d 3/2 are shown in Figure 6.2 and Table 6.1. The results highlight two major differences between the Ni⁰ on the Mg NCs and the Ni²⁺-ion in Ni(OH)₂ that had formed on nickel powder. The 3d 1/2 - 3d 3/2 doublet shifts to higher binding energies for Ni as the oxidation state of the element increases because the effective nuclear charge felt by core electrons increases as the oxidation state increases. The 3d 3/2 peak for

Table 6.1. Peak positions for synthesis –related Ni compounds.

Sample	3d 1/2 (eV)	3d 3/2 (eV)	Δ_p (eV)
Ni on Mg	870.2 (3)	853.5 (2)	16.7 (2)
Ni(OH) ₂ (Ni Powder)	874.3 (3)	856.6 (2) (sat) 862.4 (2)	17.7 (2)
Ni(OH) ₂ (NIST)	874.4	856.6 (sat) 862.4	17.8
NiCp ₂	----	856.6	----
Ni	(870.7)	852.9(4)	17.2 (2)

Ni(OH)₂ and NiCp₂ shifts +3 eV on average to the Ni peak seen in the Mg NC Ni 3d HRES scans and compared to literature values compiled by NIST⁵⁸⁻⁶⁰. The splitting between the 3d 1/2 and 3d 3/2 peaks for Ni in different oxidation states is also a good indication of the nickel valency. The splitting of the 3d peaks for Ni on the Mg NCs is 1 eV less than the splitting observed for Ni(OH)₂ and close to values reported for Ni_(m). The exact valency of the Ni cannot be determined, since anionic nickel (from MgNi alloy formation) on the surface has not been discounted. However, peak positions and peak-splitting analysis has proven the transformation of NiCp₂ to a metallic or anionic form of Ni. EXAFS measurements and neutron PDF analysis will further elucidate the nature of Ni on the MgNCs. For the remainder of this work, the Ni will be referred to as Ni⁰ or Ni_(m).

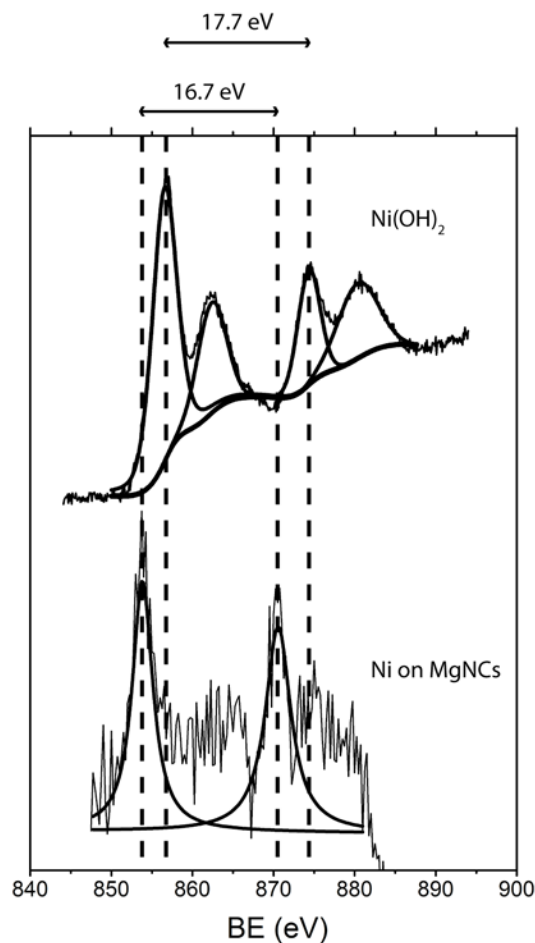


Figure 6.2. XPS HRES spectra of the 3d region for Ni for NiOH (on Ni_(m) powder, top) and Ni⁰ on MgNCs (bottom).

XRD and TEM of undoped and Ni_(m)-doped Mg NCs

Figure 6.3 contains powder-XRD patterns of undoped-Mg NCs, 20 wt.% Ni-doped Mg NCs, β -MgH₂ and Ni-powder. All the peaks in Mg NC samples index to hexagonal Mg_(m). Scherrer analysis of the most intense peak at 2θ of 36.7° gives a size estimate of 32 nm for the undoped and 20 wt.% Ni-doped Mg NCs, consistent with our previous report. The pattern labeled β -MgH₂ is the diffraction pattern of a 5 wt% Ni-doped sample hydrogenated at 523 K for 30 min. No peaks index to Mg_(m), indicating the complete conversion of Mg_(m) to MgH₂. Also, no Mg NC or MgH₂ samples display the presence of any Ni_(m) peaks. This result implies that any Ni present in the Mg NCs is not crystalline;

that is, the Ni does not have any long-range structural order. Reported XRD patterns⁵⁰⁻⁵¹ of Mg_(m) ball-milled with 5 wt.% Ni_(m) can detect crystalline Ni_(m). However, XPS results indicate the presence of Ni⁰ on the surface of the Mg NCs. Therefore, we hypothesize our synthetic method deposits Ni⁰ on the surface, but the Ni⁰ is not crystalline. Neutron diffraction of Ni-doped Mg NCs has been obtained in collaboration with Dr. Steve Conradson at LANL, and the data analysis by his group will help determine the location and oxidation state of the Ni.

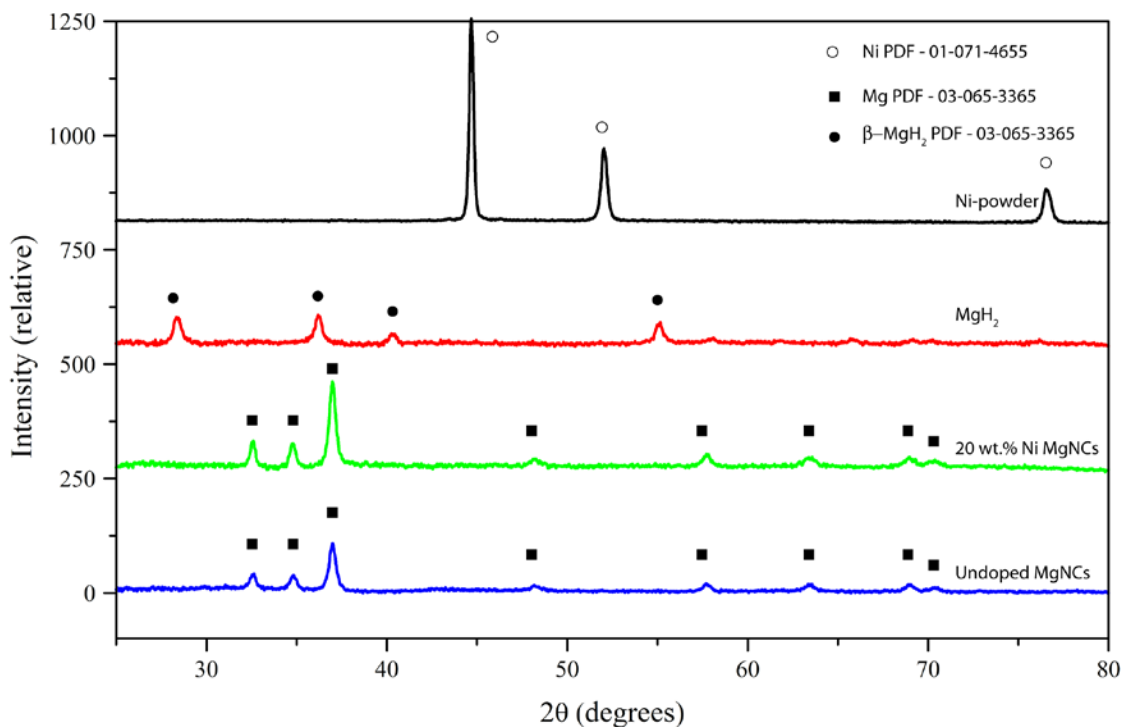


Figure 6.3. XRD patterns of undoped MgNCs, 20 wt.% Ni-doped MgNCs, MgH₂ and Ni_(m)-powder.

Figure 6.4 is a HRES TEM image of 5 wt.% Ni-doped Mg NC sample. The agglomerated nanocrystals have no defined shape due to the lack of any surfactant in the synthesis. The familiar size and shape of the Mg NCs, when compared to 32 nm pure

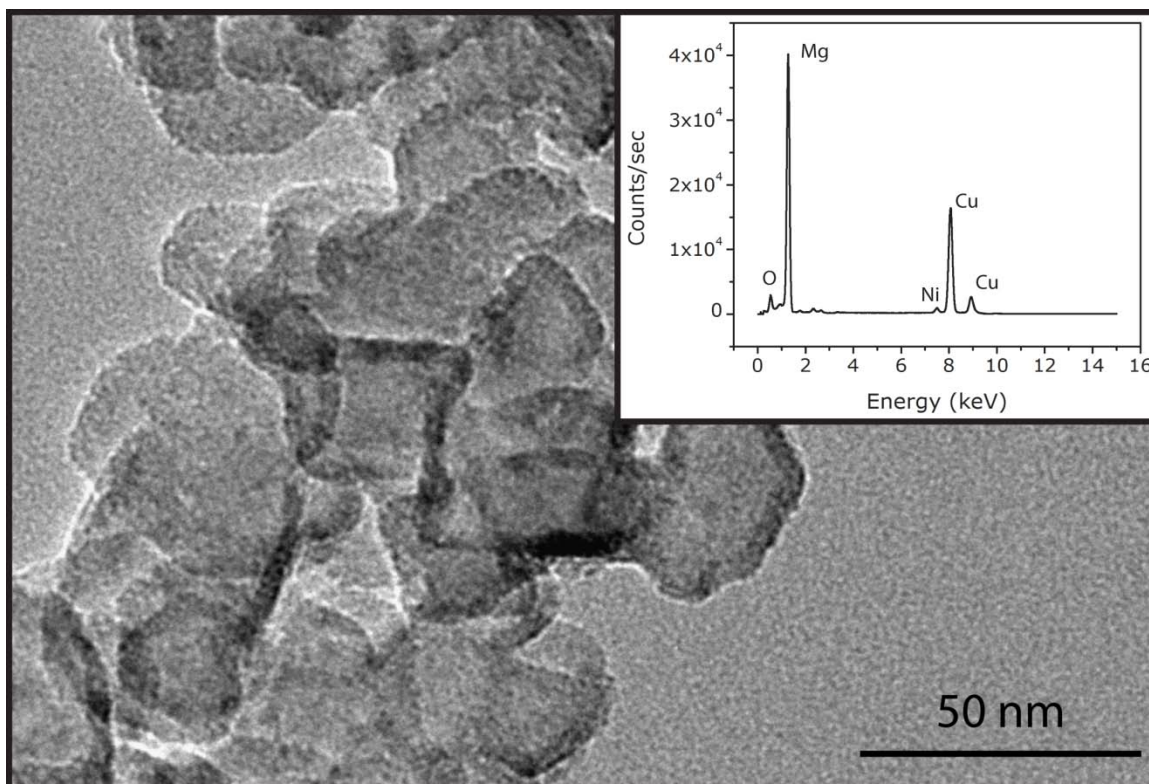


Figure 6.4. HRES TEM image of 5 wt.% Ni-doped MgNCs. EDX spectrum of 5 wt. % Ni-doped Mg NCs.

Mg NCs (Chapter 5), highlight the consistency of the synthesis. Superfluous organic materials will decrease the H₂-storage capacity of the nanocrystals, and therefore, surfactant coating was never part of the synthetic plan. Analysis of > 200 particles gives a size-distribution of 36 ± 11 nm, close to the value obtained with Scherrer analysis. There are no obvious islands of Ni_(m) on the surface of the Mg NC, but the result is not surprising because of the lack of any crystalline Ni_(m) in the diffraction pattern. EDX analysis (inset) does detect the presence of elemental Ni throughout the sample.

Hydrogen absorption and desorption properties

The H/D kinetics of the Mg NCs were monitored directly at various temperatures (523 K, 548 K and 573 K) for absorption and (573 K, 598 K and 623 K) desorption. Figure

6.5 is the reacted fraction of H₂ plotted against time of the Mg NCs during the hydrogenation and dehydrogenation process. The positive influence of the 5 wt.% Ni catalyst on both processes is apparent, as it takes < 1 min to absorb 80 % of the maximum capacity (523 K) and about 10 min to release 80 % of the absorbed H as H₂ gas (573 K). The undoped particles took approximately 5 min and 24 min to achieve the same limits. The MgNCs doped with only 1 wt.% Ni produced absorption isotherms that were comparable to the undoped nanocrystals. The desorption on-set time (before any release

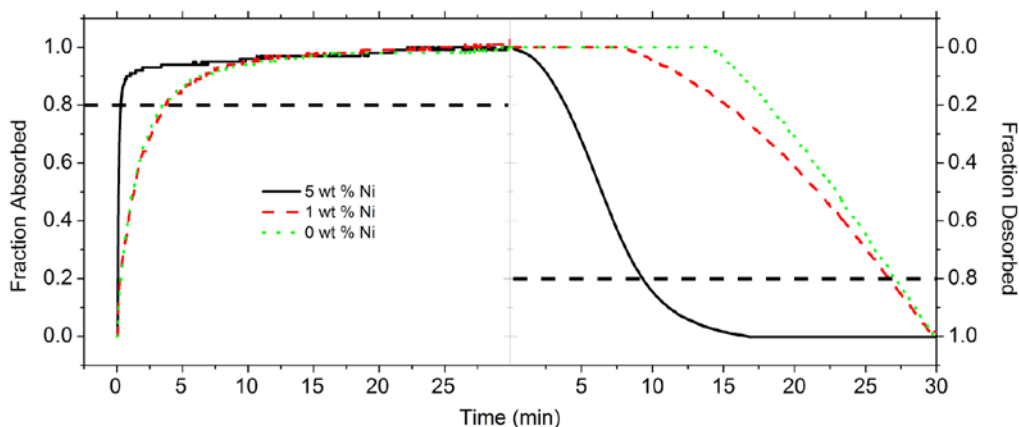


Figure 6.5. Hydrogen absorption (523 K) and desorption (573 K) of MgNCs with 5 wt% (line), 1 wt% (dash) and 0 wt% (dot) Ni_(m)

of H₂ gas) for the doped samples is faster than the undoped samples at 573 K and small observed effect on the E_a of the particles is discussed later. Since the particles are the same size and have a low polydispersity, the improved kinetics are attributed to the presence of the Ni-catalyst.

The sorption data was fit using the Johnson-Mehl-Avrami (JMA) equation, $x_{fr} = 1 - \exp(-kt)^n$, where x_{fr} is the fraction of Mg or MgH₂ that has reacted for absorption or desorption, k is the reaction rate, t is time, and n is the reaction exponent. For full details

on calculations, see Chapter 5.6 - “Notes on Calculations of reaction rates and activation energy”. Values for rate constants were obtained from the fit to the data, and Arrhenius plots were extrapolated (Figure 6.6a and b for absorption and desorption, respectively). The linear trend fitted to the Arrhenius plot was used to calculate the E_a for the Mg NCs. Table 6.3 outlines the results obtained from the kinetic data.

The inclusion of 5 wt.% Ni⁰ dopant onto the Mg NCs dramatically decreased the activation energy for absorption for the Mg NCs. The value is comparable to reported E_a 's for ball milled Mg and MgH₂ with small amounts of transition metals, transition metal oxides, and transition metal halides¹⁸. The effect on E_a is less pronounced for the 1 wt.% sample, however, as the absorption of H₂ is only slightly better than the pure Mg NCs. The doping level for 1 wt.% is very low compared to doping amounts used in ball-milling samples. Since one of the drawbacks to using a large amount of catalyst particles for H₂ absorption is the corresponding decrease in wt.% of H₂ gas absorbed, finding a lower limit to amount of catalyst used while still maintaining acceptable kinetics is advantageous. The catalyst is well dispersed through the synthetic method, but the low atomic percentage may not provide enough catalytically active sites to have a strong effect on the hydrogenation kinetics.

The desorption E_a s of the Mg NCs are less effected by the presence of the Ni on the surface of the Mg NCs. The values obtained are lower than bulk Mg-powder (140-160 kJ/mol), but the change in activation energy between 5 wt.% Ni-doped and undoped samples are similar to those obtained by ball- milling. More recently, literature has

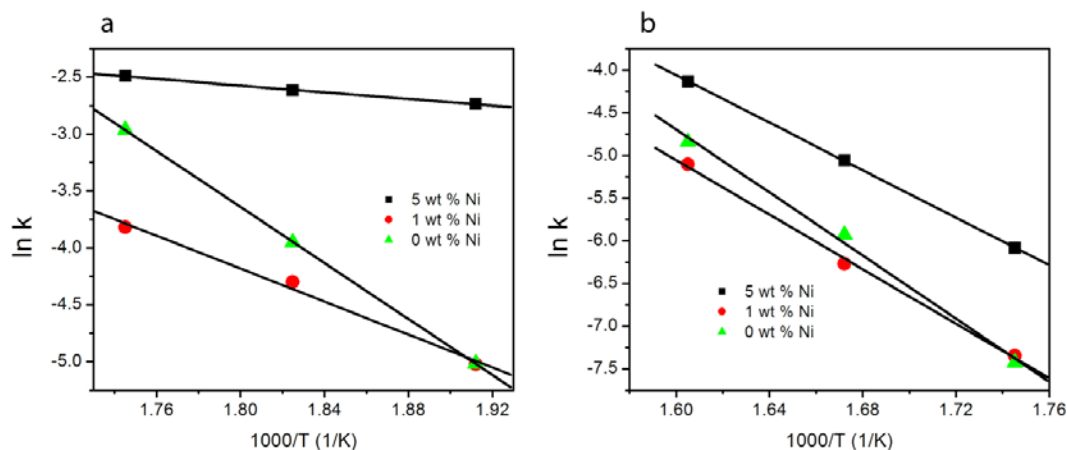


Figure 6.6. Arrhenius plots for the hydrogenation (a) and dehydrogenation (b) of MgNCs with 5 wt% (square), 1 wt% (circle) and 0 wt% (triangle) Ni_(m)

Table 6.2. Calculated activation energies for absorption and desorption.

Sample	E _a (KJ/mol) – Cycle 1 H/D	E _a (KJ/mol) – Cycle 2 H/D	E _a (KJ/mol) – Cycle 3 H/D
MgNC - 5 wt % Ni	26.3 / 115.7	15.6 / 105.6	12.8 / 123.7
MgNC - 1 wt % Ni	65.7 / 132.4	60.1 / 133.2	80.0 / 134.1
MgNC - 0 wt % Ni	81.9 / 153.4	85.6 / 152.6	78.1 / 153.5

indicated that the JMA model used to for fitting the desorption data does not take into account surface activation processes and overestimates the E_a of desorption^{49-50,52}. Therefore, the Kissinger method, which relates the temperature of endothermic heat flow to sample heating rate, is a better model to study the effect of Ni_(m)-doping on the desorption of MgH₂ NCs. DSC measurements, performed by Sarah Frederick (Prieto Group - CSU), are underway.

The effect of Ni-doping has also been found to aid in the H/D cycling capabilities of the Mg NCs and that effect is reiterated here with the cycle-number experiments. Figure

6.7 displays the different isotherms observed for the 5 wt% Ni_(m)-doped samples (a,b), the 1 wt% Ni_(m)-doped samples (c,d) and the undoped Mg NCs (e,f). There is an obvious decrease in reaction rate for the undoped samples found at all temperatures (Figure 6.7c, inset). The uniform decrease in the rate constants at all temperatures is hidden by the data in Table 6.2; that is, a constant activation energy value through multiple cycles does not necessarily imply a constant rate. However, the Arrhenius plot for the 5 wt.% and 1 wt.% Ni-doped samples (Figure 6.7a and c, inset) shows very little change in k with cycle number. Though 3 cycles is not enough to report a truly comprehensive study on the cycling capabilities of Mg NCs, retention of reaction rates are necessary for practical applications. The continued catalytic activity of the Ni_(m) is important to realizing Mg NCs as a viable H₂-storage material.

6.4 The formation of Ni⁰ on the surface of Mg NCs

The reported literature concerning electrochemical reduction of nickelocene is complex. Gubin and coworkers⁶¹⁻⁶² proposed that the reduction of the complex is a 2 electron, irreversible reduction. Geiger *et al.*⁶³, using low temperature electrochemical measurements, suggested that the reduction of NiCp₂ follows a slow 1-electron electrochemical reduction followed by a (or several) chemical reaction(s) that produce a more easily reduced product (ECE mechanism). An observed large peak separation also suggested to Geiger that the heterogeneous reduction of NiCp₂ involves structural or solvation changes, but is also only stable at low temperatures (-56 °C). Therefore, we suggest three processes that may take place for the *in situ* reduction of NiCp₂ in the presence of the reducing solution.

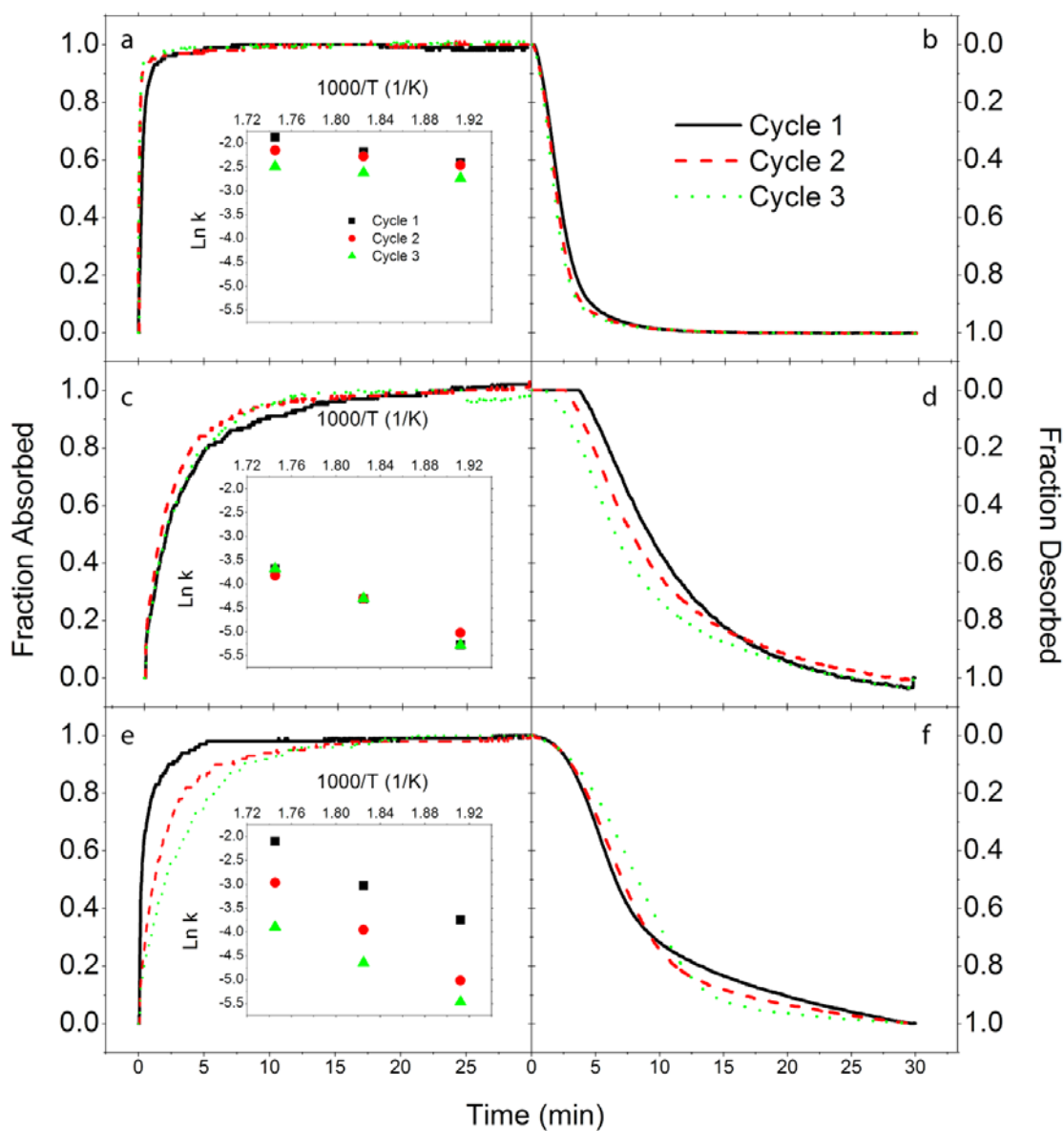


Figure 6.7. Hydrogenation (523 K) and dehydrogenation (598 K) of 5 (a,b), 1 (c,d) and 0 (e,f) wt% Ni_(m) doped MgNCs. Each sample was cycled 3 times and the Arrhenius plots for absorption for cycle 1 (square), cycle 2 (circle) and cycle 3 (triangle) are displayed as insets.

Table 6.3. Reduction Potentials (vs H/H⁺) for MgNC synthesis

Li ⁺ + e ⁻	→	Li _(m)	-3.04 V
K ⁺ + e ⁻	→	K _(m)	-2.93 V
Na ⁺ + e ⁻	→	Na _(m)	-2.71 V
Biphenyl + e ⁻	→	Biphenyl ⁻	-2.67 V
Napthalene + e ⁻	→	Napthalene ⁻	-2.60 V
Phenanthrene + e ⁻	→	Phenanthrene ⁻	-2.55 V
Mg ²⁺ + 2e ⁻	→	Mg _(m)	-2.38 V
NiCp ₂ + 2e ⁻	→	[NiCp ₂] ²⁻	-1.50 V ⁶²
		or	
NiCp ₂ + e ⁻	→	[NiCp ₂] ⁻	-1.48 V ⁶³

First, the reducing solution is strong enough to immediately produce Ni_(m) clusters, which are then deposited onto the surface of the MgNC. The high-surface energy of the Mg nanoparticles drives the Ni_(m) to agglomerate together, or to the surface of the MgNCs. This pathway suggests that there will be the presence of clustered nickel nanoparticles or the presence of crystalline nickel on the surface of the nanoparticles. Neither is observed in either XRD or TEM analysis, even on samples made with a 20 wt % Ni_(m).

Second, the reduction of the NiCp₂ is slow, as observed by the previous studies. By following the results obtained by Gubin, a more likely reaction pathway is the slow formation of the [NiCp₂]²⁻ by the reducing solution, followed by a coulombic attraction of the metallocene anion to the slightly positive “mirror-charge” of the Mg NCs. The surface of the Mg_(m) can now catalyze an intramolecular reduction of the highly-unstable [NiCp₂]²⁻ (at elevated temperatures) of the Ni²⁺ metal core to Ni_(m), forming small islands of Ni_(m) on the surfaces and edges of the Mg NCs.

Finally, and closely related to the second pathway, the reduction of the NiCp₂ can happen by only one electron. Geiger observed the presence of this anion electrochemically, albeit at -56 °C, and it would also be coulombically attracted to the surface of the Mg NCs. The highly unstable d⁹ complex would likely undergo a structural reformation (supported by slow electron dynamics observed electrochemically) by forming a more stabilized staggered geometry. The change in symmetry⁶⁴ of the [NiCp₂]⁻ has multiple consequences beyond stabilization of the e_g^{*} antibonding orbitals (now split into a₁^{*} and b₂^{*} orbitals). The bonding π-orbitals are destabilized, decreasing the bonding character between the Ni²⁺ metal core and the Cp rings. This facilitates a σ-σ bonding interaction between the Mg 2s bands and the [NiCp]⁻, further weakening the bonding between the metal core and the Cp-rings. At this point, a co-reduction of the complex, one electron from the dangling Mg_(m) bonds and one from the reduced antibonding b₂^{*} orbital, can inject into the Ni 4s orbital. This stabilizes the surface of the Mg NCs, plates Ni⁰ onto the surface and releases 2 Cp⁻ anions into solution. Hypothetically, reaction (3) happens in three steps (disregarding the first suggested reaction pathway): the formation of the [NiCp₂]^{A-} (A = 1 or 2) anion, the attraction of the anion to the surfaces or edges of the Mg_(m), and finally the intramolecular or co-reduction of the anion to form Ni_(m), evenly distributed on the surface of the Mg NC.

Repulsive negative charges between [NiCp₂]^{A-} molecules on the surface of the Mg NCs, along with a slow drop-wise addition and vigorous stirring, could contribute to the theorized distribution of the Ni_(m)-dopant evenly across the surface of the Mg NC. Then the reduction of the complex's Ni-core, possibly aided in any structural changes in [NiCp₂]^{A-} caused by the coulombic attraction to the metallic surface of the Mg NC, can

proceed. $\text{Ni}_{(m)}$ forms without the presence of much long range order, implied by the presence of Ni^0 in XPS spectra but not in XRD patterns (even at a high concentrations of NiCp_2). Gubin's two-electron irreversible reduction is predicated on the presence of a d^{10} $[\text{NiCp}_2]^{2-}$ anion, which has never been observed electrochemically or spectroscopically. The complex $[\text{NiCp}_2]^-$ is also very electron rich, but the existence of the anion has been shown electrochemically⁶³.

Though much work needs to be done to affirm or disprove our theories, one easy experiment was performed, where NiCp_2 was added to the reducing solution without the presence of Mg NCs. In this case, no $\text{Ni}_{(m)}$ was formed and the reducing solution remained dark-green. Therefore, the presence of the highly-active Mg NCs must aid the intramolecular reduction, likely through a surface-induced structural rearrangement of the molecule or the mixing of the σ -orbitals in the staggered complex. Further investigations into the exact mechanism of the doping reaction are underway.

6.4 Conclusions

The synthesis of Mg NCs out of solution has opened new pathways to control the size, apply the dopant and understand the H_2 -sorption properties of a promising storage system. The importance of $\text{Mg}_{(m)}$ in Grignard chemistry provided a start to a novel synthetic method. The capability of Ni^0 to coat the surface of the Mg was more complex. MgCp_2 's solubility in glyme and structural similarity to NiCp_2 was fortunate, but there are very different bonding and reduction properties of the two metallocenes. Solution methods to form and dope nanocrystals is a scalable process. Large amounts of Mg NCs can be synthesized, since the largest samples (1.5 g) were only limited by available glass-

ware. Additionally, the synthesis does not require expensive ball-milling equipment. The uniformity of the Mg NCs affords the direct comparison between the physical and sorption properties of the light metal hydride.

The physical analysis of the Mg NCs illustrated the synthesis of low-polydisperse, hexagonal-magnesium nanoparticles in a large range of crystal sizes. Through careful *in situ* doping techniques, Ni⁰ was uniformly dispersed throughout the Mg NCs. Crystalline Ni was never detected in XRD patterns, however, the presence of elemental nickel was confirmed by EDX and XPS. Curve-fitting analysis of the Ni 3d region revealed the oxidation of the Ni on the surface to be neutral or anionic, but further EXAFS analysis is needed to determine the exact nature and role of the catalyst.

The H/D analysis of the Mg NCs displayed some outstanding kinetics for hydrogen storage. The presence of a Ni_(m) catalyst at 5 wt % on the MgNCs reduced the E_a(abs) by an order of magnitude. Desorption kinetics based on DSC measurements (Sarah Frederick - CSU) will be compared to the rate constants obtained from the JMA model. The effect of 1 wt% Ni on the absorption properties were less pronounced, but the Mg NCs maintained a constant rate through three cycles (Figure 6.7c).

Our unique synthetic method may be applied for other/additional dopants on the surface of Mg NCs. The uniform dispersion of mixed-dopant systems can maximize both the absorption and desorption of H₂. Multiple synthetic methods are important to finding unique solutions to our energy needs. The hydrogen economy is dependent on finding new materials, or new synthetic methods to make better materials, for efficient and reversible H₂ storage.

6.5 References

- (1) Schlappbach, L.; Zuttel, A. *Nature* **2001**, *414*, 353.
- (2) Schuth, F.; Bogdanovic, B.; Felderhoff, M. *Chemical Communications* **2004**, 2249.
- (3) Zaluska, A.; Zaluski, L.; Strom-Olsen, J. O. *Applied Physics a-Materials Science & Processing* **2001**, *72*, 157.
- (4) Huot, J.; Liang, G.; Schulz, R. *Applied Physics a-Materials Science & Processing* **2001**, *72*, 187.
- (5) Lu, J.; Choi, Y. J.; Fang, Z. Z.; Sohn, H. Y.; Ronnebro, E. *Journal of the American Chemical Society* **2010**, *132*, 6616.
- (6) Paskevicius, M.; Sheppard, D. A.; Buckley, C. E. *Journal of the American Chemical Society* **2010**, *132*, 5077.
- (7) Sakintuna, B.; Lamari-Darkrim, F.; Hirscher, M. *International Journal of Hydrogen Energy* **2007**, *32*, 1121.
- (8) Zaluski, L.; Zaluska, A.; Strom-Olsen, J. O. *Journal of Alloys and Compounds* **1999**, *290*, 71.
- (9) Li, W. Y.; Li, C. S.; Ma, H.; Chen, J. *Journal of the American Chemical Society* **2007**, *129*, 6710.
- (10) Berube, V.; Radtke, G.; Dresselhaus, M.; Chen, G. *International Journal of Energy Research* **2007**, *31*, 637.
- (11) Aguey-Zinsou, K. F.; Ares-Fernandez, J. R. *Chemistry of Materials* **2008**, *20*, 376.
- (12) Bogdanovic, B. *International Journal of Hydrogen Energy* **1984**, *9*, 937.
- (13) Kalidindi, S. B.; Jagirdar, B. R. *Inorganic Chemistry* **2009**, *48*, 10856.
- (14) Norberg, N.; Arthur, T. S.; Prieto, A. L. *Journal of the American Chemical Society*, In preparation.
- (15) Fernandez, J. F.; Sanchez, C. R. *Journal of Alloys and Compounds* **2002**, *340*, 189.
- (16) Charbonnier, J.; de Rango, P.; Fruchart, D.; Miraglia, S.; Pontonnier, L.; Rivoirard, S.; Skryabina, N.; Vulliet, P. *Journal of Alloys and Compounds* **2004**, *383*, 205.
- (17) Checchetto, R.; Bazzanella, N.; Miotello, A.; Mengucci, P. *Journal of Alloys and Compounds* **2007**, *446*, 58.
- (18) Grochala, W.; Edwards, P. P. *Chem Rev* **2004**, *104*, 1283.
- (19) Du, A. J.; Smith, S. C.; Yao, X. D.; Lu, G. Q. *Journal of the American Chemical Society* **2007**, *129*, 10201.
- (20) Aguey-Zinsou, K. F.; Ares-Fernandez, J. R. *Energ Environ Sci* **2010**, *3*, 526.
- (21) Ares, J. R.; Aguey-Zinsou, K. F.; Klassen, T.; Bormann, R. *Journal of Alloys and Compounds* **2007**, *434*, 729.
- (22) Barkhordarian, G.; Klassen, T.; Bormann, R. *Journal of Alloys and Compounds* **2006**, *407*, 249.
- (23) Hanada, N.; Hirotooshi, E.; Chikawa, T.; Akiba, E.; Fujii, H. *Journal of Alloys and Compounds* **2008**, *450*, 395.
- (24) Oelerich, W.; Klassen, T.; Bormann, R. *Journal of Alloys and Compounds* **2001**, *322*, L5.
- (25) Liang, G.; Huot, J.; Boily, S.; Van Neste, A.; Schulz, R. *Journal of Alloys and Compounds* **1999**, *292*, 247.
- (26) Liang, G.; Huot, J.; Boily, S.; Van Neste, A.; Schulz, R. *Journal of Alloys and Compounds* **1999**, *291*, 295.
- (27) Bouaricha, S.; Dodelet, J. P.; Guay, D.; Huot, J.; Boily, S.; Schulz, R. *Journal of Alloys and Compounds* **2000**, *297*, 282.
- (28) Liang, G.; Huot, J.; Boily, S.; Schulz, R. *Journal of Alloys and Compounds* **2000**, *305*, 239.
- (29) Oelerich, W.; Klassen, T.; Bormann, R. *Journal of Alloys and Compounds* **2001**, *315*, 237.
- (30) Oelerich, W.; Klassen, T.; Bormann, R. *Materials Transactions* **2001**, *42*, 1588.
- (31) Huot, J.; Pelletier, J. F.; Lurio, L. B.; Sutton, M.; Schulz, R. *Journal of Alloys and Compounds* **2003**, *348*, 319.

- (32) Leon, A.; Knystautas, E. J.; Huot, J.; Lo Russo, S.; Koch, C. H.; Schulz, R. *Journal of Alloys and Compounds* **2003**, 356, 530.
- (33) Schimmel, H. G.; Huot, J.; Chapon, L. C.; Tichelaar, F. D.; Mulder, F. M. *Journal of the American Chemical Society* **2005**, 127, 14348.
- (34) Bazzanella, N.; Checchetto, R.; Miotello, A.; Sada, C.; Mazzoldi, P.; Mengucci, P. *Appl Phys Lett* **2006**, 89.
- (35) Yao, X. D.; Wu, C. Z.; Du, A. J.; Lu, G. Q.; Cheng, H. M.; Smith, S. C.; Zou, J.; He, Y. H. *J Phys Chem B* **2006**, 110, 11697.
- (36) Zhu, M.; Wang, H.; Ouyang, L. Z.; Zeng, M. Q. *International Journal of Hydrogen Energy* **2006**, 31, 251.
- (37) Ma, L. P.; Wang, P.; Cheng, H. M. *Journal of Alloys and Compounds* **2007**, 432, L1.
- (38) Bazzanella, N.; Checchetto, R.; Miotello, A. *Appl Phys Lett* **2008**, 92.
- (39) Dehouche, Z.; Peretti, H. A.; Hamoudi, S.; Yoo, Y.; Belkacemi, K. *Journal of Alloys and Compounds* **2008**, 455, 432.
- (40) Luo, Y.; Wang, P.; Ma, L. P.; Cheng, H. M. *Journal of Alloys and Compounds* **2008**, 453, 138.
- (41) Aguey-Zinsou, K. F.; Fernandez, J. R. A.; Klassen, T.; Bormann, R. *International Journal of Hydrogen Energy* **2007**, 32, 2400.
- (42) Aguey-Zinsou, K. F.; Nicolaisen, T.; Fernandez, J. R. A.; Klassen, T.; Bormann, R. *Journal of Alloys and Compounds* **2007**, 434, 738.
- (43) Revesz, A.; Fatay, D.; Spassov, T. *Journal of Alloys and Compounds* **2007**, 434, 725.
- (44) Bhat, V. V.; Rougier, A.; Aymard, L.; Nazri, G. A.; Tarascon, J. M. *Journal of Alloys and Compounds* **2008**, 460, 507.
- (45) Gupta, R.; Agresti, F.; Lo Russo, S.; Maddalena, A.; Palade, P.; Principi, G. *Journal of Alloys and Compounds* **2008**, 450, 310.
- (46) Mandzhukova, T.; Khrussanova, M.; Grigorova, E.; Stefanov, P.; Khristov, M.; Peshev, P. *Journal of Alloys and Compounds* **2008**, 457, 472.
- (47) Song, M. Y. *Journal of Materials Science* **1995**, 30, 1343.
- (48) Bogdanovic, B.; Hofmann, H.; Neuy, A.; Reiser, A.; Schlichte, K.; Spliethoff, B.; Wessel, S. *Journal of Alloys and Compounds* **1999**, 292, 57.
- (49) Hanada, N.; Ichikawa, I.; Fujii, H. *Journal of Alloys and Compounds* **2005**, 404, 716.
- (50) Hanada, N.; Ichikawa, T.; Fujii, H. *J Phys Chem B* **2005**, 109, 7188.
- (51) Varin, R. A.; Czujko, T.; Wasmund, E. B.; Wronski, Z. S. *Journal of Alloys and Compounds* **2007**, 446, 63.
- (52) Xie, L.; Liu, Y.; Zhang, X. Z.; Qu, J. L.; Wang, Y. T.; Li, X. G. *Journal of Alloys and Compounds* **2009**, 482, 388.
- (53) Singh, S.; Eijt, S. W. H.; Zandbergen, M. W.; Legerstee, W. J.; Svetchnikov, V. L. *Journal of Alloys and Compounds* **2007**, 441, 344.
- (54) Rieke, R. D.; Li, P. T. J.; Burns, T. P.; Uhm, S. T. *J Org Chem* **1981**, 46, 4323.
- (55) Friedrichs, O.; Sanchez-Lopez, J. C.; Lopez-Cartes, C.; Dornheim, M.; Klassen, T.; Bormann, R.; Fernandez, A. *Appl Surf Sci* **2006**, 252, 2334.
- (56) Ardizzone, S.; Bianchi, C. L.; Fadoni, M.; Vercelli, B. *Appl Surf Sci* **1997**, 119, 253.
- (57) Lee, S. M.; Ito, T.; Murakami, H. *J Mater Res* **2002**, 17, 1914.
- (58) Tolman, C. A.; Riggs, W. M.; Linn, W. J.; King, C. M.; Wendt, R. C. *Inorganic Chemistry* **1973**, 12, 2770.
- (59) Grim, S. O.; Matienzo, L. J.; Swartz, W. E. *Journal of the American Chemical Society* **1972**, 94, 5116.
- (60) Kim, K. S.; Winograd, N. *Surf Sci* **1974**, 43, 625.
- (61) Gubin, S. P.; Smirnova, S. A.; Denisovi, Li. *J Organomet Chem* **1971**, 30, 257.
- (62) Gubin, S. P.; Smirnova, S. A.; Denisovi, Li.; Lubovich, A. A. *J Organomet Chem* **1971**, 30, 243.
- (63) Holloway, J. D. L.; Geiger, W. E. *Journal of the American Chemical Society* **1979**, 101, 2038.
- (64) Lauher, J. W.; Hoffmann, R. *Journal of the American Chemical Society* **1976**, 98, 1729.